Self-ordering Dynamics in Controlled Encapsulation of Single and Multiple Cells

by

Todd Peter Lagus

Dissertation

Submitted to the Faculty of the

Graduate School of Vanderbilt University

in partial fulfillment of the requirements

for the degree of

DOCTOR OF PHILOSOPHY

in

Mechanical Engineering

May, 2014

Nashville, Tennessee

Approved:

Jon F. Edd, PhD

D. Greg Walker, PhD

Deyu Li, PhD

Haoxiang Luo, PhD

Carl H. Johnson PhD

To my children, Erik Allen and Mary Evelyn

and

To my beautiful, inspiring, and supporting wife, Kathryn Elizabeth

Acknowledgements

This work would not have been possible without the support of Vanderbilt University and its startup funds. I give special thanks to the support staff in the Department of Mechanical Engineering: Suzanne Weiss, Myrtle Daniels, and Jean Miller.

Importantly, I thank my dissertation committee for their time and thoughtful input to my PhD work. Dr. Greg Walker offered me a temporary office home and fun discussions on thermal transport. Dr. Deyu Li contributed advice, use of critical lab equipment, and rewarding collaboration with his students. Dr. Haoxiang Luo provided his assistance and advice in building two-phase flow models. Dr. Carl Johnson contributed his deep knowledge for my algae application work. Finally, I extend my deepest gratitude to my adviser and committee chair, Dr. Jon Edd. His style allowed me to independently explore while at the same time providing invaluable guidance for research and my career.

I also thank my fellow graduate students for their opinions, putting up with my factoids about Minnesota and, more importantly, their friendships. Thank you Kristina Kitko, Bryson Brewer, Sadie Gollub, Neal Dillon, Carl Hall, Kirsten Heikkinen, Lijie Yang, Qian Zhang, Charreau Bell, Hunter Gilbert, Dave Comber, Phil Swaney, Dustin House, Casey Brock, Haoran Yu, Joy Garnett, and many others for a great experience.

Most importantly, I thank my parents, in-laws, and extended family in supporting my decision to return to school. It's not easy raising now two children through a graduate program, but our family allowed us to weather it gracefully. And, of course, this accomplishment would mean nothing without the support of my wife Kathryn Elizabeth.

Table of Contents

List of Tables

List Of Figures

Citations to Previously Published Work

As previously noted, several sections of text, data, and figures have been published (or are in preparation to be published) in peer-reviewed articles and conference proceedings. Permission has been obtained from the specific journal to use this information within this document. Specific citations are provided here.

Chapter 2

> Lagus T P and Edd J F 2013 A review of the theory, methods and recent applications of high-throughput single-cell droplet microfluidics *Journal of Physics D: Applied Physics* 46 114005

Chapter 4

> Lagus T P and Edd J F 2012 High Throughput Single-cell and Multiple-cell Micro-encapsulation *Journal of visualized experiments : JoVE* **64**

Chapter 5

> Lagus T P and Edd J F 2013 High-throughput co-encapsulation of self-ordered cell trains: cell pair interactions in microdroplets *RSC Advances* **3** 20512 Reproduced by permission of the Royal Society of Chemistry, DOI: 10.1039/C3RA43624A.

Chapter 6

> Lagus T P and Edd J F 2012 Inertial focusing and ordering in low aspect ratio microchannels using reference frame tracking and rotation measurements. *ASME 2012 10th Int. Conf. on Nanochannels, Microchannels, and Minichannels, ICNMM 2012* (Rio Grande, Puerto Rico) pp 633-8

Chapter 7

> Lagus T P and Edd J F 2014 Fundamentals of Inertial Microfluidics for Droplet Encapsulation and Cytometry Design Applications (In preparation)

Chapter 1

Introduction

The intense activity and progress in microfluidics over the last several years is a result of combined efforts of researchers with expertise in diverse fields of fluid mechanics, thermodynamics, applied physics, chemistry, materials science, manufacturing, biochemistry, biotechnology, and medicine. Essentially, microfluidic systems manipulate small volumes of fluid within micro-scale channels. Microfluidic channels may be integrated into macro-scale systems or may be standalone, miniaturized devices, often referred to as lab-on-a-chip systems[1-3]. Self-contained microfluidic devices include channel networks, fluid reservoirs, and integrated sensors and actuators which are interfaced to users or automated programs. In simple forms, microfluidics involves single-phase flow of liquids, but complex two-phase flows of multiple liquids, gases, and suspended solids are encountered in many applications. Though the primary materials are silicone elastomers[4], glass, and silicon, the microfluidic materials list also includes various polymers, hydrogels, semiconductors, and metals as needed to achieve specific properties. Mass transport, thermal transport, chemical reactions, and biological interactions must all be considered as microfluidics widens to a large number of fields and applications.

Before diving into the technical aspects of microfluidics, it is worth noting that the field has not been widely commercialized. A recent series of focus papers[5-7] cites the lack of mass-market consumer end-uses and business-to-business product delivery as key reasons for failure of many microfluidics companies. Since proven technologies exist for these many fields, taking

on new financial risks for both manufacturers and end users must be justified with a very significant improvement in throughput and cost[7]. One proposed roadmap[3] presented four biological market segments on which microfluidics could capitalize: *in vitro* testing (point of care, diagnostic medicine, etc.), drug discovery, biotech industries (bio-based processes for industry), and ecology (agriculture, water testing, homeland security). In this work, we present an applied microfluidic device, supported by fundamental two-phase flow mechanics, that has applications in all four of these industries.

1.1 Introduction to Droplet Microfluidics

As a subset of microfluidics, droplet microfluidics involves devices that produce microscale diameter (typically on the order of tens to hundreds of μm) droplets of one fluid within a second immiscible carrier fluid. Droplet-producing micronozzles are capable of formation rates from slow dripping to over 10 kHz. Monodisperse water-in-oil (w/o) droplet emulsions provide nearly identically-sized (typically 1-5% deviation from the mean) femto-, pico-, or nanoliter aqueous compartments, each a microreactor with a specified chemical composition and encapsulated cargo such as particles, cells, or biomolecules (proteins, DNA, and metabolites). Within each droplet, a separate experiment takes place that can reveal sample heterogeneity that is otherwise obscured in bulk samples to characterize the effects of rare cells[8,9]. Alternatively, identical samples can be exposed to distinct stimuli by varying droplet conditions for applications such as drug discovery[10,11]. Moreover, volumetric confinement avoids dilution of products for improving detectable signals and reducing reagent volumes. This confinement also provides value in growth assays where cells are fooled into thinking they are in higher density cell environments[12].

1.2 Introduction to Inertial Microfluidics

Less ubiquitous than droplet microfluidics, the term "inertial microfluidics" defies the notion that small dimensions equate to diffusion-dominated Stokes' flow regimes ($Re_c << 1$). Using the properties of water ($\rho = 1{,}000$ kg/m^3, $\mu = 1.12 \times 10^{-3}$ Pa-s), a channel hydraulic diameter D_h = 50 μm and a maximum flow velocity U_{max} = 1 cm/s computes to a channel Reynolds number Re_c [$= \rho U_{max} D_h / \mu$)]= 0.5. As the Re_c is not "much less" than 1 as implied in Stokes' flow, neglecting the inertial terms in the Navier-Stokes Equations is no longer adequate.

In cylindrical flows, lift forces push particles of finite size to a thin, "focused" annulus at a radial position known as the Segre-Silberberg radius[13] (Figure 1a), named after its original discoverers. More recently, focusing has been observed in rectangular microchannel flows. Here, particles and cells migrate to discrete lateral positions in lieu of the radial distribution noted in cylindrical tubes. In addition to dependence on flow inertia, focusing dynamics and equilibrium are dependent on particle size. The particle Reynolds number Re_p [$= Re_c(a/D_h)^2$] combines the inertial requirements with the particle size a and hydraulic diameter D_h. This size dependence leads to applications in high-throughput particle and cell separations based on size[14-18].

For higher-concentration suspensions, hydrodynamic interactions between focused particles leads to the formation of particle trains in flow. In addition to containing focused cross-stream positions, these passively-formed trains are highlighted by equal longitudinal spacing between each particle. This additional degree of spatial control provides additional applications in the biomedical field for flow cytometry[19] and other high-throughput screening methods where cell sensors and actuators (see Chapter 2) often act on the order of milliseconds or less. This ordering phenomenon also constitutes an essential portion of the applications highlighted in the current research.

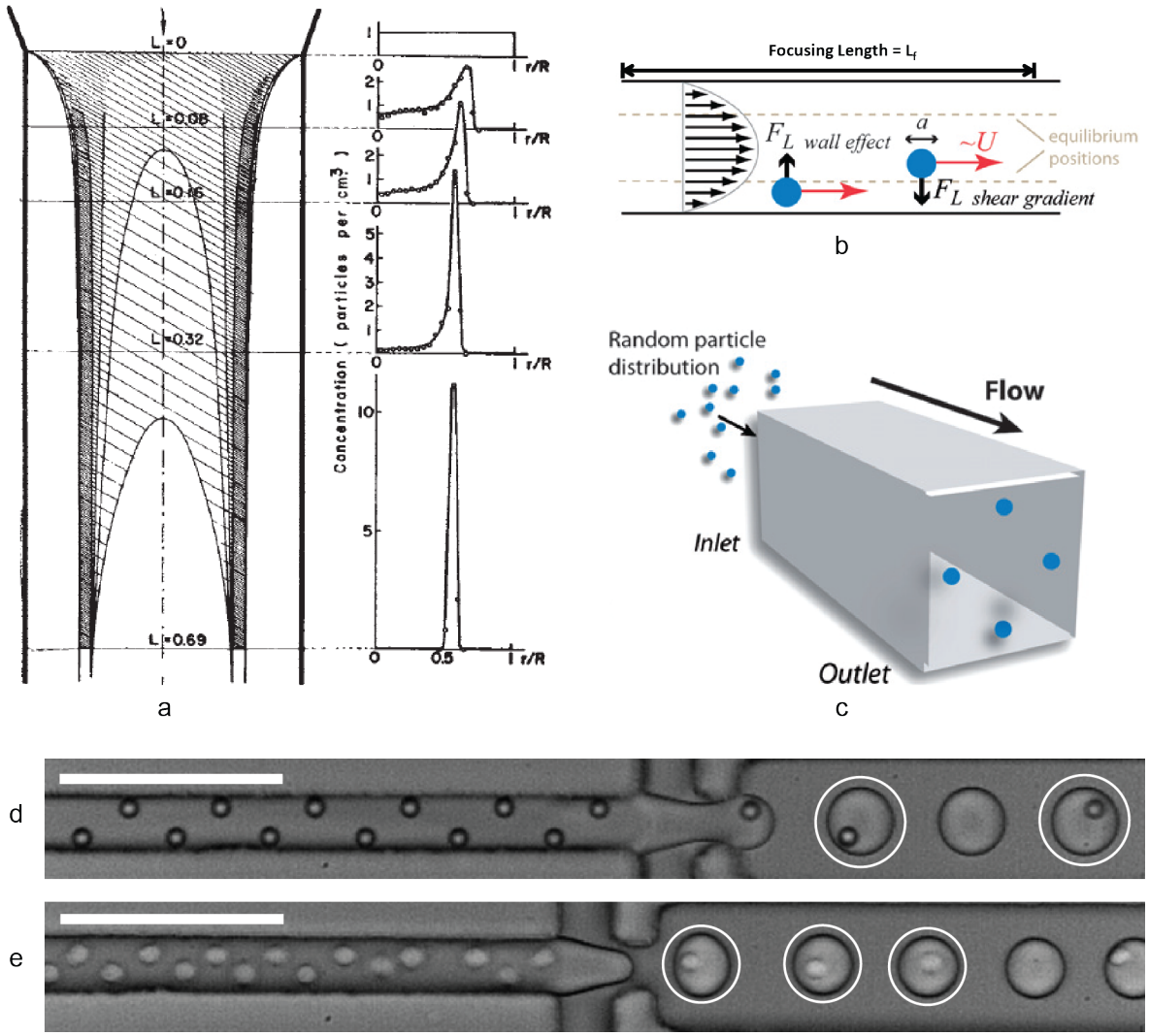

Figure 1.1. Inertial and droplet microfluidics. (a) Work from Segre and Silberberg[13] showing a randomly dispersed particle inlet in a cylindrical channel. The plots on the right show the particle distribution to the Segre-Silberberg radius r/R ~ 0.6. (b and c) Schematics from [20] illustrating the force balance leading to two equilibrium positions in each lateral direction (b) and a 3-D schematic (c) showing four quadrilaterally symmetric equilibrium positions in rectangular channel flow. (d and e) Ordering of two staggered trains of particles (d) and cells (e), which are exploited to control encapsulation of single cells in droplets. Scale bars in (d) and (e) represent 100 μm.

1.3 Combining Droplet Microfluidics and Inertial Microfluidics

As previously noted, confinement of biological materials in droplets provides isolated bioreactors, limits biomarker dilution, and controls cell environments. However, applications using cells encapsulated in droplets have suffered from the inability to control the number of cells in each droplet[21]. Cell encapsulation is often achieved by delivering a randomly dispersed

cell suspension through a droplet generation nozzle, trapping cells in the resulting droplets. For single cell encapsulation using this Poisson (random) encapsulation, a maximum of 36.8% of droplets would contain one and only one cell. The remaining droplets, either empty or containing too many cells, would need to be removed from the sample, reducing throughput and wasting valuable cells and reagents. For droplets sorted using fluorescence activated cell sorters (FACS), cell suspensions are diluted to avoid droplets containing more than one cell; here, typical single-cell encapsulation efficiencies are on the order of 20%[22,23].

The combination of droplet and inertial microfluidics in a single device allows for efficient encapsulation of cells in droplets. Upstream of a droplet generation nozzle, ordered trains of cells form. Because of the equal longitudinal spacing between cells, they arrive at the droplet generation interface at equal time intervals (given a constant flow rate). By tuning the aqueous cell suspension and immiscible oil flow rates, droplets are generated at the same frequency that cells arrive at the nozzle, thereby controlling the number of cells in each droplet. This technique was first applied[24] to encapsulate particles where nearly 80% of droplets contained one and only one particle. This represented over a twofold improvement on the maximum Poisson probability and a nearly fourfold improvement to a typical FACS encapsulation probability. Additionally, the study encapsulated single human promyelocytic leukemia (HL60) cells at nearly 15 kHz with over 90% cell viability[24].

Single-cell encapsulation is useful in determining individual cell responses and highlighting rare cells. However, limiting encapsulation to just single cells misses the opportunity to capture more complex interactions between cells. Using random encapsulation, the maximum probability of obtaining droplets containing a pair of two distinct cell types drops to 13.5% (the product of two independent Poisson probabilities) and to 5% for typical FACS

dilutions. Based on these low success rates, the market for improving throughput and conserving valuable reagents and cells is even greater than the single-cell case.

Here, we present device designs and protocols for encapsulating two cells in droplets generated at kHz rates. First, we demonstrate a protocol for encapsulating two cells of the same type (using particles as cell surrogates). More importantly, we also present a new device for encapsulating two cells of distinct types. We encapsulated separate mating type *Chlamydomonas reinhardtii* microalgae cells and observed subsequent sexual mating and long-term survival within picoliter-sized droplets with no light or cell culture media exchange. Using both experimental and computational fluid mechanics, we also provide additional insight into the dynamic ordering phenomena, including interparticle train spacing and force scaling.

1.4 Contents of this Dissertation

Two-phase fluid mechanics, emulsion thermodynamics, materials science, and biology combine to produce an elegant, passive system for encapsulating cells in droplets at rates as high as tens of kHz. This document provides a summary of work toward two distinct but related paths. The first delves into applied microfluidics, combining droplet microfluidics with inertial microfluidics to efficiently control the number of cells encapsulated in a droplet. Previous work efficiently encapsulating single cells in droplets, where a majority of droplets contain one and only one cell, is extended to encapsulate multiple cells here. The designs and applications presented here encapsulate cell pairs of a single type and, more notably, streams of two separate cell types such that a droplet contains one and only one cell of each type. The application has high implications for studies utilizing the benefits of cell co-culture interactions by combining them with the benefits of droplet microfluidic throughput and confinement in droplets.

Several chapters (Chapters 2, 4, 5, 6, and 7) represent complete works that have been published or are in the preparation process to peer-reviewed journals and conference proceedings. Chapter 2 includes a published review of the extensive background on the techniques, constraints, and motivations for studying high-throughput droplet microfluidics with particular focus droplet generation, actuation, and sensing methods of cell-containing droplets. Chapter 3 explains in greater detail the theory, key parameters, and design constraints of the relatively new inertial microfluidics field. Chapter 4 introduces the combination of droplet and inertial microfluidics to improve cell encapsulation efficiency, i.e. droplets containing only the desired number of cells. The work extends single-cell encapsulation to multiple-cell (here represented by polystyrene microspheres as surrogates) encapsulation by adjusting droplet generation frequencies such that two and only two particles are encapsulated in a single droplet. Here, the percentage of droplets containing two and only two particles was 71.5%, a nearly threefold improvement over random encapsulation. The chapter also discusses a number of conflicting design constraints including the need for sufficient inertia for cell focusing and ordering is countered by the upper limits on inertia so as to avoid jetting at the droplet generation interface.

The device shown in Chapter 4, however, only provided dual-particle encapsulation for particles of the same type. Chapter 5 presents a new device with two parallel ordering channels for efficiently encapsulating pairs of distinct cell types. We demonstrated the device both separate particle streams at paired encapsulation efficiencies (percentage of droplets containing the "correct" number of cells) nearly five times greater (64%) than Poisson co-encapsulation (13%). Additionally, we encapsulated two opposite mating-type gametes of *Chlamydomonas reinhardtii* algae in droplets. Despite the stresses of controlled encapsulation (and an additional

thermal processing step to remove algae flagella), we captured sexual mating in confined picoliter-sized droplets using high-speed video. Remarkably, the resulting zygospores and many unmated gametes remained viable after 17 days of maturation in the dark with no cell culture media changes. The zygospores completed the mating process, and offspring resumed mitosis upon agar plating.

In the second part of this work, we investigate the fundamentals of inertial focusing and ordering that enable controlled encapsulation. For the applied studies presented in Chapters 4 and 5, we relied on trial and error to obtain cell train spacing for a given ordering channel geometry and aqueous cell suspension flow rate. However, for feasible commercial applications, one must be able to predict particle spacing and arrival frequency at the nozzle early in the design phase. To this end, we have undertaken more fundamental focusing and ordering studies of particles and cells. Chapter 6 presents work using a Lagrangian reference frame to track particles and cells a stage which moves at the same velocity as the particles in flow. This reference frame tracking allowed for observation of the cross-stream migration and particle interactions for long durations. However, the motorized microscope stage speeds in this work were limited to 10 cm/s, and thus combinations of low flow rates and large channel dimensions.

In Chapter 7, we present results using a custom high-speed reference frame tracking system using a moving cart mounted on air bearings. The stage is capable of translation on the order of meters per second and thus does not carry the limits from Chapter 6 on flow rates and channel size. Here, we present experimental particle tracking using the applied devices presented in Chapter 4 and Chapter 5. Experimental results allow for quantification of spacing, velocity, and interparticle forces as functions of flow rate and particle size, and for tracking ordering behavior that occurred in two stages for rectangular channels.

However, distilling experimental focusing and ordering data was difficult because of the infinite combinations of interactions for in any given system. Additionally, microfabricating a large number of different channels make parametric studies time prohibitive, particularly when studying the effect of geometry. Numerical models, on the other hand, are well suited for parametric studies, although modeling two-phase flows requires massive computational expense. In Chapter 7, we employed experimental data for particle spacing and rotation to serve as model inputs to facilitate convergence. A number of select interactions featuring pairs of particles were compared to those noted in experimental results and used to verify the models.

The iterative relationship between experiment and simulation enhances the interplay between application and fundamentals to predict ordering behavior in controlled encapsulation devices. Many of these parameters in Chapter 7 are also expressed in terms of key parameters, namely the channel Reynolds number Re_c and particle Reynolds number Re_p. In particular, the cell shear forces were on the order of tens of Pascals for the modeled Re_c and Re_p, and the interparticle forces scaled as Re_c^2 for constant particle size.

Chapter 2

Droplet Microfluidics for Cellular Applications

Given their ability to efficiently encapsulate molecules and cells at kHz rates, droplet microfluidic devices are well poised to have a major impact on high-throughput screening technologies for traditional applications such as FACS and for smaller and potentially more mobile systems. A number of excellent reviews highlight recent progress in droplet-based microfluidics for single-cell analysis[25-28]. Rather than replicate the scope of those reviews, we discuss droplet microfluidics with a focus on high-throughput applications. This includes a summary of two-phase fluid physics, recent advances in cell encapsulation, sensing, and actuation methods which are at least potentially adaptable for high-throughput applications. Finally, we discuss in detail a select number of recent droplet microfluidic publications which provide unique contributions in techniques and methods for high-throughput single-cell analysis.

To avoid confusion with a closely related field, it is important to distinguish between droplet microfluidics and digital microfluidics. Specifically, we limit this review of "droplet microfluidics" to pressure driven devices where droplets are enclosed within channels and immersed in a continuous phase oil carrier fluid. On the other hand, "digital microfluidics" utilizes microfabricated electrode arrays programmed to move, mix, react, analyze, and split droplets through electrowetting on a dielectric-coated substrate[29,30]. Despite many digital microfluidic methods in lab-on-a-chip systems, expansion of digital microfluidics into massively parallel, high-throughput systems is limited by the size, scalability, and dynamic response of the electrodes, so it is not widely discussed here.

Pressure-driven droplet microfluidics has been successfully implemented for molecular biology applications such as amplifying single-copy DNA molecules using the polymerase chain reaction (PCR)[31-34]. Microscale droplets can also provide encapsulation of single cells[11,23,35-37] for high-throughput screening (HTS) applications involving drug discovery, toxicity testing, various "omics" studies, and rare cell analysis. This introduction highlights recent advances in high-throughput, single-cell droplet microfluidic methods and applications which have a potential to be economically competitive in the commercial marketplace.

As a testament to the recent push to high-throughput microfluidic research toward commercial applications, a Web of Science citation report for the topic phrase "'high throughput' microfluidic(s)" indicated publication of around 250 papers in both 2010 and 2011[38]. Despite this high interest level, the definition of "high throughput" remains nebulous. As a working definition for this review, we select a commercial method to quantify our high-throughput benchmark. Specifically, commercial Fluorescence Activated Cell Sorters (FACS) utilize laser illumination and fluorescence sensing with photomultiplication followed by electrostatic deflection of cell-containing droplets suspended in air. This allows them to count and automatically sort cells to microwells at rates on the order of 10,000 cells/s[39,40]. Though FACS machines can in fact process on the order of 70,000-100,000 droplets/s[41,42], single-cell encapsulation requires the use of dilute cell suspensions, causing many empty droplets and a reduction in the effective cell throughput. State-of-the-art FACS units are also equipped with on-board "index sorting" software that tracks and indexes droplet properties by microwell, allowing for correlation of sorted cell group properties with downstream transient response tracking of cell populations in any given well[39].

2.1 Droplet Generation Dynamics

A number of focused reviews[43-47] provide detailed insight into droplet generation and flow dynamics. Here, we briefly summarize them to highlight how droplet dynamics both facilitate and limit high- throughput droplet microfluidic applications. While droplet generation may be driven using active methods such as piezoelectric actuators[48] and electric fields[49], aqueous monodisperse droplets are most commonly formed in continuous pressure-driven nozzles with flow focusing[50] (Figure 2.1a), co-flowing[51] (Figure 2.1b), or T-junction[52](Figure 2.2a) designs. These passive droplet generation methods benefit from the ability to increase throughput simply by adding parallel channels since they do not require individually-addressable actuation. By cascading droplet generation interfaces in series, more complex emulsions within emulsions are also possible[53,54](Figure 2.1c).

Hydrophobic channel surfaces are required to prevent unstable, polydisperse w/o droplet formation due to wetting effects[55]. For multiple emulsions[53,54](Figure 2.1c), nozzle surface properties must alternate between hydrophobic and hydrophilic. Polydimethylsiloxane (PDMS) is a commonly used natively hydrophobic, transparent (to both UV and visible light) elastomer used in microfluidic devices. The high elasticity and gas permeability of PDMS, while beneficial in some cases, are not amenable to all applications. Additionally, the typical laboratory-scale fabrication method, replica molding with thermal curing[4], does not lend itself to mass production due to long process times[56]. Additional materials such as polymethyl methacrylate (PMMA) and polyether ether ketone (PEEK) thermoplastics have also been studied as alternatives (discussed in depth elsewhere[56-60]) using methods such as hot embossing and injection molding, but manufacturing costs have been too high to justify replacing existing screening methods with microfluidic devices.

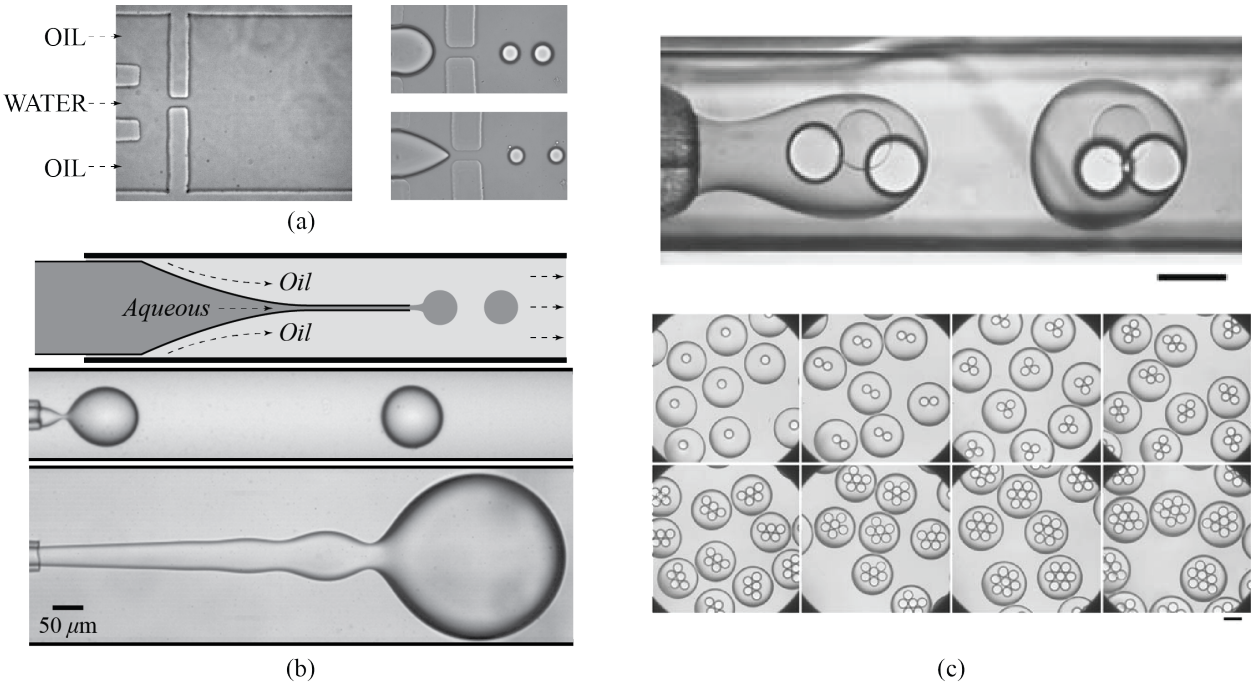

Figure 2.1. Droplet generation methods. (a)Flow-focusing geometry implemented in a microfluidic device (left) with orifice with of 43.5 μm. The droplet generation (right) demonstrates the ability to create monodisperse droplets of controlled size[50]. Copyright 2003, American Institute of Physics. (b)Co-flowing device with tapered aqueous flow inner capillary nested inside an oil flow outer capillary schematic(top), co-flowing droplet generation (middle), and a widening jet (bottom)[51]. The widening jet reflects the transition from dripping to inertial jetting due to Weber number greater than one as the aqueous flow rate increases. Copyright 2007 by the American Physical Society. (c)Precisely controlled monodisperse double emulsions using nested co-flowing capillaries. Each scale bar equals 200 μm[53]. Parts (a), (b), and (c) reprinted with permission from [50], [51], and [53], respectively.

For flow focusing and co-flowing nozzles, water-in-oil droplets break off from the aqueous fluid stream when oil shear stress overcomes interfacial tension that keeps droplets attached to the aqueous neck. For T-junction nozzles at low oil flow rates, the oil flow "pinches" droplets when the aqueous stream blocks the continuous flow channel, thereby creating a pressure buildup which leads to droplet generation(Figure 2.2a)[61]. At higher oil flow rates, oil shear acts to detach droplets in a mechanism similar to that shown in flow focusing and co-flowing nozzles[62]. Droplet size and formation rates depend on the combinations of aqueous and oil phase flow rates, nozzle geometry, respective dynamic viscosities μ and densities ρ, and interfacial tension between phases.

The balance of inertial, viscous, and interfacial tension forces governs droplet formation and confined droplet flow. The relationship between the inertial and interfacial tension forces of the aqueous phase is quantified by the Weber number We, given by

$$\mathrm{We} = \frac{\rho U^2 D_h}{\sigma}, \tag{2.1}$$

where ρ, U, and D_h represent the aqueous fluid density, mean velocity, nozzle hydraulic diameter, and σ represents the interfacial tension between the two immiscible fluids. In determining droplet formation dynamics, the Weber number is often paired with the Capillary number Ca, representing the ratio of viscous forces to interfacial tension forces and is given by

$$\mathrm{Ca} = \frac{\mu U}{\sigma}, \tag{2.2}$$

where μ and U represent the oil fluid viscosity and mean velocity, respectively, and σ again represents the interfacial tension between the two immiscible fluids[51].

While obtaining a clear-cut scaling law is challenging[45], We and Ca still illustrate the relative importance of inertial, viscous, and interfacial tension forces. Plotting the aqueous phase Weber number against the oil phase Capillary number provides a droplet formation regime map and highlights the critical Weber and Capillary numbers marking the transition from steady droplets to jetting[51]. At small aqueous and oil flow rates (We << 1 and Ca << 1), the aqueous fluid forms pulls apart an aqueous neck to minimize surface energy, yielding monodisperse droplets. At larger aqueous flow rates (We ~ 1 or greater), inertial forces begin to dominate interfacial tension forces. At a critically high Weber number, the aqueous neck moves downstream as a wide unstable "jet" of aqueous fluid from the nozzle (see Figure 2.1b). A transition from dripping to jetting also occurs as oil flow rates increase (Ca ~ 1 or greater). At a critically large Capillary number, viscous drag forces from the outer carrier oil pull on the

aqueous flow enough to overcome interfacial tension forces, causing the inner aqueous fluid to stretch into long, thin streams[51,62,63].

In T-junctions, slightly different breakup mechanisms lead to dripping/jetting transitions[62]. At low Capillary numbers (low oil flow rates), the aqueous fluid interface moves into the continuous fluid stream and creates a blockage in the channel(Figure 2.2a). The upstream pressure builds until the pressure force overcomes the interfacial tension forces, and the droplet is "pinched" off the main stream. As the Capillary number increases (higher oil flow rates), the continuous stream cross-flow deforms the droplet such that the aqueous stream does not fully block the continuous flow channel. Similar to the dripping regime for flow focusing and co-flowing nozzles, monodisperse droplets form as the oil shear pulls droplets from the main aqueous stream. Recent experimental pressure measurements in T-junctions also have found that pressure oscillations still persist even in the dripping regime, suggesting that the dripping mechanism may not be entirely shear-driven[64]. Intuitively, as Ca further increases, the oil shear stretches the aqueous fluid into long, thin streams with unstable droplet detachment.

To ensure steady droplet generation in flow focusing, co-flowing, or T-junction schemes, aqueous and oil flow rates must therefore be sufficiently small to avoid inertial and shear-based jetting. This imposes a strict throughput limitation on the attainable flow rates and drop generation frequencies for a given nozzle. Thus, increasing throughput must be attained by adding parallel channels, and not by simply increasing flow rates.

It is important to note that dripping to jetting transition maps[51] indicate that interfacial tension forces should be significant in comparison to aqueous inertia or oil-induced shear forces in order to ensure steady dripping. However, high interfacial tension conflicts with another important design constraint for droplet microfluidics: emulsion stability. While droplet formation

may occur at a nozzle, the emulsion is at best meta-stable. For any non-zero interfacial tension, droplet surface area is minimized to decrease the surface energy of the emulsion such that two separate droplets are more stable as a single droplet. Decreasing interfacial tension using surfactants provides additional stability such that some emulsions remain stable for several years[65]. However, decreased surface tension also increases the Weber and Capillary numbers, increasing the likelihood of jetting at drop generation nozzles. These competing design constraints necessitate careful consideration of surfactant types and concentrations for optimal droplet generation and emulsion stability regimes.

For water-in-oil emulsions, surfactants such as ABIL EM 90 and Span 80 are typically mixed in organic carrier phases such as mineral or silicone oils[66]. Fluorocarbon oils such as FC-40 mixed with fluorosurfactants are popular carrier fluids for biological droplet applications. Since fluorocarbon oils are both hydrophobic and lipophobic, they are considered more biocompatible than lipophilic organic oils as fluorocarbon oils are not likely to interact with aqueous solutes, biomolecules, and cell membrane lipids[67]. Nonionic fluorosurfactants, which provide both emulsion stability and an inert inner droplet surface, are, however, difficult to obtain commercially but may synthesized using protocols presented in the literature[67-69]. Pickering emulsions can also be created using nanoparticle-stabilized interfaces[70-72]. More complete reviews of surfactants[66] and nanoparticle pickering emulsions[73] are available elsewhere.

2.2 Chemical Species Transport: Mixing and Isolation in Droplets

Due to small dimensions in microfluidic channels, Reynolds numbers (Re_c) are typically small, on the order of 1 to 100 or less. For reference, the channel Reynolds number is given by

$$\mathrm{Re_c} = \frac{\rho U_{max} D_h}{\mu}, \tag{2.3}$$

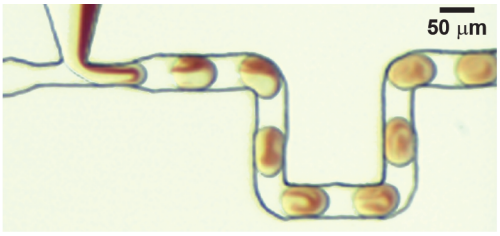

(a)

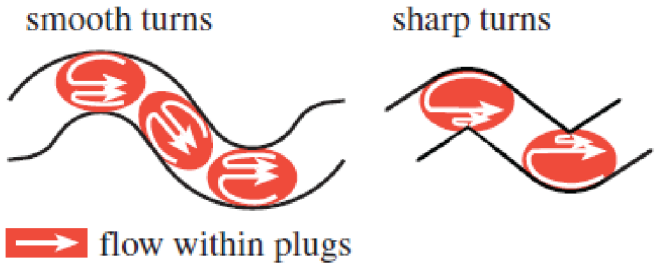

(b)

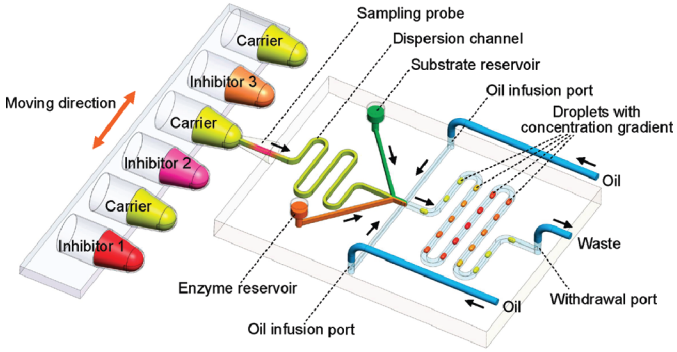

(c)

Figure 2.2. Mixing enhancements in microdroplets. (a)Multiple inlet fluid mixing in droplets generated at T-junction. Note the swirling and folding patterns indicative of internal advection[74]. (b)Mixing schematic in smooth and sharp turning devices with schematic flow arrows demonstrating mixing flow patterns[74]. (c)Example method for generating droplets with unique concentrations using multiple aqueous inlets upstream of the flow-focusing nozzle. Supply reservoirs are mechanically actuated to provide unique reagents to expand the experimental parameter space[75]. Copyright 2012, American Chemical Society. Parts (a) and (b) are reprinted with permission from [74], and part (c) is reprinted with permission from [75].

where ρ, U_{max}, D_h, and μ represent the fluid density, maximum channel velocity, channel hydraulic diameter, and dynamic viscosity, respectively. A low Reynolds number also implies a

relatively low Peclet number (Pe), which compares the advection transport to the diffusion transport as

$$\mathrm{Pe} = \frac{LU}{D}, \tag{2.4}$$

where U is a characteristic velocity (e.g. mean velocity), L is a characteristic length (such as the hydraulic diameter D_h), and D is a mass diffusion coefficient. Low Pe represents diffusion-dominated transport, while high Pe represents advection dominated mixing. While $\mathrm{Re_c}$ and Pe may be large enough in high-throughput applications to leave the viscous Stokes' flow regime (i.e., where $\mathrm{Re_c}$, Pe << 1), it is still below turbulent flow regimes better suited to mixing.

However, rapid mixing is essential for applications where reactions, measurement, and actuation must take place on millisecond (ms) or faster time scales, and where interrogation times in high-throughput devices are limited. In lieu of diffusive mixing, microfluidic channel geometries such as serpentines (Figures 2.2a and 2.2b) are often added to induce chaotic advection (secondary flows within channels and droplets which cause folding of layers of fluid onto each other). This can improve mixing rates to millisecond time scales[74,76,77] and facilitate an increase in surface areas between chemically reacting layers[78]. Initial droplet reagent concentrations can be controlled simply by pre-mixing samples, mixing samples at the drop generation inlet, or using gradient generators connected to multiple droplet nozzles to create wider experimental parameter spaces[75,79](Figure 2.2c).

For aqueous droplets in immiscible oil carrier fluids, delivery of reagents and other solutes to and from cells is prevented by the low solubility of the aqueous phase in the oil phase. However, some lipophilic oils can selectively dissolve trace amounts of water to concentrate aqueous solutes[80], or transport particles across the interface[81], but these effects are usually undesirable. A recent study noted that while hydrocarbon oils are not compatible with DNA

transfection of encapsulated cells in droplets due to reduced oxygen transport and reactivity with transfection reagents at the fluid interface, fluorocarbon oils were utilized to successfully transfect encapsulated cells[82]. Another study controllably lowered the fluorocarbon oil oxygen concentration that reportedly caused encapsulated blood cell sickling[83]. Despite adequate gas exchange for certain applications, aqueous droplet microfluidics still suffers from the inability to continuously perfuse fresh media to cell cultures to replenish nutrients and wash away toxic cell byproducts, often limiting encapsulated cell experiment time scales[23,84]. However, off-chip cell culture periods of up to several days are possible using gas-permeable storage materials with larger 600-700 picoliter (pL) droplets[35,85].

2.3 Beyond Aqueous Encapsulation

In addition to aqueous droplet formation, agarose and other polymer hydrogels have been employed to encapsulate and immobilize cells[86-91] or individual molecules[87,92] within monodisperse microspheres. In these applications, particle composition is carefully selected to control specific microcapsule mechanical, diffusive, and degradation properties. Typically, droplet generation encapsulates the cells within the precursors using typical flow focusing or other junction-type nozzles. Note that the viscosity and interfacial tension may change due to the addition of gel precursors, which could greatly affect the drop generation dynamics and limit throughput when compared to encapsulation in aqueous cell culture media[93]. In most cases, gel droplets are exposed to thermal or UV curing methods which must not harm encapsulated cells. Often, the resulting hydrogel microcapsules may also be re-suspended in a continuous phase of aqueous media so that longer-term cell studies are possible, although some of the

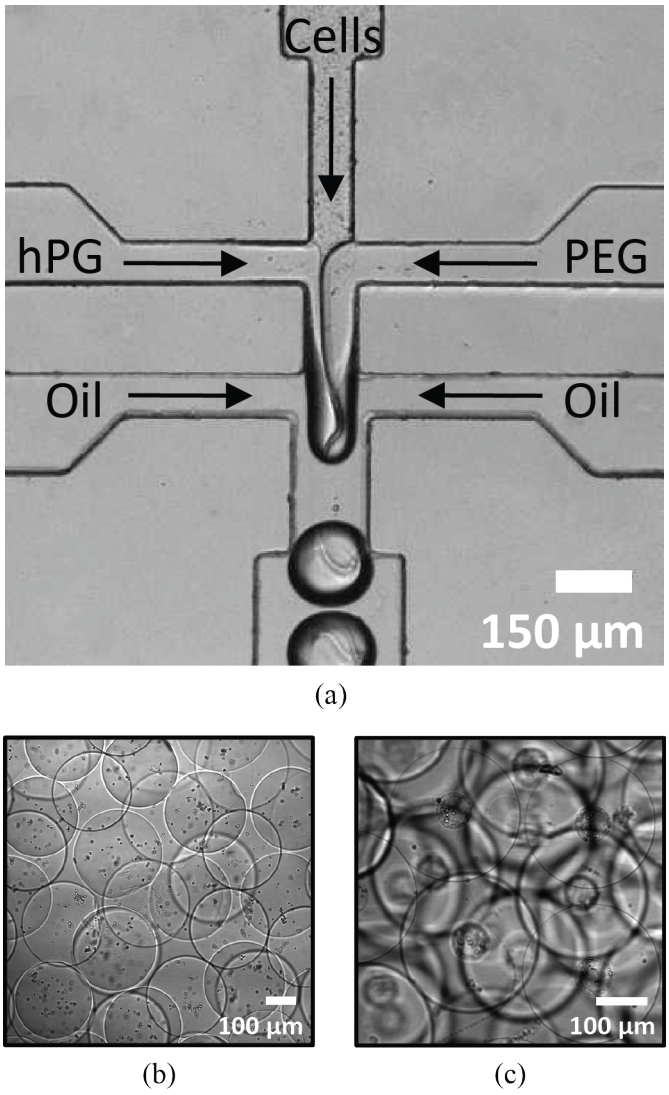

Figure 2.3. Cell-laden hydrogels fabricated using droplets. (a)Two sequential cross-junctions serve to form monodisperse, micrometer-sized precursor droplets which consist of polyglycerol (hPG), polyethylene glycol (PEG), and cells. (b) Yeast-cell-laden microgel particles formed by gelation of the droplets. (c) Core−shell-structured microgel with cells concentrated in the center of the microgel. Reprinted with permission from [94]. Copyright 2012, American Chemical Society.

benefits of droplet confinement are eliminated in a re-suspended environment. To highlight the ability of hydrogels to sustain longer-term experiments, agarose particles have been utilized in antibiotic resistance studies of *E. coli* cells[89] and in a seven day culture of *C. militaris* cells[90]. An additional study encapsulated and cultivated yeast cells in polyethyleneglycol

(PEG) and hyperbranched polyglycerol (hPG) without the use of cell-harming polymerization initiators[94](Figure 2.3).

Interestingly, multiple aqueous hydrogel precursor inlets upstream of the drop generation nozzle may be used to form so-called “Janus” particles[95-98] (Figure 2.4). When multiple precursor streams merge immediately upstream of the droplet generation nozzle, the fluids are not well-mixed in the droplet. Rapid curing following droplet formation therefore limits mixing and diffusion between the two droplet components to create particles with two distinct halves. Paramagnetic Janus particles, fabricated using one magnetic nanoparticle laden inlet stream and one non-magnetic inlet stream, provide not only the ability to move and sort cell-embedded hydrogel droplets in a magnetic field, but the capability to orient particles into large arrays for parallel manipulations[97].

Instead of simple cell immobilization in a gel matrix, more complex core-shell emulsions can also be utilized to trap cells inside porous capsules with tunable transport properties. In addition, double emulsions (water/oil/water) have been utilized to trap cells trapped within a polymer (whose precursor is soluble in the oil phase)[99-101] or other biomaterial (such as a lipid[102]) membrane. More recently, porous shell capsules were fabricated using a polymer-gold nanoparticle composite with versatile functional groups at up to 300 Hz rates with a demonstrated ability to encapsulate bacterial cells[103]. Note that these thin membrane and core-shell methods highlight one critical role of droplet microfluidics in synthetic biology[104,105] for both single cells and sub-cellular components. Additional materials and methods for core-shell microcapsules have been reviewed in depth elsewhere[106-108].

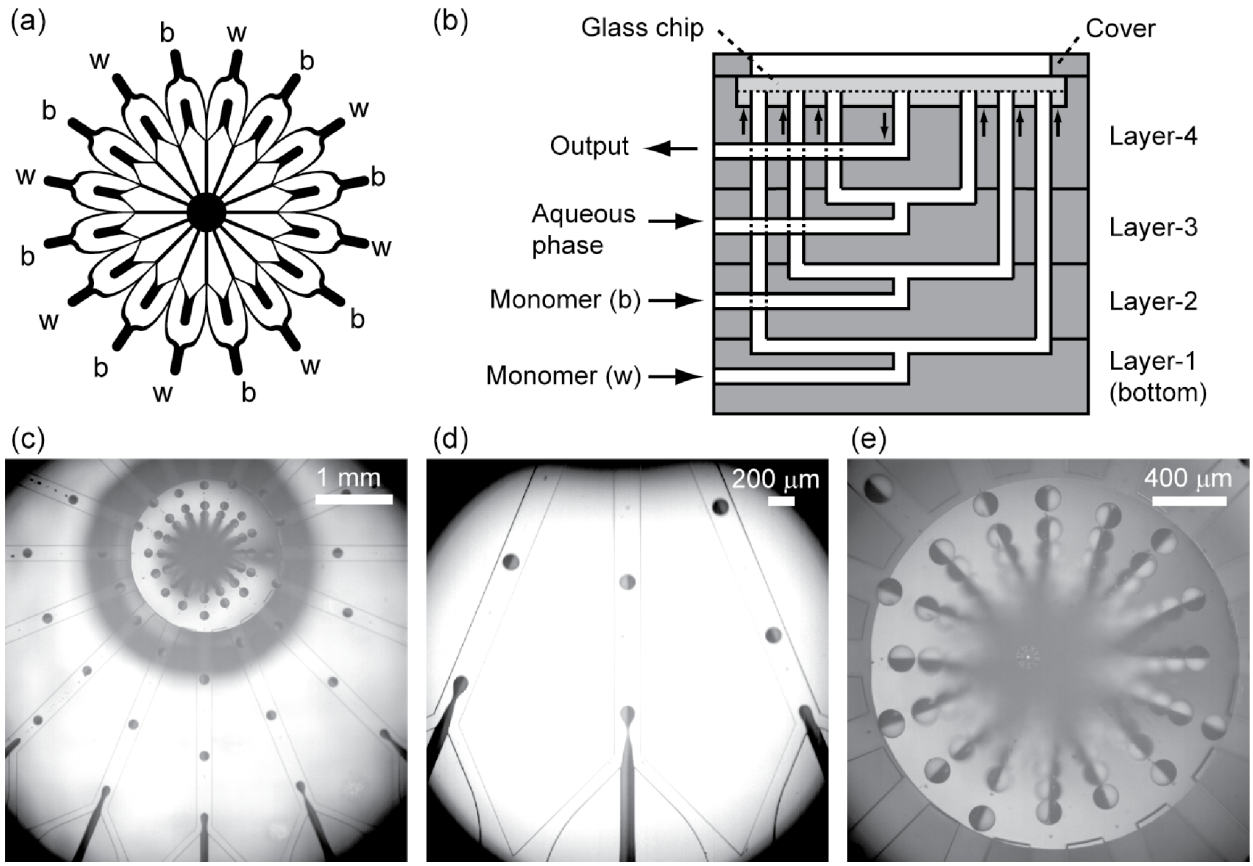

Figure 2.4. Parallel channel scale-up of Janus particle production. (a) Schematic of the microchannels on a chip. The "b" and "w" labels specify the inlet positions for the black and white monomers respectively. The aqueous phase is infused from the inner 16 inlets, arranged circularly with an outlet in the center. (b) Schematic of the layered internal device structure (side view). (c) Top view of the formation of biphasic droplets in the module. d) Magnified view of the co-flow geometries. e) Magnified view of the outlet port in the center of the chip. Reprinted with permission from [95].

2.4 High-throughput Droplet Actuation Methods

Parallel (multiplexed) droplet generation (Figure 2.4) can increase droplet production tremendously, but providing reliable downstream measurement and control of so many droplets has been much more challenging. To match the high-throughput droplet generation capabilities to downstream droplet processing capabilities, high-throughput actuation and measurement interfaces, data processing and analysis, and real-time feedback control are essential.

For droplet microfluidics at any throughput, actuation and sensing methods should be minimally invasive to preserve the viability and differentiation of encapsulated cells. Invasive methods are those which introduce pressures, shear stresses, electric and magnetic fields, and any changes which may alter a cell's phenotype. While serial methods which interrogate and actuate individual droplets one at a time have proven indispensible, they require parallelization of sensors and actuators to increase throughput further. For higher throughputs, goals include dynamic control, parallel (and ideally simultaneous) actuation and sensing, and droplet-specific tagging to track individual droplets or unique droplet characteristics, all with low rates of error, failure, and interference with natural cellular processes.

While others have reviewed single-cell investigation techniques[109,110] and microfluidic pumps[111,112] and valves[2] in depth, we focus this section on droplet microfluidic methods, both serial and parallel, and their potential for throughputs that compete technically and economically with existing technologies. It is not always straightforward to distinctly separate actuation and sensing methods, as the two preferably work in conjunction to achieve maximum throughputs. However, to address sensing, we must first address how droplets are actuated to provide conditions and appropriate time scales for reliable droplet sensing. The methods highlighted here in no way represent an exhaustive list of techniques in single-cell droplet microfluidics; rather, we attempt to highlight a few recent advances toward high-throughput applications. Additionally, we discuss methods that have been demonstrated for actuation and manipulation of suspended cells since these principles may be expanded for use with droplets in the future.

2.4.1 Extracellular Environmental Control

While microfluidic droplets provide unique microreactor conditions for test samples, often droplet environments must be modified by introducing new aqueous fluids and reagents, extracting fluid and cells from droplets, re-suspending cells in a bulk aqueous environment, or modifying droplet temperatures. Passive droplet splitting provides a mechanism to create multiple droplet samples of the extracellular fluid environment. Coalescence mechanisms provide means for introducing controlled volumes of reagents and media to cell-containing droplets.

Splitting and coalescence have been well-reviewed elsewhere[45,46]. Briefly, passive splitting is often accomplished using a bifurcating T-junction[113,114] or Y-junction[115]. In both T- and Y-junctions, droplet breakup dynamics have shown dependence on capillary number Ca and droplet size[113,116]. Symmetric splitting junctions[113] (equal-sized outlet channels each with equal flow) provide equal-sized daughter droplets while asymmetric junctions[117] provide one larger droplet and one smaller droplet. It is important to note that passive splitting methods do not control which daughter droplet contains the encapsulated cell or cells.

For passive coalescence, altered channel geometries can induce coalescence in low-stability emulsions simply by bringing a droplet into direct contact with another droplet or bulk fluid interface[118-120]. Alternatively, patterned biphilic surfaces provide spatial control over droplet wetting on a small hydrophilic area of the channel wall. When enough droplets collect and mix on the wetted surface, the drag force overcomes the droplet capillary force, and the combined droplet detaches[121]. Droplets may be actively coalesced using electric fields (on the order of 50-200V in some studies[122,123]) oriented parallel to the two-phase flow. Additionally, focused lasers can locally heat fluid interfaces at the point of droplet contact to

induce interfacial tension gradients and Marangoni flows in each droplet to result in coalescence[124].

When using electric fields and focused lasers for droplet control, care must be taken to avoid damage to encapsulated cells if cells are to remain viable for later interrogation. One study characterized droplet-encapsulated cell electroporation for both gene delivery and cell lysis using droplet throughputs on the order of 40-250 Hz and applied voltages on the order of 5-10V[125]. While electroporation voltage thresholds are based on many factors (e.g. fluid electrical properties, droplet sizes, droplet velocities), these values suggest precluding droplet electrocoalescence techniques in some encapsulated cell applications. Laser-induced coalescence applications may be limited when extended cell viability is required. Rapid photolysis using focused lasers has been demonstrated for enzymatic analysis of droplet-encapsulated cells[126]. Heating using laser absorption has been exploited to reduce droplet polymerase chain reaction (PCR) cycle times to around 10 seconds[127,128]. In the referenced laser heating studies, stationary droplet samples are cycled between approximately 60°C and 95°C while reporting laser powers on the order of 30-70 mW. The laser is defocused to apply a uniform intensity across the droplets with diameters on the order of 300-400 μm. While electric fields and lasers provide tools for coalescence, cell lysis, and thermal control, it is important to quantify induced stresses to avoid unintentional cell death.

2.4.2 Droplet Trapping

Measurement of microfluidic droplet characteristics requires, for example, optical, magnetic, chemical, or thermal interrogation droplets which may be moving at a relatively high speed (up to hundreds of mm/s) through finite microscopic fields of view. Therefore, matching

the sensor interrogation time to the droplet lifetime in the field of view is a critical parameter when balancing the need to accurately assess droplet contents versus the desire to maximize throughput. The sensor time scale places an upper limit on the velocity at which droplets may be actuated for a single measurement in time if actuation follows sensing, one drop at a time.

With cellular processes occurring on time scales from sub-millisecond or less to hours and days, multiple measurements may be required to obtain transient droplet profiles. Despite the requirement to stop the flow, which limits the maximum throughput, static droplet and cell traps provide some of the more established methods for detecting droplet properties with maximum resolution over a wide range of time scales. U-shaped flow-induced traps provide a method to "catch" droplets in a flow field while a continuous oil flow assists in thermal and chemical transport (depending on oil solubility and interfacial properties) and in generating secondary mixing flows within droplets[129,130]. U-shaped traps may also be designed to contain multiple droplets[131,132]. While mechanical droplet traps have the benefit of containing cells indefinitely for experiments with longer time scales, sub-millisecond kinetics were obtained using only droplet contact traps[132]. As opposed to droplet merging reactions, droplet contact provided a controlled reaction interface where the temporal resolution was not limited by millisecond droplet mixing times. Three-dimensional packing schemes have also been utilized to passively arrange up to around one million droplets in a wide-field array. As a result, simultaneous imaging of multiple droplet planes is possible[115,133].

Several trapping mechanisms also allow for quasi-continuous flow where droplets are stopped only temporarily. One two-dimensional array coined the "dropspot" passively captures droplets in continuous flow. This works because the interfacial tension forces favor droplet locations within traps as spheres rather than in the narrow regions between traps. Notably, these

devices can also release droplets by increasing the pressure differential across the channel following droplet interrogation[134,135]. More integrated microfluidic designs use series of complex valves such that media and reagents can be added to any one of hundreds of addressable chambers[136-138]. While these chambers have been demonstrated with trapped cells, droplets may also be trapped and subsequently released following interrogation.

2.4.3 Mechanical and hydrodynamic sorting

For continuous flows, mechanical and hydrodynamic methods can also provide passive sorting of cells and droplets. For example, pinched flow fractionation (PFF) utilizes a narrow channel followed by a sudden expansion to a wide channel to separate particles based on size[139]. In addition, deterministic lateral displacement (DLD) utilizes pillar arrays to sort particles based on size[140], although this method may be susceptible to clogs. Recently DLD has also been applied for cell-containing droplet sorting[141]. Passive hydrodynamic effects in rectangular channels also provide a sorting mechanism. At sufficiently high flow rates, objects such as particles, cells, and droplets tend to passively equilibrate to discrete cross-sectional "focusing" positions in both cylindrical and rectangular channels[20,142,143] (see Chapter 3). Combining this straight-channel effect with spiral[15,144] and asymmetrical[17,19] channels introduces secondary Dean flows, forcing larger objects to move toward the inside channel wall while smaller objects stay further from the wall. A number of discrete channel outlets provide separation based on size, although current devices typically require a semi-empirical calibration of flow rates to optimize the separation efficiency.

2.4.4 Optical Sorting

Optical methods include the use of lasers to control cells and particles[145]. The optical tweezers use a single laser to trap a dielectric particle in three dimensions[146]. For aqueous droplets, optical tweezers are not feasible when the refractive index of oil is greater than that of the aqueous phase (~1.33 for pure water), but optical vortex traps have been utilized to facilitate trapping in this case[147]. Optical switches can also deflect droplets and cells for sorting and have achieved actuation rates in the 4 ms range[148]. More recently, optical pulling of dielectrics has also been discovered, although achievable forces are relatively weak[149].

2.4.5 Magnetic Sorting

Magnetic activated cell-sorting (MACS) involves tagging cells and molecules with functionalized magnetic nanoparticles or simply suspending magnetic nanoparticles in droplets. When magnetic particles are uniformly suspended in all droplets, continuous flow actuation must be based on a triggered change in magnetic field. Controlling the magnetic nanoparticle concentration also provides variable deflection (with force proportional to concentration) of droplets in flow[150]. However, magnetic nanoparticles bound to specific proteins[151] and cells[152-154] prior to encapsulation can provide both sensing and sorting actuation without direct control of the magnetic field[155]. Studies have reported functional binding to yeast[153] and bacteria[152] cells without loss in cell viability for selective magnetic manipulation. Magnetic droplet sorting has been demonstrated at relatively low rates of around 10 droplets/s[150] and 30 droplets/s[156], while cell sorting has been demonstrated using flow velocities on the order of 0.1 to 1 mm/s[157].

2.4.6 Acoustic Sorting

Surface acoustic waves (SAW), often created using piezoelectric actuators[158], are also being exploited to deflect droplets into specific sorting paths. Acoustic waves provide an attractive method for manipulation of label-free particles and droplets because forces depend only on droplet size, shape, and density[159]. One study utilized acoustic forces to perform both size-based separation of polystyrene particles and density based separation of red blood cells, platelets, and leukocytes[160]. Additional studies demonstrate cell[161] and droplet[162] sorting at kHz rates.

2.4.7 Electric Sorting

In a similar manner to surface acoustic waves, electric fields can also deflect and sort droplets. In commercial FACS machines, droplets are electrostatically charged, and droplet sorting is achieved by switching electric fields[40], a phenomenon that has also been utilize to deflect droplets between outlets[163]. Dielectrophoresis (reviewed elsewhere[164]) has also been used to deflect droplets in fluorescence activated droplet sorting (FADS) at rates up to 2 kHz[165]. Dielectrophoretic methods using marker-specific labeled cells (where labeled cells exhibited dielectrophoretic deflection and unlabeled cells did not) have achieved rare cell sorting at rates of 10 kHz[166].

2.4.8 Droplet Labeling and Indexing

For high-throughput screening, processing millions or more droplets on short time scales entails very short interrogation periods for each droplet. For biological processes occurring on longer time scales (minutes, hours, or days), tracking individual droplets in static arrays for the

entire process is not feasible while still achieving a high throughput. Ideally, one could interrogate a unique droplet, temporarily store it, and recall the same droplet later at discrete time intervals to measure its transient quantities.

Studies have demonstrated barcode identification of unique non-spherical particles by utilizing UV curing of polymer precursors with variable optical mask patterns in both continuous[167] and stop flow lithography[168]. As an alternative strategy for droplet identification, suspended quantum dots[169-171] in the extracellular fluid, may provide an additional tool which is easily adaptable for spherical particle and liquid droplet identification. Briefly, fluorescent quantum dots are suspended in droplets at *N* discrete concentrations using microfluidic gradient generation combined with standard drop generation techniques. When combined with a discrete range of *M* fluorescent colors, (N^M-1) spectral codes are possible[171]. For example, a combination of 30 discrete intensity levels with 5 colors leads to over 24 million unique codes, although mapping each individual droplet to a unique code is not a trivial challenge. Magnetic nanoparticle concentration gradients could also assist as an additional marker, as droplet and particle deflections are proportional to the magnetic nanoparticle concentration and orientation[150].

2.5 High-throughput Droplet sensing methods

Prior to initiating many of the previously mentioned actuation and sorting mechanisms, sensing is required to decide on the appropriate actions. Sensors provide a measure of optical, electromagnetic, or chemical output that must be quickly received, interpreted, and converted to an actuation response. Although droplet-encapsulated cells remain the focus of this review, here we also include several methods which have been developed for droplet-encapsulated molecular

studies. These methods are relevant when detecting small concentrations of molecules and proteins which may be expressed or absorbed by encapsulated cells.

2.5.1 Fluorescence Droplet Sensing

Though some cellular proteins and other biomolecules exhibit auto-fluorescence, they often must be tagged using targeted binding of fluorescent dyes or particles. Several techniques are highlighted here, but additional methods are reviewed in depth elsewhere[110,172].

To optimize throughput using fluorescent methods, one must carefully weigh the importance of image resolution and brightness with the ability to interrogate a larger number of droplets in parallel. Wide field fluorescence utilizes a fluorescence microscope, fluorescence-inducing light source, and high resolution camera. Due to the wider fields of view, multiple droplets may be interrogated in parallel (and in dynamic and static parallel channels[173] and arrays) for maximizing throughput, although the increase in throughput comes at the expense of decreased resolution[28]. Serpentine channels have been employed to move samples across the field of view at discrete time intervals for fluorescent imaging, increasing total on-chip time for transient experiments[174].

For smaller regions of interest, focused lasers are used to induce fluorescence. Laser-induced fluorescence has made it possible to detect molecules on the 10^{-12} M scale[175]. Precise fluorescence activation is more complicated in moving droplet flows but has been successfully implemented. In an integrated fluorescence activated droplet sorter (FADS), laser induced fluorescence was utilized to dielectrophoretically sort continuously flowing *E. coli* cells encapsulated in droplets based on enzymatic activity at a rate of 300 cells/s[165].

One study combined confocal fluorescence microscopy with fluorescence resonance energy transfer (FRET), which uses fluorescent stimulation of one molecule to induce fluorescent emission from an adjacent molecule, to detect millisecond droplet reaction kinetics[176]. Additional studies have used confocal fluorescence microscopy to detect single DNA molecules in static droplets[130], cell protein expression in moving droplets[36], and single molecule detection with droplet flow velocities up to 1 mm/s[177]. Additional droplet techniques include fluorescent polarization, demonstrated for protein detection[178], and fluorescence *in situ* hybridization (FISH), demonstrated for rare cell identification, although the latter method is lethal to cells[9].

2.5.2 Droplet Sensing by Mass Spectrometry

Mass spectrometry (MS) uses a label-free system which ionizes sample compounds to generate charged molecule fragments for detection. The ionization process is invasive and deadly to cells, so post-measurement cell cultures are not possible. While mass spectrometry has been demonstrated using continuous flow microfluidic devices, the continuous oil phase in droplet microfluidics provides interference with MS techniques such that droplets must be coalesced into continuous flow systems for analysis[28]. Electrospray ionization MS (ESI-MS) has been developed to re-introduce droplet streams into new aqueous streams for aerosol droplet generation and MS analysis at encapsulated droplet rates on the order of 0.1 Hz[179,180], relatively slow for high-throughput applications and with high dilution negating some of the benefits of droplet confinement.

2.5.3 Droplet Sensing by Raman Spectroscopy

Raman spectroscopy utilizes non-invasive, label-free interrogation of single cells and droplets using a spectrum of Raman bands of molecular vibration initiated by an incident laser to serve as fingerprint of a cell. Notably, unique bands exist for different sub-cellular components including proteins and DNA[181]. Traditional Raman signal acquisition times are on the order of minutes, as only a tiny fraction of photons undergoes Raman scattering[182,183]. This leads to low throughput in Raman activated cell sorting (RACS) platforms[184]. Interrogation times may be reduced, however, by increasing the laser power[182,184], or by using enhanced Raman spectroscopy techniques. Surface-enhanced Raman scattering (SERS) detects molecules attached to noble metals[182,185] such as gold. SERS was used to investigate the internal contents of gold-nanoparticle laden shells fabricated using microfluidics[103] and to reduce the interrogation time of *E. coli* cells to 1 s[186]. More recently, surface-enhanced resonance Raman scattering (SERRS) systems have been demonstrated which detect multiple droplet analytes in real time at a rate of 4 droplets/s[187] and interrogate moving droplets at sub-ms time scales at average rate of 13.3 droplets/s[188].

2.5.4 Electric Droplet Sensing

Several studies have used insulated electrodes placed within the top and bottom channel surfaces to measure capacitance as droplets pass between the electrodes. In these studies, the droplet changed the overall dielectric constant across the channel at time scales on the order of 10 ms[189,190]. Aqueous droplet flows in silicone oil induce a change in the measured voltage or capacitance across the electrodes to serve as a droplet detector and droplet velocity measurement device when multiple electrode pairs are included[190]. This simple method using

only voltage signals provides a valuable alternative to optical droplet detection and velocity measurement where channel materials must be transparent. The measured signal is also proportional to droplet size and was calibrated to quantify droplet sizes for pure water, providing discrete volumetric measurements without using optical imaging. Depending on how droplet composition affects its dielectric properties, capacitive sensors could be exploited to measure droplet composition (including detecting which droplets contain cells and which do not), and transient droplet reactions. Similarly, electrodes were utilized to quantify droplet flows using impedance measurements[191-193], with one study reporting measurement times on the order of 100 ms[191].

2.5.5 Magnetic Droplet Sensing

As previously mentioned, functionalized magnetic nanoparticles can be tailored to bind to specific cells and molecules for their use as both sensor and actuator in droplet microfluidics[155]. Additionally, studies have used magnetic nanoparticles to interrogate droplets using nuclear magnetic resonance imaging (NMR) coils wrapped around channels, although throughput was relatively low because of the need to stop the flow for 16 s for sufficient droplet sensing time[194,195]. Additional studies have used microfluidic NMR hand-held devices (without droplets) to detect bacteria in unprocessed biological samples[196,197] and for cancer cell detection[198]. A more detailed review of magnetic biosensors is available elsewhere[199].

2.5.6 Particles and Droplets as Sensors

In some cases, suspended droplets and hydrogels themselves can function as sensors. Stimuli-responsive hydrogels can be engineered to change size based on temperature, pH, droplet composition, and electric fields[200-202]. DNA may also be used as a reversible cross-linker to modulate the hydrogel rheological and mechanical properties and to provide for controlled interactions between DNA and other molecules and cells[203]. In another study, oxygen-permeable PDMS microparticles were embedded with oxygen-sensitive dye for an optical readout of oxygen concentration[204]. Liquid droplets have also been used to monitor reactions if those reactions induce changes in osmotic pressure. As a result, small but measurable volumetric water transfer between droplets provided quantifiable reaction metrics[205].

2.6 Expansion to High-throughput Applications

In previous sections, we have addressed droplet mechanics and methods for measuring some of the most relevant properties of cell-laden droplets. Here, we attempt to place these methods in the context of specific biomedical applications, a number of which have been addressed in recent reviews. One review[27] highlighted how the absence of dilution in droplets allows for faster accumulation of biomarkers to reduce clinical diagnostic times for detecting antibiotic responses of bacteria in human blood plasma[206]. This review also emphasized how volumetric confinement in droplets allowed for enzymatic amplification of cell surface protein biomarkers[207]. Confinement also allowed for the detection of rare mammalian cells via cell lysis within droplets followed by PCR amplification of DNA[208]. Several reviews[27,209] note how confinement reduces the number of cells required to mimic quorum sensing (high cell density) environments for cell-growth assays[12,23]. Cell confinement has also allowed for the

detection of rare slow-growing cells since fast-growing cells cannot dominate a mixed population, as is the case in a bulk sample[210]. Given that a number of single-cell droplet reviews have been recently published, here we focus on just a few notable studies based on their high-throughput potentials. These studies have not only allowed biological questions to be answered in new ways but also represent significant progress in high-throughput single-cell droplet microfluidic applications.

Based on the discussions from previous sections, it is apparent that high-throughput applications of droplet microfluidics have been limited by the ability to sense droplet contents and sort droplets at the kHz rates at which droplets can be generated. Significant efforts are now being directed to apply on-chip dielectrophoretic sorting of droplets, based on fluorescence interrogation, to biological applications that require a high throughput. These include screening cells for enzyme activity[165], screening drug libraries for cytotoxicity[35](Figure 2.5), and screening engineered proteins for directed evolution[211]. This represents the logical extension of fluorescence-activated cell sorting to a drop-based system, and the throughputs have now reached about 2,000 droplets per second, a significant fraction of the best rates achieved for commercial FACS machines. In contrast to FACS, however, droplets enable sorting according to accumulated changes in the extracellular media that are induced by cell-specific processes, and this can lead to time-integrated measurements that are not limited to intracellular processes. This is an impressive capability and will clearly have application to many critical problems in biotechnology and biomedicine.

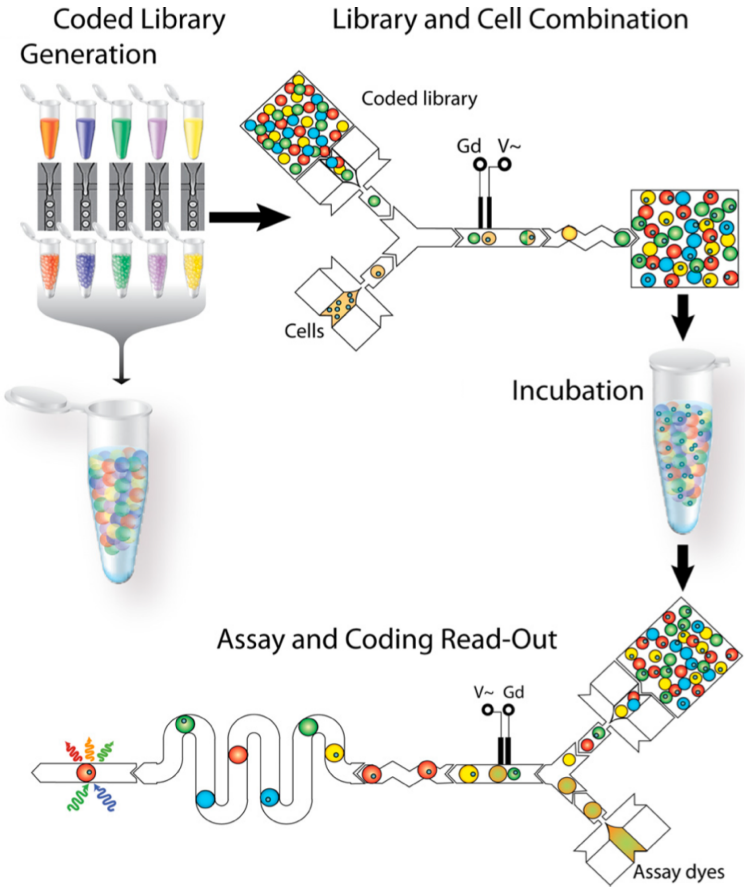

Figure 2.5. Droplet-based platforms for toxicity screening of single cells. Besides integrating cell encapsulation, pairwise droplet merging, and reinjection of encapsulated cells, at combined rates of 100 cells per second, this study used eight concentrations of fluorescent dye to encode each droplet by its drug concentration. Copyright 2009, National Academy of Sciences, U.S.A. Reproduced with permission from[35].

However, nutrient depletion by encapsulated cells sets an important time limit on experiments since even single cells will eventually run out of nutrients and accumulate toxic levels of waste products in their drop. Though it is inherently impossible to replenish media in droplets without sacrificing some degree of chemical isolation, it is possible to exchange the extracellular fluids while still preventing entry of biological contaminants, e.g. bacteria. In one type of approach, gel beads are formed from emulsion drops, with or without cells inside, and they are then re-suspended in aqueous media to allow for fluid exchange without cell-cell contact. Since this barrier may only be necessary at the oil-water interface, it could be better in

some cases to create a polymer shell with a defined pore size at this interface in order to limit the effects of gel precursors on events in the drop interior (c.f. a subsequent section on capsule density). Washing in aqueous media then facilitates a direct coupling of encapsulated cells to standard FACS[212,213]. Similarly, w/o/w emulsions can be used directly in FACS machines yet retain all the benefits of encapsulation[214,215].

Moreover, though drop-based FACS is appropriate for many applications, one can aim for even higher throughputs, and in particular, for passive droplet sorting mechanisms that select droplets according to specific properties of the cells inside them. To see why passive sorting can be desirable, consider that although commercial FACS machines can sort many thousands of cells per second with multi-color probes, this instrument is expensive, takes up significant lab space, and requires a trained technician to run properly. On the other hand, magnetic activated cell sorting can isolate rare cells from a large mixed sample by specific adhesion of coated magnetic beads to cell membrane proteins. Though less specific than multi-color FACS, the key is that separation is done in parallel as a single batch operation with an inexpensive magnet.

Furthermore, there are numerous cell separation approaches which do not require active control of individual cells. These include affinity-based capture[216], size-based separation by deterministic lateral displacement[140] or inertial focusing[20], and density-gradient centrifugation[217], among many others that rely on multiple physics modes, as reviewed elsewhere[218]. The key to each of these is that sensing and actuation are intrinsically linked so that control per se is not required on a cell-by-cell basis. This greatly simplifies operation even at ultra-high rates through simpler parallelization. Because many of the same principles for cell separation might in theory be adapted to droplet separation, one promising area of future research would be to find robust means to precisely change the sortable properties of droplets in

response to the phenotype exhibited by cells inside each drop. Droplet size, density, and viscoelasticity are the obvious physical properties which, if modified by a cell, could lead to passive separation of the associated droplets. At first glance, these would seem to require quite large efforts by cells and do not suggest specificity in sorting. Nevertheless, in highlighting three recent approaches, it becomes clear that each avenue is possible for cell-based assays.

2.6.1 Droplet Size

Inert fluorocarbon oils are notable for their impermeability to aqueous and lipophilic molecules and high gas exchange, making them highly desirable for cell-based assays. However, this chemical segregation is not absolute, and recent works[205,219] have taken advantage of the tiny but nonzero mobility of water in FC-40 to turn monodisperse droplets into osmotic sensors for chemical reactions(Figure 2.6a). Notably, the authors observed that water migrated through the oil over the course of several hours in response to solute depletion by cellular metabolic activity, moving water from yeast-containing droplets to nearby empty droplets in a hexagonal close-packed droplet array. This was shown to result from osmotic pressure differences created by growing cells. Yeast cells ultimately exhausted their nutrients such that drop volume stabilized at about half its initial value after 33 hours, where no change in volume was seen for dead cells or those in drops without nutrients. The appeal of their approach for high-throughput, cell-based encapsulation is that droplet sorting could be done in parallel based on size alone without the need to actively interrogate and sort each droplet individually. This allows enrichment of cells that continue to grow over several hours in drops from inactive cells or empty droplets, potentially yielding methods to isolate pathological cell clones based on their

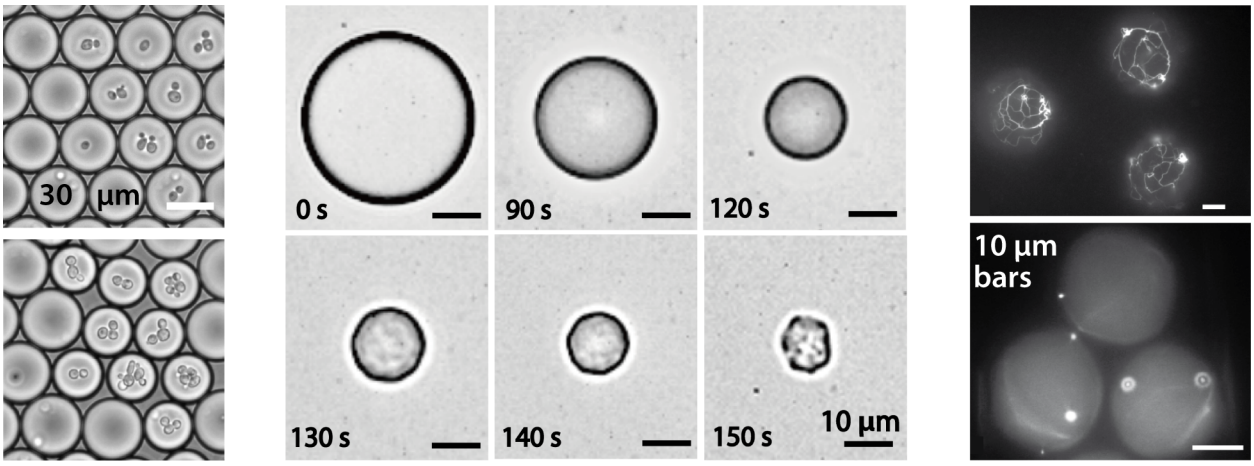

(a) (b) (c)

Figure 2.6. Strategies to control the physical properties of cell-laden droplets. (a) Solute depletion by yeast cell metabolism leads to osmotic shrinkage of cell containing drops over 30 hours of culture[205], yielding size-based droplet sorting capability[141]. (b) Thin-shell porous capsules were formed by partial dehydration of droplets in the presence of host-guest chemicals[103]. After resuspension in water, capsule density is determined by encapsulated cellular materials, enabling separation by density gradient centrifugation. Besides encapsulation of cells in drops filled by a biodegradable extracellular matrix, (c) droplet viscoelastic properties could be modulated by shifting the balance between growth and disassembly of actin filaments (top) or microtubules (bottom)[220]. Parts (a) and (c) reproduced by permission of the Royal Chemistry Society, DOI: 10.1039/C2LC20971C and DOI: 10.1039/C0LC00046A, respectively. Part (b) reprinted with permission from AAAS.

resistance to therapeutics added to the media. In fact, in a prior study, deterministic lateral displacement was used to separate yeast-containing drops at 12,000 drops per second due to the osmotic shrinkage of cell-containing droplets[141].

2.6.2 Capsule Density

Interestingly, one recent study[103] reported a simple approach to create porous capsules through self-assembly of a supramolecular coating as a thin, rigid, film along the FC-40 oil and water interface(Figure 2.6b). Specifically, the authors mixed a host molecule with two guest molecules just upstream of a T-junction for drop formation and observed that a ternary complex formed at the droplet boundary which solidified on partial dehydration of the drop. After cell encapsulation, the difference in density between the capsule and the surrounding aqueous media

is due entirely to the presence of cells plus a thin shell, so capsules could be fractionated according to the number of cells in a capsule and their densities, enabling sorting by centrifugation.

2.6.3 Droplet Viscoelasticity

A third recent report described a step along the way to creating artificial cells from microfluidic droplets. Specifically, the authors encapsulated *Xenopus* egg extracts and observed the self-organization of microtubules and actin filaments in droplets. Because these events are under complex biological control, it is possible in theory to switch between formation and degradation through regulatory controls. However, it is not clear if these intracellular structures could be coupled to the activities of encapsulated cells through specific cell secretions. Nevertheless, if this were possible, it would allow cells which secrete particular biomolecules to modify the mechanical properties of their encapsulating droplet into a form that is highly resistant to internal flow (filament growth), or one that behaves normally (degradation), allowing passive separations based on differential droplet migration according to viscoelastic properties(Figure 2.6c). In addition, it should be possible to encapsulate cells in specific extracellular matrix materials to select for cells that are able to degrade their matrix.

Looking to the future, it will be important to increase the specificity and flexibility of passive droplet separation methods. One interesting approach could be to self-assemble lipid rafts into the oil-water interface, among a larger coating of stabilizing surfactants, as a platform for receptor-ligand interactions. For instance, receptor domains on the aqueous side of the droplet surface could be made to change conformation on the oil-phase side after specific interaction with ligands secreted by the cell. If these changes led to adhesion of the lipids to

corresponding motifs presented on channel walls, affinity-based capture of droplets could become possible. In fact, one recent study grafted lipid patches onto soybean oil droplets in an aqueous continuous phase to generate receptor-ligand-like interactions between the droplet surface and a T-cell line[221]. Alternatively, through the further development of artificial cells in droplets, one can envision the use of combinatorial interactions among droplet pairs across an artificial lipid bilayer[222], that includes specific membrane proteins which cleave the drop-drop connections on exposure to a particular cell secretion. Or, droplets could become sticky only when cells secrete the target molecules. Either way, separation could then be accomplished by differential centrifugation. The key benefit in these approaches would be the high degree of specificity afforded by receptor-ligand interactions, and the passive manner of sorting.

2.7 Final Thoughts on High-throughput Droplet Applications

In the past ten years, droplet microfluidic platforms have provided a new way to carry out single-cell and biomolecular experiments for drug discovery, “omics” studies, and rare cell detection. Downstream measurement and actuation of droplets provides a major challenge to reaching this high-throughput potential. Automated systems must acquire and comprehend massive amounts of data to make decisions in the tiny fraction of a second that a particle sits within a small region of interest. When biological processes take place on longer time scales, the system must either slow droplet speeds at the expense of throughput, or employ methods which can interrogate, store, and reacquire a unique droplet over time. Indexed droplet tracking has been recently explored using quantum dots, but much room for improvement remains.

Highlighting the challenges above should not overshadow the many recent successes in droplet microfluidics. Droplet-based PCR methods have demonstrated gains for protein

engineering and directed evolution studies using smaller amounts of costly reagent volumes. Microfluidic lab on chip devices such as the “FADS” system utilizing fluorescence sensing and dielectrophoretic actuation have made significant progress toward high-speed automated sorting, reaching 2,000 droplets per second using an on-chip device and microscope. In recent years, data acquisition times for single-cell Raman spectroscopy have been reduced from minutes to sub-second time scales. Continuing on the path to commercial successes will take a truly interdisciplinary understanding of the fluid mechanics, chemistry, physics, biology, computer science, materials science, economics, and personalized medicine to bring the high potential of droplet microfluidics to full fruition.

Chapter 3

Inertial Microfluidics

While first discovered experimentally in macroscale pipe flow[13,142], the tendency of particles to migrate across streamlines has more recently been applied to microchannel flows. "Inertial microfluidics" contradicts the perception that small channel dimensions imply very small channel Reynolds numbers ($Re_c << 1$). Here,

$$Re_c = \frac{\rho U_{max} D_h}{\mu}, \tag{3.1}$$

where ρ, U_{max}, D_h, and μ represent the fluid density, maximum channel velocity (for the undisturbed flow), channel hydraulic diameter, and fluid dynamic viscosity, respectively. Analytical work[223,224] shows that in this Stokes' flow regime, where inertial effects are neglected, cross-stream migration of rigid particles is not possible. However, for channel diameters on the order of ten microns and modest flow velocities on the order of 10 cm/s, Re_c is on the order of one (using water's properties). As a result, inertial terms in the Navier Stokes equations often cannot be neglected.

3.1 Inertial Focusing

In both axisymmetric and rectangular channels, the velocity gradient in parabolic flow induces lift both due to the shear gradient and to particle spin. The result is a lift force away from the channel centerline. Note that the shear lift typically dominates the rotational lift, especially away from the channel walls[143,225,226]. As the particle approaches the wall, a repulsive force opposes the shear gradient and rotational lift until the forces balance at an equilibrium

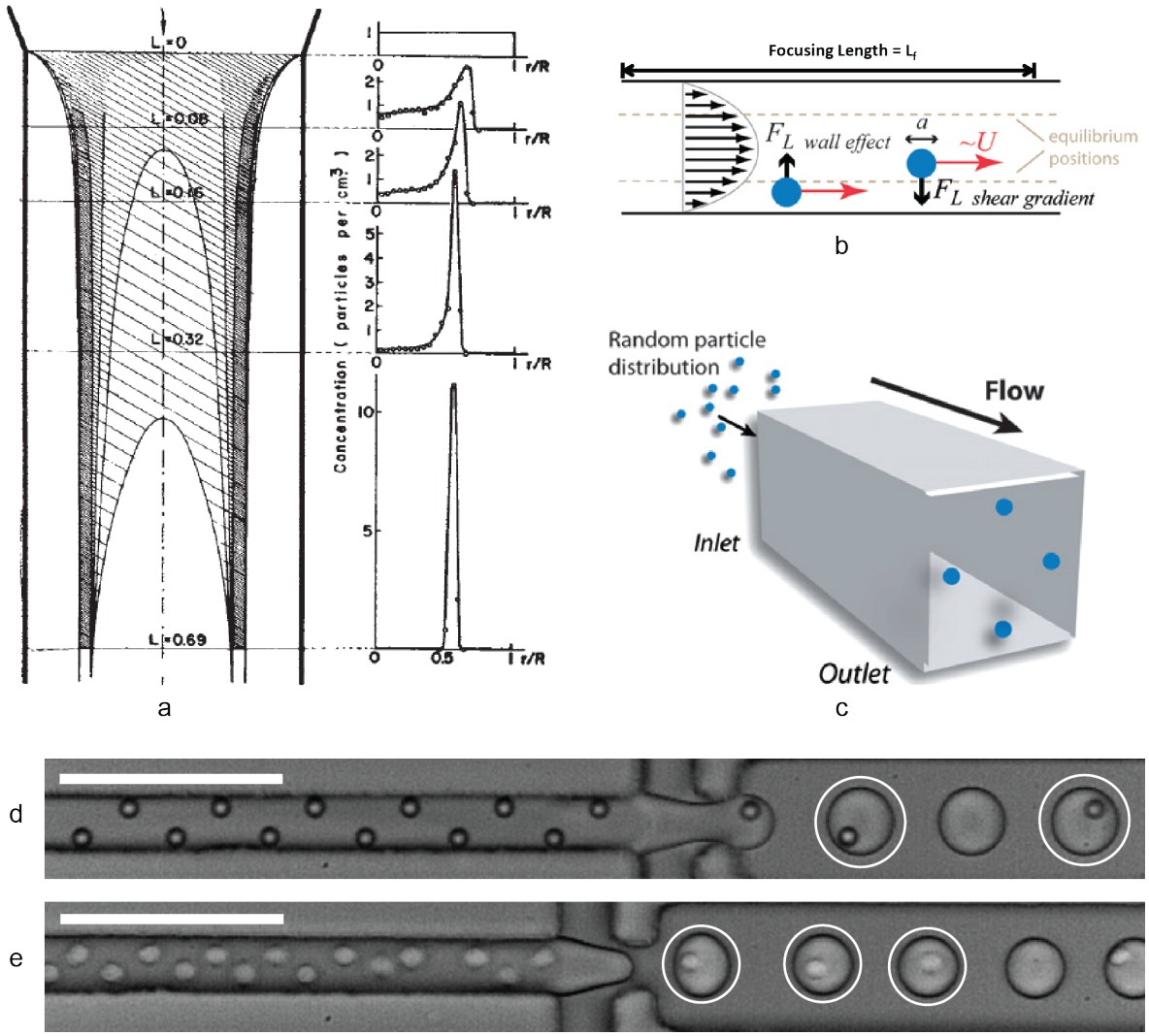

Figure 3.1. Inertial and droplet microfluidics. (a) Work from Segre and Silberberg[13] showing a randomly dispersed particle inlet in a cylindrical channel. The plots on the right show the particle distribution to the Segre-Silberberg radius r/R ~ 0.6. (b and c) Schematics from [20] illustrating the force balance leading to two equilibrium positions in each lateral direction (b) and a 3-D schematic (c) showing four quadrilaterally symmetric equilibrium positions in rectangular channel flow. (d and e) Ordering of two staggered trains of particles (d) and cells (e), which are exploited to control encapsulation of single cells in droplets. Scale bars in (d) and (e) represent 100 μm.

position[20]. In axisymmetric pipes, particles migrate to form an equilibrium annulus at the Segre-Silberberg radius (Figure 3.1a) [13,142]. In square and rectangular microchannels, computational[143] and experimental[18,143,227] studies show that there are four equilibrium nodes (Figure 3.1c) centered at each of the channel faces. One numerical study has noted an additional four equilibrium positions in channel corners[228], although corner equilibrium

positions have only been experimentally confirmed using scanning fluorescence microscopy at high Re_c (~158)[229]. For non-square rectangular channels, two focusing positions, parallel to the short channel dimension, are common. This equilibrium position has been shown to depend in part on particle size, flow rate, and channel geometry. The particle Reynolds number Re_p is defined as

$$Re_p = Re_c(a/D_h)^2, \tag{3.2}$$

where a is the particle diameter. In other words, Re_p takes into account fluid inertia and viscous forces, as well as the extent to which the particle occupies the cross-sectional area of the channel. For low aspect ratio channels, or parallel plates, the channel height H may be used in place of D_h as the characteristic channel dimension.

In applied work, studies have used the effect of inertial lift to focus particles and cells to distinct lateral positions for size-based separations and filtration in straight channels[230]. Some have also used channels with expanding regions following focusing to enhance separation efficiencies[231]. Others have enhanced size-based separations using curved channels to induce secondary Dean flows and increase the lateral separation between particles and cells[15-18,144].

While inertial effects have been exploited, focusing applications often rely on trial-and-error approaches. Recent studies[228,232] have characterized focusing as a three-dimensional, two-step process where particles quickly migrate parallel to the shortest channel dimension, i.e. where the velocity gradient is largest. During this shear lift phase, the particle moves down the velocity gradient. Following this initial step, the particle moves up the velocity gradient, parallel to the long channel dimension. The particle equilibrates in the center face of the channel (or, in some numerical simulation cases, to corners)[228].

This secondary focusing step occurs much slower than the initial step. While the initial focusing steps can be intuited from two-dimensional models[226,233], the migration of particles parallel to the wall is more complicated due to shear and rotational components in three dimensions. In the near-wall region, the velocity gradient in the long dimension is weak.

In addition to the weak gradient, the particle, already at shear-wall equilibrium in the short channel dimension (which we will call the z-direction here), also contains rotational components about the z-axis. As noted by several investigators[226], in the case of small shear forces, the rotational lift about the z-axis can become significant and overcome the shear lift, causing migration up the velocity gradient. The direction of this Magnus-type lift depends on the relative velocity U_{slip}, given by

$$U_{slip} = U_p - U_\infty, \tag{3.3}$$

where U_p is the particle velocity and U_∞ is an undisturbed velocity at the same lateral position in the absence of a particle[226]. Experimental results typically exhibit negative slip velocity, i.e. the particle lags behind the flow, leading to wall-centered equilibrium positions. However, corner equilibrium positions can be explained in cases when the shear force becomes large enough, e.g. an initial position near the corner where the shear becomes large, to overcome the rotation-induced lift.

3.2 Focused Particle Interactions: Ordering

Adding to the already complex nature of the focusing problem, particles in tend to interact, both during focusing and at equilibrium. This is especially true for higher particle concentrations and when the particle size is on the order of the channel dimensions. The focused

particles tend to self-organize, i.e. “order”, into trains with equal longitudinal spacing between each particle (Figures 3.1d and 3.1e)[234].

In particular, the ordering phenomenon has been exploited for cell biology applications. Ordering has allowed for efficient encapsulation of single particles and cells into microdroplets[24,235], which are valuable as bioreactors that confine and accumulated excreted cell products for high-throughput detection of rare biomarkers, drug efficacy, and directed evolution[236]. More recently, studies have encapsulated multiple particles[237] and dissimilar cell pairs[238] for controlled cell-cell interaction experiments in microdroplets. The ability to predict the position of a cell also has particular value in flow cytometry[19,239], where predicting the location of a cell within millisecond time intervals is critical.

3.3 Focusing and Ordering Models

Following the pioneering work of Segre and Silberberg[13,142], initial attempts to analytically model cross-stream migration focused on unbounded rotating cylinders in stationary flow[240] and linear shear flow[225], both at limited to $Re_p << 1$. Later models included bounded Poiseuille flows[241,242] and particle interactions[243], but their perturbation methods were also restricted to small Re_p. Note that despite these limitations, these models were critical first steps in understanding cross-stream migration.

Further studies using sedimentation experiments[244], asymptotic linear shear models[245], and two-dimensional direct numerical simulation[226] provided further insight into the repulsive wall force. Additional three-dimensional simulation studies[246-248] for linear shear and Poiseuille flows have used matched asymptotic expansions, a method which solves the creeping flow equation in an “inner flow” region. Inertial terms are included in an “outer

region", and the two regions are then resolved using a matching parameter. The results of these studies still assume small Re_p, i.e. a/D_h or $a/H << 1$.

Recently, Lattice-Boltzmann simulation methods have provided select solutions to both particle focusing and ordering flows. In two-dimensional planar Poiseuille flow, one study[233] noted that cylinders in flow migrate to equilibrium lateral positions and also form the staggered trains noted in applied ordering studies[19,24,235,237,238]. Additionally, the spacing between the cylinders reached a quasi-steady equilibrium state where small oscillations persisted[233]. Recent three-dimensional simulations[228] of square channels show initial fast migration along the strongest velocity gradient (perpendicular to the nearest wall). A second migration stage is marked by a slow migration parallel to that same wall, with an equilibrium position either in the center of the wall or at the channel corner. This study noted up to eight equilibrium positions (wall centers and corners) and a tendency of particles to form equally spaced trains (but not staggered) similar to those seen in experiments[234] where particle size a is not on the order of the channel dimensions. However, at higher Re_c (~1,000), these trains broke apart and migrated towards the channel center.

An additional computational study compared modeling and experimental results[143]. Using a quasi-dynamic iterative solution algorithm in COMSOL Multiphysics, the study determined equilibrium positions, slip velocities, and rotations for single spherical particles in square channels. The study also calculated total lift as a function of channel position. The results showed shear lift scaled as

$$F_L \propto \rho U_{max}^2 a^3/H. \tag{3.4}$$

This result contradicts one oft-cited analytical study[247] that calculated

$$F_L \propto \rho U_{max}^2 a^4/H^2 \tag{3.5}$$

using point-particle matched asymptotic expansion model. The study used to obtain Equation 3.4 also found that the shear lift dominated the rotational contribution to the total lift.

The a^3 scaling of Equation 3.4 was used to estimate a scaling of the focusing length $L_f/H \propto 1/\mathrm{Re_p}$ by balancing the lift force with Stokes' drag acting parallel to cross-stream migration[20]. While recent studies have provided insight into focusing migration, the computational expense of three-dimensional, two phase particulate flows has still limited the number of available results in the literature. Thus, the precise scaling parameters for particle size, velocity, and geometry have yet to be resolved.

Chapter 4

Single- and Multiple- Cell Controlled Encapsulation

4.1 Abstract

Described in detail in Chapter 2, confinement of cells in picoliter-scale aqueous, monodisperse droplets, provides confinement from a bulk fluid environment with applications in high-throughput screening, cytometry, and mass spectrometry. We describe a method to not only encapsulate single cells, but to repeatedly capture a set number of cells (here we demonstrated one- and two-cell encapsulation) to study both isolation and the interactions between cells in groups of controlled sizes. By combining droplet generation techniques with cell and particle ordering, we demonstrate controlled encapsulation of cell-sized particles for efficient, continuous encapsulation. Using an aqueous particle suspension and immiscible fluorocarbon oil, we generated aqueous droplets in oil with a flow focusing nozzle. The aqueous flow rate was sufficiently high to create ordering of particles that reached the nozzle at integer multiple frequencies of the droplet generation frequency, encapsulating a controlled number of cells in each droplet. This study showed a single-particle encapsulation efficiency $D_{k=1}$ of 79.5% and a double-particle encapsulation efficiency $D_{k=2}$ of 71.5% as compared to their Poisson efficiencies of 36.7% and 26.7%, respectively. The effect of consistent cell and particle concentration was demonstrated to be of major importance for efficient encapsulation.

4.2 Introduction to Cell Encapsulation

Droplet microfluidics provides an instrument for encapsulation of cells in uniformly-sized (monodisperse) aqueous compartments that are suspended in an immiscible oil carrier fluid. Confinement of cells in droplets facilitates the accumulation of cell secretions which otherwise diffuse widely in bulk cell suspensions. This confinement has been exploited for cell surface proteins[207] and cell lysate[208] amplification, high-throughput drug efficacy testing[206], and rare growth event detection[12]. Advanced materials also allow encapsulation of cells in hydrogels and re-suspension in buffer for long-term cell culture[86,90,94] or 3D cell patterning[249]. Co-flowing[51], T-junction[52], and flow-focusing[50] nozzles enable droplet generation at rates which can exceed 10 kHz from a single nozzle. As a result of this high-speed delivery, droplets are well suited for high-throughput screening using techniques such as fluorescence activated cell sorting (FACS)[89] and other microfluidic droplet screening methods[165].

Some applications, however, have been limited by the lack of ability to control the number of cells encapsulated in droplets[21]. Chapter 2 presented a wide range of current and potential uses of droplet microfluidics for cellular investigations. The complexity and challenges of droplet actuation and sensing suggests that we should also optimize the efficiency at which droplet cargo is encapsulated to avoid processing droplets containing the incorrect cargo.

When generating droplets, it logically follows that cells contained in aqueous solution that passes through a droplet generation device will become encapsulated in the resulting droplet. For randomly dispersed cell suspensions such as those used in FACS machines[40], the number of cells in any given droplet is based on Poisson statistics, which govern random encapsulation, where the fraction of droplets containing k cells is given by

$$D_{k,Poisson} = \frac{\lambda^k \exp(-\lambda)}{k!}, \tag{4.1}$$

where λ is the average number of cells per droplet. For Poisson single-cell encapsulation, the probability that a droplet contains one and only one cell is maximized when λ = 1 but is still limited to just 36.8%. The remaining droplets contain either no cells or more than one cell. Therefore, these droplets must be removed or accounted for, sacrificing throughput, wasting reagents and cell samples, and complicating subsequent analysis. In practice, single-cell encapsulation is often achieved using dilute cell suspensions where very few droplets contain multiple cells and most droplets are empty, again sacrificing throughput and reagents. In typical FACS applications, λ is kept at around 0.3 to avoid droplets containing multiple cells. Using λ = 0.3 and k = 1 in Equation 4.1, the single-cell encapsulation efficiency $D_{k=1,\ Poisson}$ (where efficiency is defined as the percentage of droplets containing the "correct" number of cells) is limited to around 22%[22,23].

Note that we can also define an efficiency related to the fraction of *cells* which end up in the "correctly" encapsulated drops is calculated using

$$P_k = \frac{kD_k}{\sum_{k'}(k' \times D_{k'})}. \tag{4.2}$$

The subtle difference between the two metrics is that D_k relates to the utilization of aqueous fluid and the amount of drop sorting that must be completed following encapsulation, and P_k relates to the utilization of the cell sample. As an example, one could use a dilute cell suspension (low λ) to encapsulate drops where most drops containing cells would contain just one cell. While the efficiency metric P_k would be high, the majority of drops would be empty (low D_k), thus requiring a sorting mechanism to remove empty drops, also reducing throughput.

In one study, self-sorting of cell-containing droplets from empty droplets provided singly-encapsulated cells at a throughput of 160 cells/s following a 1 kHz droplet generation

rate[250]. Here, the empty droplets were passively sorted[250] by size. Alternatively, empty droplets could be interrogated as if they contained cells, and their data can be considered later. To overcome the Poisson statistical limitation, another study utilized densely packed gel particles in aqueous flows upstream of the flow focusing droplet nozzle to encapsulate single gel particles at 1.5 kHz rates with 98% efficiency[251]. However, expansion of the method to cells would require prior cell encapsulation of cells into gel particles, a step also hindered by Poisson encapsulation, to alleviate fluid stresses associated with flow-based close packing.

Combining droplet generation with inertial focusing and ordering provides the ability to encapsulate drops with more predictable numbers of cells per droplet and higher throughputs than random encapsulation. Inertial focusing, first discovered by Segre and Silberberg[13], refers to the tendency of finite-sized particles and cells to migrate to lateral equilibrium positions in channel flow. Ordering refers to the tendency of the particles (and cells) to passively organize into equally spaced, staggered, constant velocity trains. When particle trains form upstream of a droplet generation nozzle, they arrive at the nozzle at equal time intervals. By tuning the aqueous cell suspension and immiscible oil flow rates, droplets are generated at the same frequency that cells arrive at the nozzle, thereby controlling the number of cells in each droplet.

Both focusing and ordering require sufficiently high flow rates and particle sizes, i.e. high Particle Reynolds number Re_p (= $Re_c(a/D_h)^2$)[20,143]. Empirically, the length required to achieve focused and ordered trains decreases as Re_p increases. Note that the Re_p requirements (for this study on the order 0.5, respectively) may conflict with the need to keep aqueous flow rates low to avoid inertial jetting at the drop generation nozzle. Additionally, higher flow rates lead to higher shear stresses on cells, which are not addressed in this protocol. The previous ordered encapsulation study demonstrated that over 90% of singly encapsulated HL60 cells

under similar flow conditions to those in this study maintained cell membrane integrity[24]. However, the effect of the magnitude and time scales (on the order of fractions of seconds) of shear stresses will need to be carefully considered when extrapolating to different cell types and flow parameters.

Because very few studies address interparticle train spacing[252,253], here the determining the spacing is done empirically and will depend on channel geometry, flow rate, particle size, and particle concentration. Nonetheless, the equal lateral spacing between trains implies that cells arrive at predictable, consistent time intervals. When droplet generation occurs at the same rate at which ordered cells arrive at the nozzle, the cells become encapsulated within the drop in a controlled manner. This technique has been utilized to encapsulate single cells with throughputs on the order of 15 kHz[24], a significant improvement over previous studies reporting encapsulation rates on the order of 60-160 Hz[36,250] and on the same order of magnitude as current FACS machines[40]. In the previous controlled encapsulation work, over 80% of droplets contained one and only one particle (used as a cell surrogate), a significant efficiency improvement over Poisson (random) statistics, which predicts less than 38% efficiency on average[24].

In previous controlled encapsulation work[24], the average number of particles per droplet λ was tuned to provide single-cell encapsulation. We hypothesize that through tuning of flow rates, we can efficiently encapsulate any number of cells per droplet when λ is equal or close to the number of desired cells (k in Equation 4.1) per droplet. While single-cell encapsulation is valuable in determining individual cell responses from stimuli, multiple-cell encapsulation provides information relating to the interaction of controlled numbers and of cells. Here we present a device, protocol, representative results using polystyrene microspheres, and

discussion for controlled encapsulation of multiple cells using a passive inertial ordering channel and flow-focusing nozzle.

4.3 Materials and Methods

4.3.1 Fabrication and Materials

Devices (Figure 4.1) were constructed using standard soft lithography procedures.[4] Briefly, master molds were fabricated using SU-8 photoresist (Microchem 2050, Newton, MA) patterned by ultraviolet exposure through a 50,000 dpi patterned Mylar mask (FineLine Imaging, Colorado Springs, CO). The ordering channel measured 27 μm wide by 52 μm tall. Polydimethyl siloxane (PDMS) elastomer (Dow Corning Sylgard 184, Midland, MI) was mixed at a 10:1 w/w base to curing agent ratio, poured onto the master mold, de-gassed, and cured overnight at 65º C. The PDMS devices were then bonded to 3 inch x 1 inch glass microscope slides using a hand-held corona surface treater (Electro-Technic Products BD-20AC, Chicago, IL).[254] Devices were baked at 120º C overnight to return the channel walls to a hydrophobic state.[133] To further ensure hydrophobicity, the devices were also injected with Aquapel™ and then purged with air to coat interior channel surfaces[24].

4.3.2 Experimental Setup

Fluorocarbon oil (3M FC-40, Saint Paul, MN) stabilized by a 2.5% w/w PFPE-PEG block copolymer surfactant (RainDance Technologies, Lexington, MA)[67] served as the oil carrier fluid for aqueous droplets. Aqueous and oil fluids flow rates were controlled using positive displacement syringe pumps (Chemyx Nexus 3000, Stafford, TX). To demonstrate co-encapsulation, 10 μm polystyrene microspheres (Thermo G1000, Waltham, MA) served as cell

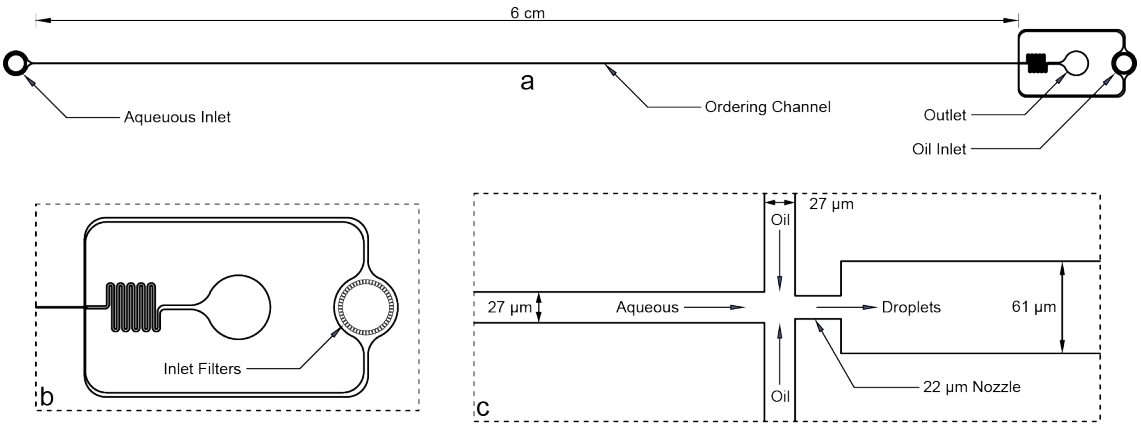

Figure 4.1. Encapsulation device schematic. (a) Overall device with inlets, outlet, and long ordering channel. The device height was 52 µm and the ordering channel width was 27 µm. (b) Both aqueous and oil inlets had large debris filters with gaps on the order of the ordering channel width for the enlarged view of the oil inlet. (c) The enlarged nozzle view shows equal channel widths of 27 µm for the aqueous and oil channels, followed by the nozzle contraction of 22 µm and sudden expansion to a wider 61 µm channel. Note that the dimensions of the device shown here were verified using a profilometer after microfabrication and differed slightly from the nominal dimensions on the mask.

surrogates for initial experiments. Prior to experiments, stock particle concentrations were increased to approximately 25 x 10^6 particles/mL using centrifugation and supernatant removal. Rather than using density-matched solutions, we exploited the density mismatch between the aqueous fluid and particles (specific gravity = 1.05 for polystyrene microspheres) to control real-time particle concentration via sedimentation within the syringes[237].

4.3.3 Imaging

Imaging was performed using brightfield illumination on an inverted microscope (Zeiss Axio Observer, Oberkochen, GER) and a high-speed camera (Vision Phantom V310, Wayne, NJ). Droplet encapsulation videos were acquired at 21,005 frames per second. Particle encapsulation data was obtained by visually observing the encapsulated particles upon entry into each droplet.

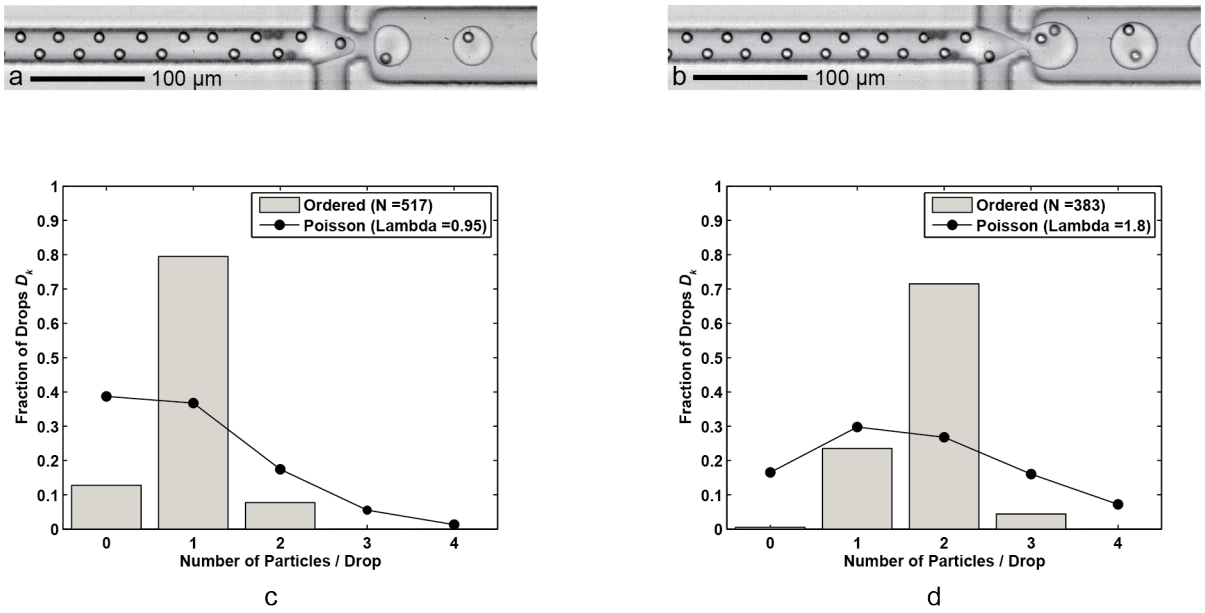

Figure 4.2. Single- and double- particle encapsulation statistics. (a) Droplet formation with one cell per drop (Q_{oil} = 60 µL/min, Q_{aq} = 9 µL/min) with a droplet generation rate of 6.1 kHz, average droplet size of 24.4 pL, and a single-cell capture efficiencies D_k = 79.5% and P_k = 83.7% (λ = 0.95) for a sample size of n_d = 517 droplets and n_p = 491 particles. (b) Droplet formation with two cells per droplet was achieved simply by reducing the FC-40 flow rate Q_{oil} to 30 µL/min. The larger (39.8 pL) drops were formed at a rate of 3.8 kHz with a two-cell capture efficiency D_k = 71.5% and P_k = 79.5% (λ = 1.80) for a sample size of n_d = 383 droplets and n_p = 689 particles. (c and d) Two histograms compare the drop encapsulation particle efficiencies D_k of ordered single- and double- particle encapsulation with Poisson statistics (random encapsulation). Note that for both cases, particle spacing in the direction of flow was about 17-18 µm for fully ordered, alternating particles.

4.4 Results and Discussion

Results are presented which achieved both controlled single-particle and controlled double-particle encapsulation (Figure 4.2). By decreasing the FC-40 oil flow rate, single-particle encapsulation became two-particle encapsulation. Conversely, we could have increased the aqueous flow rate to deliver particles to the nozzle more quickly, but we also would have increased the risk of inertial jetting of the aqueous stream. Histograms in Figure 4.2 present the fractional number of particles per droplet for the two cases, along with comparisons to Poisson statistics. Both the single and double particle encapsulation efficiencies outperformed random encapsulation efficiencies by over a factor of two and greatly reduced the number of droplets with more than the desired number of particles.

4.4.1 Particle and Cell Concentration

Figure 4.3 demonstrates the need for proper concentrations for high efficiency; that is, λ, a function of both particle concentration and droplet volume, should be equal or close to the number of desired cells per droplet to maximize correctly-encapsulated particles or cells. The occasional empty droplets are primarily due to "missing" particles in the ordered trains, while the cases where there are more encapsulated particles than desired result from local high particle concentrations and particles which sometimes migrate toward one of the two vertical focusing positions.

Note that a higher concentration of particles or cells is usually a good thing for full ordering as dense trains tend to spread out over time and fill emptier regions between trains. On the other hand, if concentration is too high, the high number of particles may cause interfacial instabilities that induce jetting at the nozzle. In specific studies (such as single-cell encapsulation, for example), it may be more advantageous to avoid multiple-cell droplets at the expense of introducing a few more empty droplets, so a slightly lower λ will be desired. This would also apply for studies aimed at interactions between two cells or between a cell and a particle, where single-particle or single-cell droplets are more tolerable than droplets with two or more of one kind of cell or particle.

Maintaining a constant λ over time is critical for consistent encapsulation. Buoyancy matching assists in long-term concentration control by reducing settling of cells and particles in the syringe and tubing. However, buoyancy matching also results in a higher aqueous viscosity that may delay ordering (lower Re_p resulting in longer focusing channel requirements), increases the channel pressure droplet, and change the flow rates required for droplet generation. Here, we used 9.9 μm diameter microspheres with a particle volume fraction of (approximately 25 million

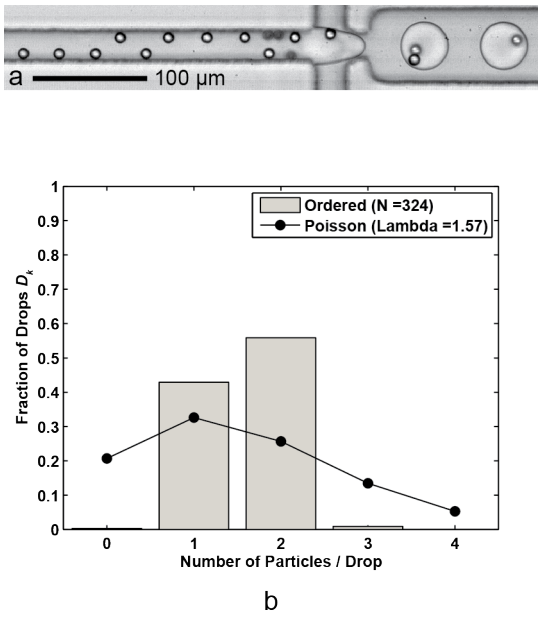

Figure 4.3. Effect of particle concentration on encapsulation efficiency. (a) As the concentration decreased, full ordering did not occur, and thus "holes" in the trains emerged, leaving some droplets with fewer than anticipated particles. (b) The histogram shows the decreased efficiency (D_k = 55.9%, P_k = 70.9%) for two-particle encapsulation due to a lower value of λ = 1.57 where there are nearly as many single-particle droplets as there were double-particle droplets. This figure results from Q_{oil} = 30 µL/min and Q_{aq} = 9 µL/min, the same flow conditions as for Figure 4.2b.

particles per mL), but we utilized tilting to increase volume fractions to 34 million particles per mL for the data shown in Figure 4.2. A second alternative is to mix the aqueous fluid intermittently with an enclosed stainless steel ball bearing (Teflon coated for working with cells) using a small external magnet. Care is required however to avoid letting the ball bearing settle to the syringe tip where it may occlude the entrance to the inlet tubing. However, these alternatives are more labor intensive and less repeatable than buoyancy matching, so buoyancy matching is most suitable for larger scale experiments occurring over long time frames.

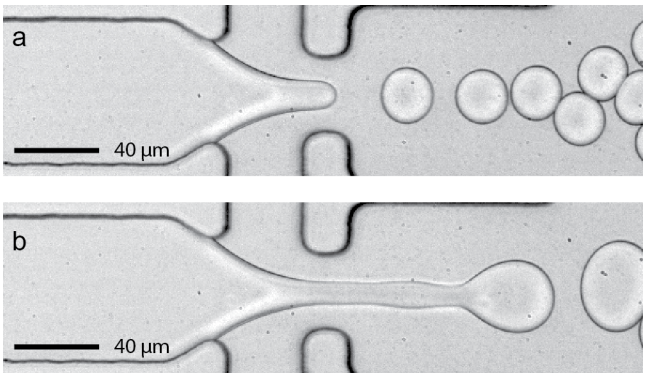

Figure 4.4. Hysteresis of the dripping to jetting transition. The low aspect ratio device dimensions were 80 µm wide x 22 µm high. (a) At constant FC-40 flow rate (Q_{oil} = 45 µL/min), droplet formation occurred at 10 kHz using Q_{aq} = 8 µL/min. As the aqueous flow rate was slowly increased to 10 µL/min, jetting of the aqueous fluid stream was triggered. (b) When the flow rate was returned to 8 µL/min jetting continues. Note that steady droplet formation could be re-established by briefly pausing the aqueous flow pump (a 1 second pause was typical).

4.4.2 Limitations due to Jetting

While inertial ordering requires high Re and Re_p to operate, when the aqueous and oil flows are pushed higher and higher, steady dripping of droplets turns to inertial (high Weber number We) jetting[51] (see Figure 4.4), and uncontrolled encapsulation results. For cells smaller than the 10 µm particles used here, smaller channel dimensions may be required to achieve sufficient Re_p if the flow rates cannot be increased without jetting. One peculiarity of jetting in microfluidic systems is that hysteresis effects can occur which make it difficult to stop jetting by simply lowering the aqueous flow rate once it occurs back to a point where it was not observed. Based on experimental results, one could develop a dimensional or non-dimensional dripping to jetting flow map like those previously developed for axial co-flowing nozzles[51] and T-junctions[61,255,256] with additional contours for droplet generation rate, cells per droplet, and encapsulation efficiency. This map would provide a robust roadmap from which the droplet generation rate can be predicted to calculate λ and thus provide an estimated flow rate for water and oil streams *a priori*.

It is important to note that droplet generation and the dripping to jetting transition are very sensitive to surfactant concentration. High surfactant concentrations increase the viscosity of the oil, changing the droplet generation parameters (See Chapter 2). As an aside, the scarcity of widely available biocompatible surfactants for fluorocarbon oils presents a major challenge. Currently, one commercial supplier (RainDance Technologies) exists for PFPE-PEG block copolymer surfactants[67], but studies demonstrate small-scale synthesis techniques of a number of surfactant groups such as PFPE-HEG[68,69]. Alternatives such as light mineral oil have been utilized in biological droplet generation applications to access a wider range of available surfactants[115,133], but note that the accompanying increase in viscosity as compared to fluorocarbon oil alters the droplet generation parameters. A recent review[66] describes a large number of published continuous phase oils and surfactants.

4.4.3 Extending to Additional Particles and Cells

While not directly demonstrated here, additional reductions in oil flow rate Q_{oil} from those presented in Figure 4.2b would further increase the number of particles per droplet to three, four, and so on. To achieve more particles per droplet, either Q_{oil} must decrease or the aqueous flow rate Q_{aq} must increase. As an aside, we have included a supplemental MATLAB script which models the encapsulation efficiency of capturing any number of particles in droplets. The user inputs the average particle spacing and particle spacing standard deviation, which models the degree of ordering. For ordered trains, the standard deviation will be small. Additionally, the user inputs the average droplet size and droplet size standard deviation, which accounts for the polydispersity of droplet sizes. Refer to the script documentation for additional information.

When increasing the aqueous flow rate or decreasing the oil flow rate to increase the number of particles or cells per droplet, the risk of unstable jetting increases as the respective flow rates near extreme values. Thus, the maximum number of achievable particles/cells per droplet will depend on device geometry and fluid properties. Given the particle/cell concentration and oil flow rate, the number of particles/cells per droplet is constrained by upper limits on aqueous flow rates, which must be large enough to induce ordering but must be small enough to avoid unstable jetting (and limit shear stresses on cells to ensure viability).

4.5 Conclusions

We have described a method to not both single cells and two cells using particles to demonstrate the device. By combining droplet microfluidics and inertial microfluidics, we have encapsulated cell-sized particles for efficient, continuous encapsulation. Using an aqueous particle suspension and immiscible fluorocarbon oil, we generated aqueous droplets in oil using a flow-focusing nozzle. The particle Reynolds number Re_p was sufficiently high to create ordering of particles that reached the nozzle at integer multiple frequencies of the droplet generation frequency, encapsulating a controlled number of cells in each droplet. This work achieved a single-particle encapsulation efficiency $D_{k=1}$ of 79.5% and a double-particle encapsulation efficiency $D_{k=2}$ of 71.5% as compared to their Poisson efficiencies of 36.7% and 26.7%, respectively. The effect of consistent cell and particle concentration was demonstrated to be of major importance for efficient encapsulation.

Chapter 5

High-throughput Controlled co-encapsulation for Studying Cellular Interactions and Sexual Reproduction in Droplets

5.1 Abstract

As noted in previous chapters, controlling the number of cells per droplet has been limited to using *Poisson* (random) encapsulation for high-throughput applications. While the *Poisson* probability of a droplet containing one and only one cell is limited to 36.8%, the *Poisson* probability of pairing two distinct cell types in a droplet is even more limited at 13.5%. Combining droplet microfluidics with inertial microfluidics, we present a device which efficiently co-encapsulates cell pairs in droplets at rates on the order of 6 kHz. We demonstrate particle co-encapsulation where 64% of droplets contained the correct one-to-one pairing, representing a nearly fivefold improvement to *Poisson* co-encapsulation. We also apply the device to encapsulate two separate strains of *Chlamydomonas reinhardtii*. *C. reinhardtii* is a single-cell microalgae with applications as a model organism, recombinant protein source, and potential source of multiple biofuels. After inducing gametogenesis by nitrogen starvation and thermally inducing flagella loss, we co-encapsulate separate mating-type plus (mt+) and mating-type minus (mt-) *C. reinhardtii* cells in droplets. Here, 29% of droplets contained one and only one cell of each mating type, over a twofold improvement to the *Poisson* co-encapsulation probability of 13%. Approximately one hour following deflagellation, gametes regained flagellar motility and mating ability within the droplets. The mated zygotes were stored in emulsion form without nutrient replenishment. After 17 days, both zygospores and, remarkably, some unmated

gametes remained viable. When the emulsion was broken and plated on full-nutrient agar, zygospore germination, tetrad hatching, and then mitosis followed. In addition to algae, the device has the potential for confined interaction studies for a variety of cell types.

5.2 Introduction to Controlled Co-encapsulation

Droplet microfluidics provides a platform technology for encapsulation of cells in uniformly-sized (monodisperse) aqueous compartments that are suspended in an immiscible oil carrier fluid. Confinement of cells in droplets facilitates the accumulation of cell secretions which otherwise diffuse widely in bulk cell suspensions. Single-cell encapsulation in droplets has been exploited for amplification of cell surface proteins[207,236] and cell lysates[208], testing of high-throughput drug efficacy[206], and detecting growth events[12,257,258], where high cell density quorum-sensing is quickly achieved by confinement. Advanced materials also allow for cell encapsulation in hydrogel precursor droplets which are then cured and re-suspended into buffer for long-term cell culture[86,90,94] or 3D cell patterning[249].

Co-flowing[51], T-junction[52], and flow-focusing[50] nozzles enable droplet generation at rates which can exceed 10 kHz from a single nozzle. For the flow-focusing nozzle design used here, the oil phase flow pulls an immiscible aqueous flow fluid into a thinning “neck” region. When oil shear stresses, maximized at the nozzle constriction, overcome interfacial tension forces, a droplet breaks from the main aqueous flow (see results in Figures 5.4 and 5.6)[44]. The process repeats at kHz rates, and the droplet breaks from the main flow at the same neck position each time, thus leading to a near-uniform droplet size. As a result of their high-speed production, droplets are well suited for high-throughput screening using techniques such as fluorescence activated cell sorting (FACS)[89] and other microfluidic droplet screening methods[165,259].

However, protocols and applications using cell-laden droplets often suffer from the inability to control the number of cells in a droplet[21]. In randomly dispersed aqueous cell suspensions, cells are encapsulated according to *Poisson* statistics. The probability that a droplet contains k cells is therefore given by

$$D_{k,Poisson} = \frac{\lambda^k \exp(-\lambda)}{k!}, \tag{5.1}$$

where λ is the average number of cells per droplet. For random single-cell encapsulation, the probability that a droplet contains one and only one cell is maximized when $\lambda = 1$ but is still limited to just 36.8%. The remaining droplets contain either no cells or more than one cell. The unwanted droplets must be removed or accounted for, sacrificing throughput, wasting reagents and cell samples, and complicating subsequent analysis. In practice, single-cell encapsulation is often approached using dilute cell suspensions. In typical FACS applications, λ is diluted to around 0.3 to avoid droplets containing multiple cells. Using $\lambda = 0.3$ and $k = 1$ in Equation 5.1, the single-cell encapsulation efficiency $D_{k=1,\ Poisson}$ (where efficiency is defined as the percentage of droplets containing the "correct" number of cells) is limited to around 22%[22,23]. While very few droplets (3%) will contain multiple cells, most droplets (74%) will be empty, again sacrificing throughput and reagents.

However, both manual[126] and passive[24,237,250] methods have been devised to provide more control of number of cells in a droplet. To reduce the number of droplets containing the "incorrect" number of cells, high efficiency encapsulation at kHz rates has been achieved using a combination of droplet microfluidics and inertial microfluidics[24,237]. Inertial microfluidics defies the notion that small microfluidic channels preclude inertial effects on finite-sized particles and cells in flow. At sufficiently high mean flow velocity and cell diameter a, cells migrate (due to inertial lift forces) across streamlines to lateral equilibrium positions and

form self-ordered trains of equal longitudinal spacing. The flow velocity and cell diameter are non-dimensionalized by the Particle Reynolds number Re_p ($= Re_c(a/D_h)^2$), where the channel Reynolds number $Re_c = \rho U_{max} D_h/\mu$, and U_{max}, D_h, ρ, and μ represent the maximum fluid velocity (assuming no particles), channel hydraulic diameter, fluid density, and fluid dynamic viscosity, respectively. Higher Re_p values increase the quality of focusing and ordering and decrease the required channel length, which scales as $1/Re_p$[20].

To achieve controlled encapsulation, ordering channels are placed upstream of a droplet-generating nozzle. The droplet generation frequency is tuned to match the frequency at which the self-ordered cells arrive at the nozzle by adjusting the aqueous and oil flow rates. In straight ordering channels, single-cell encapsulation efficiency $D_{k=1}$ (the fraction of droplets containing one and only cell or particle) has been demonstrated at 80% for 10 μm particles[24,237] and 60% for human HL60 cells with 90% cell viability[24]. Another study[235] achieved ordered encapsulation using curved channels, which induced secondary Dean flows that pushed cells to one side of the ordering channel. That study achieved 80% encapsulation efficiency of HL60 cells, 92% of which maintained their membrane integrity. Recently, ordered co-encapsulation of two and only two microparticles per droplet was demonstrated using a straight ordering channel[237]. In that study, decreasing the oil flow (continuous phase) rate reduced the droplet generation frequency, independent of ordering, such that approximately two particles arrived at the nozzle for each droplet formed (λ = 1.8). As a result, 71.5% of droplets contained two and only two particles as opposed to a predicted $D_{k=2,\ Poisson}$ = 26.7% using Equation 5.1.

Ordered co-encapsulation in previous work was limited to single particle types from the same ordering channel[237]. While interactions between like cells are of interest, the ability control the co-encapsulation of multiple cell types (without the need to induce pairwise

fusion[45,122] of droplets containing one cell of each type) would significantly broaden the utility of co-encapsulation. Previous cell-cell interaction studies have employed continuous flow microfluidic devices to study co-cultured cell migrations when tumor cells were paired with endothelial[260] and immune cells[261]. More recently, co-culture of distinct cell lines has been performed within droplets[262,263]. One study[262] used *Poisson* co-encapsulation of separate blood progenitor cell lines in agarose gel microspheres and re-suspended them in buffer to demonstrate sub-population responsiveness to interleukin-3 (IL-3). This study varied the average ratio of human MBA2 cells (secrete IL-3) to M07e cells (require IL-3) and used FACS to assess cell viability over several days. The study was limited to droplet generation rates on the order of 40 Hz, and controlled only the average cell ratios in the droplet samples, not the number of cells in each particular droplet.

To illustrate the need for controlled co-encapsulation, consider the encapsulation of a random mixture of two cell types (A and B) using *Poisson* statistics. The probability D_{k_A} of a droplet containing k_A cells of Type A at concentration λ_A (cells per droplet) is again given by Equation 5.1. Independently, the probability D_{k_B} of a droplet containing k_B cells of Type B at an independent concentration λ_B also follows Equation 5.1. The *Poisson* probability for co-encapsulation where a droplet contains k_A cells of Type A and k_B cells of Type B is then given by the product of the two independent probabilities as

$$D(k_A \cap k_B, Poisson) = \frac{{\lambda_A}^{k_A} \exp(-\lambda_A)}{k_A!} \times \frac{{\lambda_B}^{k_B} \exp(-\lambda_B)}{k_B!}. \quad (5.2)$$

For perfect one-to-one co-encapsulation of two distinct cell types ($k_A = k_B = 1$), the *Poisson* probability is maximized when $\lambda_A = 1$ and $\lambda_B = 1$. Thus, the maximum probability of one-to-one co-encapsulation from a randomly distributed cell suspension is $D_{k_A=k_B=1,Poisson} = 13.5\%$. For parameters used in typical FACS applications (λ_A and $\lambda_B \sim 0.3$), the *Poisson* probability of

obtaining one-to-one co-encapsulation is just 5%. Additionally, 35% of droplets would be empty, 33% would contain just one cell, and 7% would contain more than two cells. For optimal co-encapsulation, one could independently control the number and type of each cell in a droplet while maintaining high throughput.

Note that pairwise fusion of single-cell containing droplets is also possible for creating encapsulated cell pairs. However, serial methods such as electro-coalescence[122] and optical coalescence[124] require external interfaces that increase device complexity. Some passive methods such as using channel surface wettability modification[264] can also induce coalescence. Importantly, all droplet-merging methods require slowing or even stopping of flow to induce droplet contact and coalescence[46], thereby reducing throughput.

Here, we present a passive co-encapsulation device which combines two ordered cell trains to exceed the *Poisson* limit. Specifically, two 44 μm wide by 31 μm tall ordering channels, aligned in parallel, convey separate aqueous cell suspensions at sufficiently high Re_p to induce ordered trains of equal longitudinal spacing (Figure 5.1a). We report results which show significant improvements in co-encapsulation efficiency $D_{k_A=k_B=1}$ for both polystyrene microspheres and unicellular algae. *C. reinhardtii* provides a particularly relevant cell type due to its wide use as a model organism in biology[265], emergence as a source for recombinant proteins[266], and multiple end uses in the biofuel industry (ethanol[267], hydrogen[268], and biodiesel[269])[270]. Most notably, its life cycle is well suited to droplets; algae undergo sexual

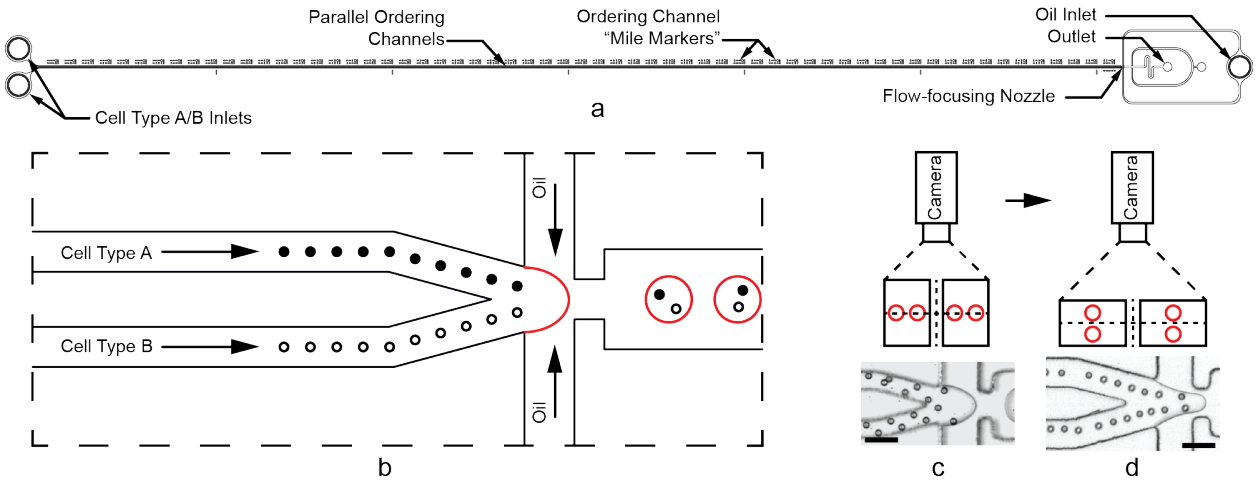

Figure 5.1. Cell and particle co-encapsulation device. (a) Parallel ordering channels are 6 cm long. (b) Close-up schematic of the flow-focusing nozzle. Cells hydrodynamically order with equal longitudinal spacing in one of two upstream channels. Immiscible oil pulls droplets from the aqueous cell streams such that one cell of each type arrives at the nozzle at the same frequency as droplet formation, thus encapsulating a pair in a single droplet. (c,d) For the high aspect ratio ($W < H$) arrangement shown in (c), the particles on the inside walls accelerate downstream faster than those on the outside walls, disrupting encapsulation of pairs. Low aspect ratio ($W > H$) channels shown in (d) provide quadrilateral symmetry so that all particles and cells experience the same velocity profiles, leading to more optimal pairing. The particles in (d) appear to form one collinear train, but closer inspection reveals staggered ordering on the top and bottom surfaces of the channel. Scale bars in (c) and (d) represent 50 μm.

reproduction by meiosis. Using separate mating type plus (mt+) mating type minus (mt-) strains, we induced gametogenesis and co-encapsulated gamete pairs in droplets. Following ordered co-encapsulation, we show that cells retained their mating ability. Somewhat remarkably, zygospores and unmated gametes were viable for 17 days in droplets without culture media replenishment. We broke the emulsion on agar to induce zygospore hatching and allow the algae offspring to resume asexual (vegetative) reproduction. The ability to efficiently encapsulate cell pairs, exploit paired cell interactions, and achieve long-term cell survival highlight a remarkable droplet microfluidic tool that may be applied to high-throughput screening and a wide range of cell interaction assays.

5.3 Materials and Methods

5.3.1 Device Design

Two parallel ordering channels, width W = 44 μm and height H = 31 μm, merge immediately before a flow-focusing nozzle as shown in Figures 5.1a and 5.1b. For calculating Re_c, we used known finite difference solutions[271] for rectangular channel flow to obtain U_{max}/U_{mean} = 2.068 for the aspect ratio α (=W/H) = 0.70. The aqueous channel outlet is 75 μm wide, and the nozzle constriction is 44 μm wide. Importantly, the low aspect ratio ($W > H$) design, flipped from previous work (where $W < H$)[24,237], avoids unequal acceleration of cells when two high aspect ratio channels merge. To illustrate this motivation, consider the high aspect ratio case shown in Figure 5.1c using polystyrene microspheres. When the channels merge, the particles on the inside channel walls experience a velocity mismatch with those on the outer channel walls. The mismatch disrupts the longitudinal spacing between particles and causes inefficient co-encapsulation. In the low aspect ratio case (Figure 5.1d), the particles are ordered on the channel centerline (when viewed from the top) and experience a quadrilateral symmetry when two streams merge. Since all particles experience the same velocity profile at the merge, more consistent spacing is maintained.

It is important to note that the ordering shown in Figure 5.1c and 5.1d only appears different due to the camera angle and three-dimensional effects. Because cells tend to order along the short channel dimensions with the strongest velocity gradients, cells appear staggered when viewed from the top of the high aspect ratio channel. The camera schematics in Figures 5.1c and 5.1d show that when the particles order in staggered trains (on the top and bottom of the low-aspect ratio channel), the ordering only appears different due to the two-dimensional camera

view. Additional design considerations regarding ordering and the dripping to jetting transitions are addressed in the Results and Discussion section.

5.3.2 Fabrication and Materials

Devices were constructed using standard soft lithography procedures[4]. Briefly, master molds were fabricated using SU-8 photoresist (Microchem 2050, Newton, MA) patterned by ultraviolet exposure through a 50,000 dpi patterned mylar mask (FineLine Imaging, Colorado Springs, CO). Polydimethyl siloxane (PDMS) elastomer (Dow Corning Sylgard 184, Midland, MI) was mixed at a 10:1 w/w base to curing agent ratio, poured onto the master mold, de-gassed, and cured overnight at 65º C. The PDMS devices were then bonded to 3" x 1" glass microscope slides using a hand-held corona surface treater (Electro-Technic Products BD-20AC, Chicago, IL)[254]. Devices were baked at 120º C overnight to return the channel walls to a hydrophobic state[133]. To further ensure hydrophobicity, the devices were also injected with Aquapel™ and then purged with air to coat interior channel surfaces[24].

5.3.3 Experimental Setup

Fluorocarbon oil (3M FC-40, Saint Paul, MN), stabilized by a 2.5% w/w PFPE-PEG block copolymer surfactant (RainDance Technologies, Lexington, MA)[67], served as the oil carrier fluid for aqueous droplets. Aqueous and oil flow rates were independently controlled using three separate positive displacement syringe pumps (Chemyx Nexus 3000, Stafford, TX). To demonstrate co-encapsulation, 10 μm, monodisperse (coefficient of variation <5%) polystyrene microspheres (Thermo G1000, Waltham, MA) served as cell surrogates for initial experiments. Rather than using density-matched solutions, we exploited the density mismatch

between the aqueous fluid and particles (specific gravity = 1.05 for polystyrene microspheres) to control particle concentration via sedimentation within the syringes[237]. For both particle and cell co-encapsulation results, the aqueous flow rate was 10 μL/min in each ordering channel, and the total oil flow rate was 45 μL/min.

5.3.4 Algal Cultures

Microalgae *C. reinhardtii* (mt-) CC-124 and (mt+) CC-125 strains (Chlamydomonas Resource Center, Saint Paul, MN) were prepared separately in *Sueoka's* High Salt Media (HSM)[272] using an orbital shaker plate (SCILOGEX SK-180-Pro, Berlin, CT) at 160 RPM. Culture temperature and gas composition were maintained at ambient conditions. Cell cycle synchronization was achieved by cycling between 12 hour light and 12 hour dark periods[265]. Following centrifugation at 100 g for 20 minutes and aspiration of supernatant, samples were re-suspended in a nitrogen-free variety of Sueoka's High Salt Media and exposed to continuous light for 24 hours to induce gametogenesis[265,273]. Immediately prior to experiments, cells were concentrated by centrifugation to working concentrations of approximately 30 x 10^6 cells/mL, as measured by counting cells within a hemocytometer. Again, we controlled cell concentrations in real time using sedimentation (*C. reinhardtii* specific gravity ~ 1.04[274]) within the syringes.

5.3.5 Reversible Algae Deflagellation

For initial vegetative algae cell ordering experiments in single channels, cells tended to bounce away from the channel walls and off their hydrodynamic focusing and ordering positions (see Figure 5.2a) due to the presence of flagella. However, *C. reinhardtii* cells are known to

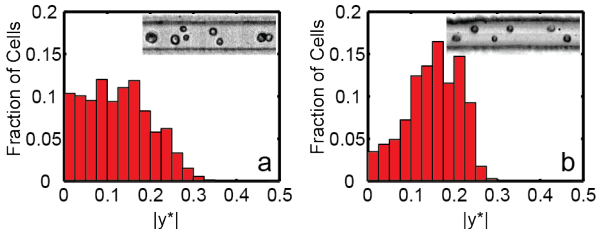

Figure 5.2. Ordering of algae cells with and without flagella. Histograms present normalized counts of vegetative *C. reinhardtii* cells as a function of non-dimensional cross-stream channel position $|y^*|$. (a) Normalized histogram for cells with flagella (N=164). (b) Normalized histogram for deflagellated cells (N=113). In both histograms, $|y^*| = 0$ represents the channel centerline, and $|y^*| = 0.5$ represents the channel wall for a 27 μm wide by 52 μm tall single channel. Measurements were taken at the end of the 6 cm-long channel. For (b), cells were deflagellated by submerging a 1.5 mL centrifuge tube sample in a 40° C water bath for 30 minutes. Both the histogram and still images show improvements in focusing and ordering for the deflagellated cells.

excise or resorb their flagella, i.e. "deflagellate", in response to various environmental stresses such as low pH[275,276] or elevated temperature[277]. Deflagellated cells can then quickly regrow the flagella when more favorable conditions return provided the stress was not too damaging. For example, *C. reinhardtii* gametes deflagellated using pH shock have been shown to regain both flagellar motility and mating capability[275]. After 25 minutes removed from the pH shock, the cells regained motility. Between 45 minutes and two hours following deflagellation, the gametes were able to mate[275].

To demonstrate the importance of flagella removal on ordering, Figure 5.2 shows histograms of cross-sectional focusing position for vegetative UTEX-90 (UTEX, Austin, TX) *C. reinhardtii* cells with flagella (Figure 5.2a) compared to cells without flagella (Figure 5.2b). Measurements of cross-sectional position were taken 6 cm from the inlet of a 27 μm wide and 52 μm high ordering channel[24]. For the results shown in Figure 5.2 and for co-encapsulation experiments, algae were moved to 1.5 mL centrifuge tubes and heated in a constant temperature bath (40º C) for 30 minutes to induce reversible loss of flagella immediately prior to co-encapsulation experiments.

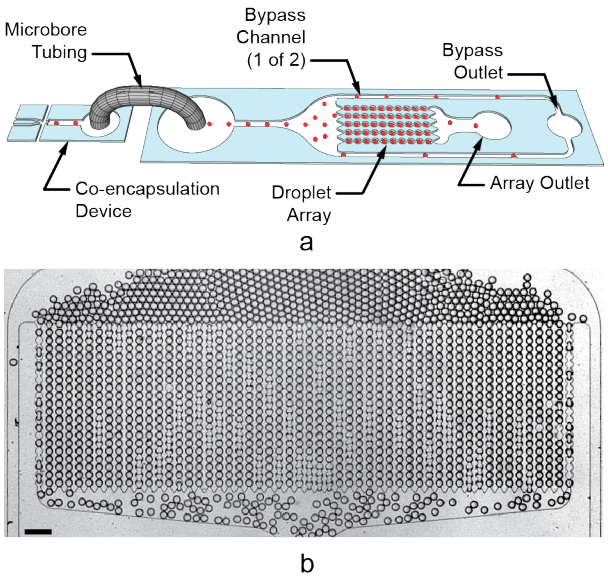

Figure 5.3. Interface between co-encapsulation and droplet trap devices. (a) Three-dimensional schematic illustrating the coupling between the co-encapsulation device (left) and customized *Dropspot*[134] array (right). Droplets (represented by the red spheres) generated in the co-encapsulation device are conveyed via tubing to the inlet of a droplet array device. Droplets either flow through the array (to an array outlet tube) or a bypass channel (to a bypass outlet tube). When the array contains the desired numbers of droplets, the array outlet tube is reversibly clamped, immobilizing the droplets in the transparent device. Additional generated droplets may continue to be generated and exit through the bypass outlet, or the flows may be stopped. (b) Still image showing empty droplets filling the 55 µm tall array device used in this study. The array contained 54 columns and 20 rows for a total of 1080 array traps. The trap diameter measured 61 µm with a minimum constriction width of 35 µm between traps in the same column. The scale bar represents 200 µm.

5.3.6 Droplet Visualization

Following co-encapsulation, droplet samples were coupled directly into a customized *Dropspot*[134] array device, shown in Figure 5.3. This array allowed for long-term tracking of flagellar mt+ and mt- agglutination (mating) and zygote formation within specific droplets, which were identified by their array coordinates. Arrays were secured to a petri dish and immersed in a layer of DI water to prevent slow droplet evaporation through the PDMS. A larger emulsion sample was also stored in the dark at room temperature for zygospore maturation. Seventeen days post-encapsulation, 50 µL of emulsion was pipetted onto nitrogen-containing HSM agar along with 2 µL of a droplet destabilizer (RDT 1000, RainDance Technologies) to break the emulsion. The agar plated cells were then exposed to light for 24 hours to trigger

zygospore germination and returned to a 12 hour light / 12 hour dark cycle to resume vegetative algae growth by mitosis[278].

5.3.7 Imaging

Imaging was performed using transmitted brightfield illumination on an inverted microscope (Zeiss Axio Observer, Oberkochen, GER) using a high-speed camera (Vision Phantom V310, Wayne, NJ). Droplet encapsulation videos were acquired at 13,005 frames per second. A customized MATLAB tracking code[279] was utilized to calculate particle and cell spacing and velocities. Particle and cell co-encapsulation statistics were obtained by visually observing high-speed video of the particles and cells during co-encapsulation. Static array videos were acquired intermittently at 100 frames per second.

5.4 Results and Discussion

5.4.1 Co-encapsulation of Polystyrene Microspheres

Before applying the device to living cells, we co-encapsulated separate streams of 10 μm polystyrene microspheres to demonstrate device operation. The results in Figure 5.4a show ordered particle trains at the end of the two channels, which merge at the flow-focusing nozzle. For channel A (top), the longitudinal particle spacing was 24.9 +/- 5.3 μm while the particles traveled at an average velocity of 13.6 +/- 0.1 cm/s. For channel B (bottom), the longitudinal particle spacing was 23.7 +/- 4.3 μm, and the average velocity was 14.1 +/- 0.2 cm/s. Note that the spacing statistics only include particle distances that are less than 45 μm; particles that were further apart were assumed to be a part of a separate train.

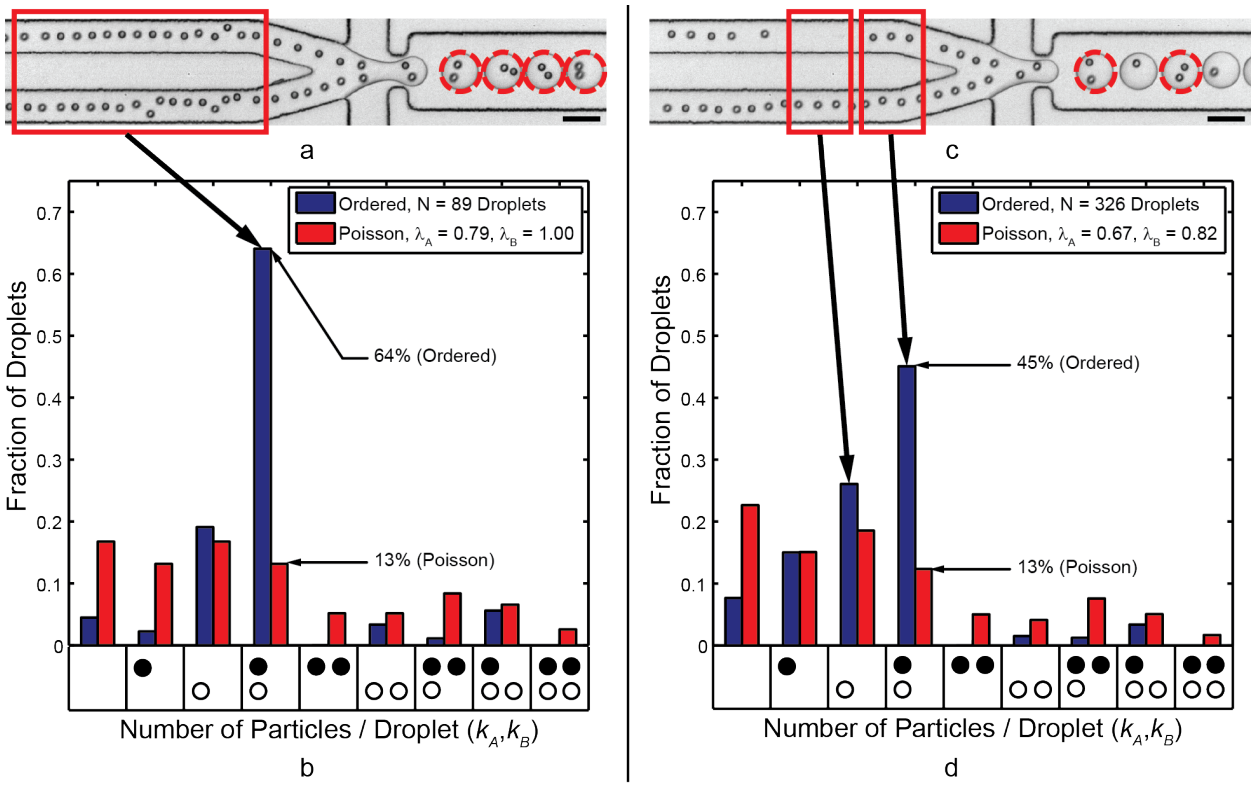

Figure 5.4. Particle co-encapsulation statistics. (a) Co-encapsulation of separate 10 µm polystyrene microsphere trains at 5.8 kHz. The dashed circles highlight droplets that contained one particle of Type A (top channel) and one particle of Type B (bottom channel). (b) Histogram showing the normalized frequency of droplets that contained the number of particles indicated by each x-axis bin. The black circles represent Type A particles while the white circles represent Type B particles, and each bin represents a droplet composition. For average particle A and B concentrations of 0.79 and 1.0 per droplet, respectively, there are few gaps in the trains (see red box). (c) When the local particle concentrations drop to 0.67 and 0.82, respectively, gaps in the ordering trains (e.g., see red boxes) emerged. The co-encapsulation efficiency decreased but still significantly outperformed *Poisson* co-encapsulation. Scale bars in (a) and (c) represent 50 µm.

The combination of particle spacing and velocities imply that the average rate of particle arrival at the flow-focusing nozzle was 5.5 +/- 1.2 kHz for channel A and 5.9 +/- 1.1 kHz for channel B. Note that the instantaneous frequency depended highly on local longitudinal spacing, which is in part a function of particle concentrations λ_A and λ_B[252]. The interparticle spacing was as low as 14 µm for very dense particle suspensions, but less concentrated suspensions led to larger gaps between trains (Figure 5.4c). However, because the droplet generation rate (5.8 kHz) was in line with the particle deliver rate to the flow-focusing nozzle, the statistics presented in

Figure 5.4b show 64% ($= D_{k_A=k_B=1}$) of droplets contained the correct contents: a single co-encapsulation pair. Data in Figure 4b reflects results from two particle trains with relatively few gaps; that is, $\lambda_A = 0.79$ and $\lambda_B = 1.0$. However, the calculated *Poisson* co-encapsulation efficiency (Equation 5.2) is just 13%, so ordered co-encapsulation resulted in a nearly fivefold increase in the number of correctly loaded droplets.

Figure 5.4c and subsequent encapsulation statistics in Figure 5.4d highlight the importance of maintaining both particle concentrations near unity. Specifically, Figure 5.4c shows particle ordering in channels with several gaps between ordered particle trains ($\lambda_A = 0.67$ and $\lambda_B = 0.82$). The train spacing increased due to lower particle concentrations such that the particle frequency at the flow-focusing nozzle dropped to 5.1 +/- 1.1 kHz in channel A and 5.4 +/- 1.3 kHz for channel B. This led to more empty droplets and droplets containing a single particle of either type. Here, the paired co-encapsulation efficiency fell to $D_{k_A=k_B=1} = 45\%$, which is still a nearly fourfold improvement over *Poisson* co-encapsulation. Interestingly, for the results in Figures 5.4c and 5.4d, the bottom train had relatively few gaps ($\lambda_B = 0.82$). As a result, the percentage of droplets containing one and only one Type B particle was still 72.6%. This result agrees well with the single-cell encapsulation efficiency values reported in previous studies[24,235,237] and supports the Equation 5.2 assertion that the encapsulation efficiencies of separate streams are independent.

To see a wider range of local particle concentrations, Figure 5.5 plots the co-encapsulation efficiency data versus the minimum of the Type A and Type B particle concentrations. Intuitively, the minimum particle concentration of the two streams, $\min(\lambda_A, \lambda_B)$, dictates the maximum attainable co-encapsulation efficiency. For example, the co-encapsulation efficiency when $\lambda_A = 0$ particles/droplet would be zero, no matter the value of λ_B. When $\lambda_A = 0.1$

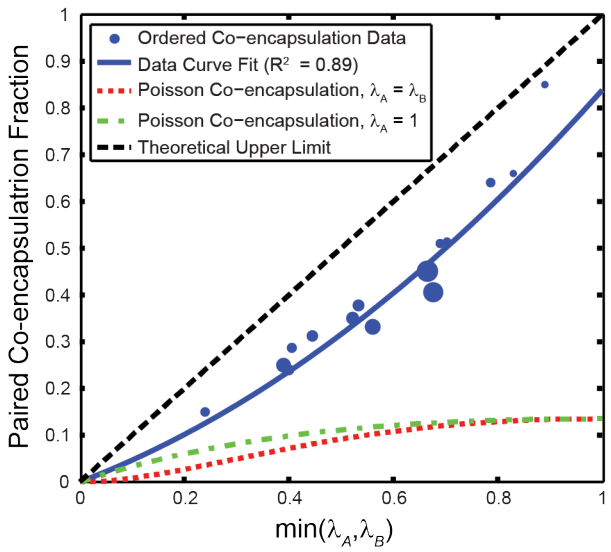

Figure 5.5. Co-encapsulation efficiency versus particle concentration. Here, we plot $D_{k_A=k_B=1}$ of 10 µm polystyrene microspheres versus min(λ_A, λ_B). The theoretical maximum co-encapsulation efficiency is $D_{k_A=k_B=1} = \min(\lambda_A, \lambda_B)$. The co-encapsulation data point size is proportional to the N value, where the smallest marker size corresponds to N = 41 droplets; largest corresponds to N = 326 droplets. For the weighted (by N) curve fit of the form Ax^2+Bx+C, A= 0.4138, B= 0.4247, and C is constrained to 0. Two different Poisson co-encapsulation distributions (using Equation 5.2) are plotted using both $\lambda_A = \lambda_B$ (a likely design situation) and $\lambda_A = 1$ (where the $D_{k_A=k_B=1,Poisson}$ is maximized).

particles/droplet, the theoretical maximum co-encapsulation efficiency $D_{k_A=k_B=1}$ is also 0.1. We infer that, for λ_A and λ_B less than one, the theoretical maximum co-encapsulation efficiency is linearly proportional to the minimum concentration such that $D_{k_A=k_B=1} = \min(\lambda_A, \lambda_B)$, reaching a maximum of unity when $\lambda_A = \lambda_B = 1$. The data and weighted curve fit illustrate that when the ordered particle concentrations are very low, the likelihood that individual trains, while ordered, reach the nozzle at the same time also becomes similar to *Poisson* statistics. When the particle concentrations increase towards unity, fewer gaps in the trains leads to better pairing efficiencies.

While empty droplets and single-cell containing droplets are problematic, they are not as problematic as droplets containing incorrect groupings of multiple cells (0/2, 2/0, 2/1, 1/2, etc.), especially when considering FACS sorting based on fluorescent signal strength. For example, FACS may not be able to discern between a strong signal exhibited by a particularly active cell

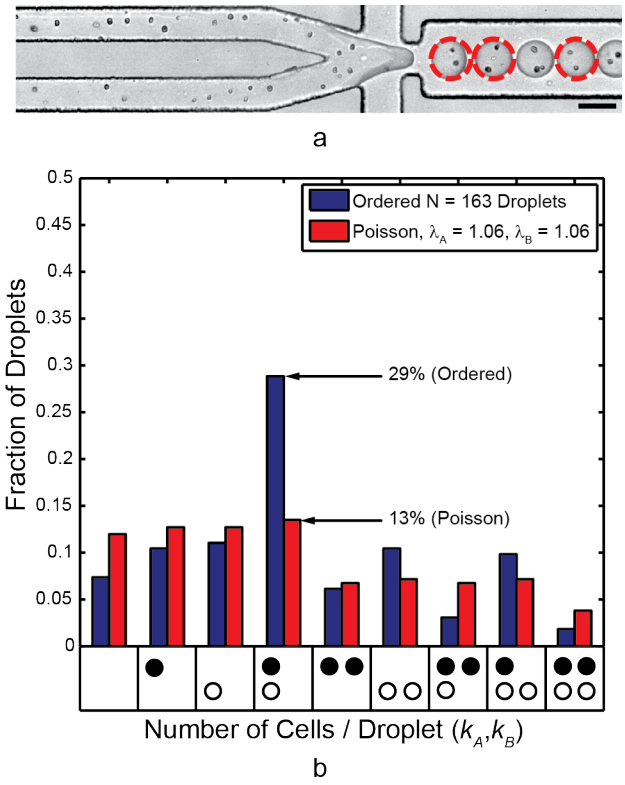

Figure 5.6. Algae cell co-encapsulation statistics. (a) Co-encapsulation of separate mt+ (Type A, top) and mt- (Type B, bottom) *C. reinhardtii* cell trains at 6.0 kHz. The dashed circles highlight droplets that contained one cell of each mating type. The scale bar represents 50 µm. (b) This histogram presents the normalized frequency of droplets that contained the number of cells indicated by each x-axis bin. The black circles represent mt+ and the white circles represent mt- cells, and each bin represents a droplet composition. While ordering quality and encapsulation efficiency were decreased compared to the 10 µm microsphere case, the paired encapsulation efficiency was over a twofold improvement to *Poisson* co-encapsulation.

pair from a strong signal that may be the cumulative result of having multiple cell groups in a droplet. Despite the decrease in efficiency due to the less than optimal particle concentration in Figure 5.4c and Figure 5.4d, a metric to define the ratio of droplets containing one-to-one co-encapsulation to those containing incorrect groupings ($D_{k_A=k_B=1}/D_{k_A \text{ or } k_B>1}$) was 7.4, as opposed to 0.4 for the *Poisson* case. In other words, of all the droplets containing two or more particles, 88% of those contained "correct" pairings while only 28% would have contained correct pairing for the *Poisson* case. Thus, one could also sort based solely on the number of

cells in a droplet (without additional cell labeling) with significantly higher confidence that the droplet contains two separate cell types.

5.4.2 Co-encapsulation of Microalgae Gametes

Trains of mt- (Type A) and mt+ (Type B) *C. reinhardtii* cells are shown in the upstream ordering channels of Figure 5.6a. Here, cells traveled downstream with an average speed of 16.6 +/- 0.5 cm/s in channel A (top) and 16.7 +/- 1.6 cm/s in channel B (bottom). Visually, the cell trains also appear to be less ordered. Here, the longitudinal cell spacing was 25.7 +/- 8.8 μm in channel A and 26.8 +/- 12.2 μm in channel B. This leads to the immediate observation that cell focusing and ordering quality (uniformity of cell velocity and cell train spacing), was degraded when compared to the case of 10 μm particles. A major factor in this change was a decrease in the particle Reynolds number Re_p (as low as 0.16 for 5 μm cells while 0.62 for 10 μm particles). In other words, with cell diameters as low as 5 μm, the decrease in Re_p was fourfold for the smallest cells. The average cell diameter (major axis length) was 7.7 +/- 1.1 μm ($Re_p \sim 0.37$) while the average minor axis length was 6.5 +/- 1.0 μm. Based on cell spacing (not including train gaps over 45 μm) and velocity, the cells in Figure 5.6a reached the nozzle at a frequency of 6.4 +/- 2.2 kHz for channel A and 6.2 +/- 2.9 kHz for channel B. Droplets, 57 pL on average, were generated at 6.0 kHz.

It is critical to note that while Re_p can be raised by simply increasing flow rates, droplet generation places conflicting design constraints on these flow rates. The Weber number ($We = \rho U^2 D_h/\sigma$) represents the ratio of inertial forces of the aqueous flow to interfacial tension forces. The Capillary number ($Ca = \mu U/\sigma$) represents the ratio of viscous forces from the oil flow to interfacial tension forces. Aqueous fluid properties are used for calculating We, and oil phase

properties are used for calculating Ca. For both quantities, σ represents the interfacial tension between the immiscible fluids, and all geometrical dependent quantities are taken at the flow-focusing nozzle. For small We and Ca (both << 1), droplets form at the nozzle when the oil flow pulls droplets from the main aqueous flows. As We approaches 1 (higher aqueous flow rates), the aqueous stream begins to "jet" as inertial forces shoot the droplet interface downstream, leading to unstable droplet generation. As Ca approaches 1 (higher oil flow rates), the oil phase tends to pull the aqueous stream into long, thin jets[51]. Neither inertial jetting nor Capillary jetting is acceptable for controlled encapsulation. For ordered co-encapsulation, adding a second channel roughly doubles the aqueous flow rates at the nozzle. As a result, channel and nozzle geometries must be carefully designed so that the flow rates are sufficient for ordering but small enough to avoid the transition from droplet generation to jetting.

While the ellipsoidal cell size variation and shape are not directly addressed here, some previous studies[280,281] have addressed the effect of particle and cell shape on inertial focusing. Note that these studies separated focused streams of particles based on shape and did not address ordering and interparticle spacing. Additional, flow rates were much higher (40-80 μL/min) than allowed for low Weber number droplet generation in our device. Our device did induce strong ordering of the ellipsoidal algae cells using the 31 μm x 44 μm device and a thinner 22 μm x 44 μm device with flow rates on the order of 15-20 μL/min. At the combined flow rates, however, the Weber number was too high, and inertial jetting ensued at the flow-focusing nozzle.

Despite the decreases in longitudinal ordering quality, the co-encapsulation statistics, presented in Figure 5.6b, still demonstrate a twofold improvement over the *Poisson* case for the same cell concentrations. Gametes were paired at an encapsulation efficiency $D_{k_A=k_B=1}$= 29%

compared to a *Poisson* encapsulation efficiency of 13%. Table 1 shows results for additional experiments. As previously noted, the most problematic droplets for FACS sorting are those containing two or more of either cell type. The ratio of droplets containing correct pairings to those containing incorrect groupings ($D_{k_A=k_B=1}/D_{k_A\ or\ k_B>1}$) was 0.7 but still higher than 0.4 (the *Poisson* case). Of all the droplets containing two or more cells, 42% of those were "correctly" paired ($D_{k_A=k_B=1}/D_{k_A+k_B\geq 2}$) while only 22% would be correctly paired in the *Poisson* case. To achieve this same $D_{k_A=k_B=1}/D_{k_A\ or\ k_B>1}$ = 0.7 ratio in the *Poisson* case, the values of λ_A and λ_B must be 0.29, implying a co-encapsulation efficiency of 4.7% using Equation 5.2. In that sense, the current data represents a sixfold improvement over *Poisson* co-encapsulation.

Table 5.1. Algae Co-encapsulation Data.

N	λ_A	λ_B	$D_{k_A=k_B=1,Poisson}$	$\boldsymbol{D_{k_A=k_B=1,Data}}$
60	0.98	0.92	13%	**42%**
63	0.76	0.89	13%	**32%**
80	0.81	0.73	13%	**31%**
105	0.80	1.11	13%	**29%**
163	1.06	1.06	13%	**29%**

5.4.3 Mating Reaction

Under typical culture conditions, *C. reinhardtii* produces asexually through mitosis. However, the ability of *C. reinhardtii* to sexually reproduce provides an extremely relevant application for co-encapsulation. When subjected to nitrogen starvation under continuous light exposure, vegetative cells convert to gametes (through either direct conversion or mitosis). Each *C. reinhardtii* strain is genetically predetermined to form gametes which are either mating-type minus (mt-) or mating-type plus (mt+)[265,273]. When mt- and mt+ cells meet, agglutination

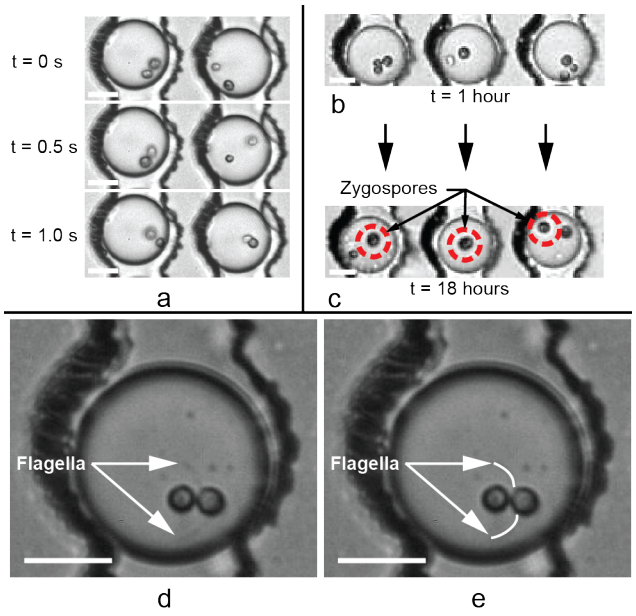

Figure 5.7. Droplets immobilized using static *Dropspot*[134] arrays for tracking individual *C. reinhardtii* gamete pairs. (a) Time sequence taken 30 minutes post-encapsulation and 1 hour following removal from the thermal deflagellation bath. In the left droplet, mating had begun prior to the t = 0 s frame (t = 0 selected arbitrarily. In the right droplet, the mt+ and mt- algae cells swam in the droplet but then agglutinated between t = 0.5 s and 1.0 s. (b,c) Successful mating was determined by comparing the number of cells in each droplet one hour post-encapsulation (b) to the number of cells 18 hours post-encapsulation (c). In droplets where mating occurred, the decrease in the number of cells indicated the number of mating reactions that took place. Additionally, mating was further confirmed by the presence of a larger zygote (indicated by the circles in (c)), formed from the fusion of the mt+ and mt- cells. Unmated gametes in (c) remained motile. (d,e) Close-up view of flagellar agglutination. The original image is shown in (d), and visible flagella have been traced in (e) to highlight their presence. Flagella remained in motion as the cells prepared to fuse. Scale bars in (a-d) represent 20 μm.

proteins on their flagella initiate adhesion of the cells, gamete activation, and ultimately cell fusion to form a diploid zygote. Upon suspension in nitrogen-containing culture media after at least five days in dormancy, the zygospore will initiate separation into four recombinant haploids, two of which are mt+ and two of which are mt-, but all of which are genetically distinct[265].

Figure 5.7a shows two cases of encapsulated algae in a static droplet array[134] containing a pair of cells which had begun mating (left) and another pair where initial agglutination is captured in a time sequence of images (right). Figures 5.7d and 5.7e show a close-up of flagellar entanglement (agglutination) between two algae gametes in a droplet

approximately 30 minutes post-encapsulation and 1 hour following removal from the thermal deflagellation bath. This agglutination time (1 hour post-deflagellation) matches a previous study[275], where resumption of mating capability occurred between 45 minutes and 2 hours for gametes deflagellated using pH shock.

Zygote formation was deemed successful by comparing the number of cells visible in a droplet shortly after encapsulation to the number of cells 18 hours later (sufficient time to fully mate). Figures 5.7b and 5.7c show the decrease in the number of algae in each droplet due to gamete fusion and zygote formation. Gametes not involved in a mating reaction remained motile in the droplets shown. Of 341 droplets examined, 179 droplets contained two or more algae cells following encapsulation. Of these 179 droplets, 18% contained zygotes after 18 hours, and 7% contained zygotes originating from a droplet containing one and only one cell of each mating type.

For more rigorous mating statistics, one could stain either the mt+ or mt- mating type to distinguish between the two following encapsulation. However, a fluorescence stain must penetrate a thick cell wall and then cleave within the cell. Initial attempts to stain one *C. reinhardtii* mating type with fluorescein, fluorescein diacetate, calcein, and calcein AM did not yield adequate fluorescence signals to differentiate between the stained and unstained mating types, even at high stain concentrations. These particular stains are optimized for animal cells, which lack cell walls and are thus easier to penetrate than algae cells. An additional stain (BODIPY 505/515)[282] was successful in staining the algal lipid bodies but diffused from the stained cell type into the unstained type too quickly (on the order of seconds) to differentiate between mating types.

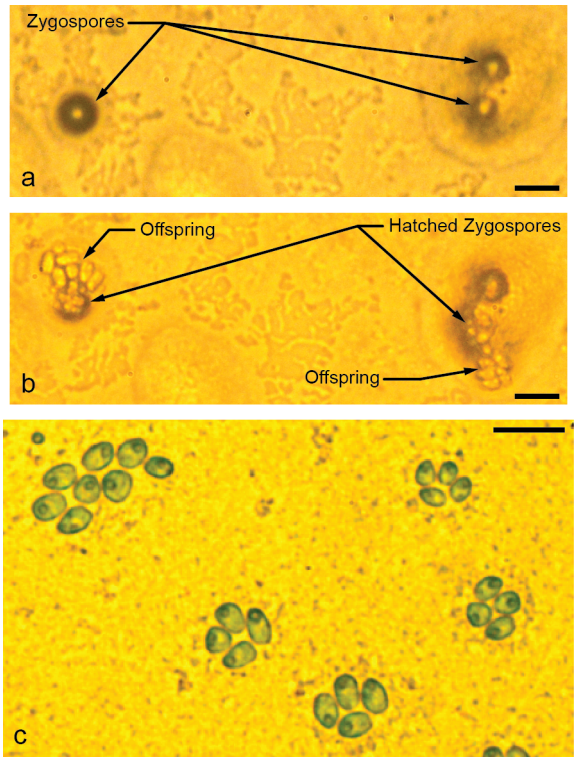

Figure 5.8. Algal zygospores, plated on complete nutrient agar media seventeen days post-encapsulation. (a) Three zygospores on high salt media (HSM) agar, three days following plating on agar. (b) The following day, two of the three zygospores had germinated into tetrads and broken out of their zygospore shells. Based on the number of cells shown, the vegetative cell tetrads had also begun asexual reproduction by mitosis. **(**c) Mitosis on HSM agar, three days following agar plating. Scale bars in (a), (b), and (c) represent 20 µm.

5.4.4 Zygospore Maturation

The *C. reinhardtii* mt+ and mt- co-encapsulation emulsion sample was stored in the dark at room temperature for 17 days following encapsulation. Aside from ambient air gas diffusion, no additional nutrients or media were supplied to the droplets or the cells they contained. After 17 days, a number of zygospores were visible, along with smaller, unmated cells. Remarkably, some of these smaller cells appeared motile despite that no additional nutrients or light energy were supplied. Assuming that zygospore germination did not occur in the absence of light and nitrogen, we inferred that these surviving cells were unmated gametes. However, since the original composition of specific droplets in the collected emulsion was unknown (the bulk

emulsion was not held in an indexed array), we could not deduce the fraction of gametes that survived in the droplet during this time. Zygospores are adapted to survive long periods of starvation by forming a thick, protective wall, and other long-term survival behaviors have been documented[265]. Resting cell spores of *Chlamydomonas nivalis*[283], have shown the viability after multiple years in dry, frozen storage[265]. One study[258] used nano-liter scale droplet encapsulation to study *Cholorella vulgaris* algae growth rates for 33 days. Another growth rate study[257] encapsulated *C. reinhardtii* cells in 270-pL droplets, where cells remained viable in the droplets after 10 days. Still, 17-day gamete survival in 57-pL droplets observed here was surprising. One explanation for the extended survival of some gametes is that the cells fed on their own lipids. Triaglycerol lipids, a potential source for algal biofuel[269], are generated as a stress response when the cells are starved in nitrogen-free media for gametogenesis.

Figure 5.8a shows three zygospores following agar plating but prior to hatching. Figure 5.8b shows the broken zygospores, 24 hours later, with offspring and subsequent mitosis. To further demonstrate viability, Figure 5.8c shows a resumption of mitosis of additional cells on agar plates. Since the emulsion contained zygospores and unmated gametes, we could not determine if the cells shown here resulted from single-cell mitosis or zygospore hatching. Still, the ability to survive 17 days in a droplet and resume asexual reproduction for single cells is even more significant.

5.5 Conclusions

We have described a new device that merges parallel, ordered cell trains at a flow-focusing droplet nozzle. The resulting co-encapsulation statistics showed significant improvement in pairing separate particle and cell types in droplets at multi-kHz rates. This

device showed an improvement in one-to-one co-encapsulation of mt+ and mt- *C. reinhardtii* algae gametes from 13% in the *Poisson* case to 29% in the ordered co-encapsulation device. Note that using typical dilutions with the same ratio of paired cell droplets to incorrectly grouped cell droplets, the predicted *Poisson* encapsulation efficiency was on the order of 5%. For larger 10 μm polystyrene microspheres with higher Re_p, the improvement in paired co-encapsulation efficiency was fivefold, from 13% in the *Poisson* case to 64% for ordered co-encapsulation.

Moreover, we have demonstrated the long-term survival of algae cells in microdroplets. Following thermal deflagellation, hydrodynamic self-ordering, encapsulation in 57 pL droplets, and flagellar regrowth, mt+ and mt- *C. reinhardtii* gametes maintained their ability to sexually agglutinate and form a zygote within a droplet. Furthermore, zygospore maturation and gamete survival continued in the extremely confined environment for 17 days, far longer than for animal cells.[284] Subsequent agar plating resulted in zygospore hatching and vegetative offspring expansion by mitosis. The long-term survival and ability to resume both sexual and asexual reproduction highlights the remarkable survival ability of *C. reinhardtii* cells and may set a record for duration of cell survival in sub-100 pL droplets at ambient temperature.

When encapsulating a single algae cell from a single unique line, all cells and resulting asexual offspring are theoretically identical. Droplet confinement could lead to the identification of rare cells due to mutations during mitosis, but these mutations may be slow unless induced. Sexual mating provides unique offspring from each mating event. Completing the zygospore maturation and re-introduction of nitrogen media within the droplet would provide four unique offspring that are isolated from the bulk cell population. From this droplet, new, isolated strains are contained and may be screened for new, useful phenotypes. Following sorting, selected cells could be re-suspended in media for asexual reproduction of the new strain. Exploiting controlled

encapsulation of single or multiple cells can accelerate high-throughput screening of microalgae for improved biofuel (or other) desirable traits. More broadly, new avenues are opened for studying the basic biology and applications of cell-cell interactions.

Chapter 6

Inertial Focusing and Ordering in Low Aspect Ratio Microchannels using Reference Frame Tracking and Rotation Measurements

6.1 Abstract

Previous studies have exploited inertial microfluidics to passively manipulate cells into droplets. However, relatively few studies have investigated the ordering phenomenon that takes place upstream of the droplet generation nozzle. To gain insight into inertial microfluidics, this study uses a motorized microscope stage moving along the length of a low aspect ratio ($W > H$) channel at up to 10 cm/s. This moving reference frame provides a Lagrangian view of particles to obtain more complete time dependent trajectory and rotation histories from the channel inlet to outlet. We observed monodisperse particle dynamics, rotations, and interactions over time scales significantly longer (exceeding a 30-fold increase) than tracking in static reference frames. The results present new insight into particle interactions which showed quasi-steady state equilibrium spacing which oscillated at a constant frequency at a fixed flow rate, which is different from the damped oscillatory interactions suggested in the literature. The average spacing showed little dependence on flow rate, but the oscillation frequency was dependent both on flow rate and particle size.

6.2 Introduction

Earlier chapters have focused on applications of inertial microfluidics to control cell encapsulation. However, controlled encapsulation designs have resulted from empirical results of

interparticle and cell spacing, as well as trial and error in designing channel dimensions and flow rates suitable for both ordering and droplet formation. Here, we attempt to gain insight into inertial microfluidic focusing and ordering by tracking dynamic particle trajectories from the channel inlet to outlet.

As discussed in Chapter 3, inertial lift forces push particles of finite size to a thin, "focused" annulus at a radial position, known as the Segre-Silberberg radius, in cylindrical tube flows[13]. In rectangular microchannels, particles focus to one of four (or eight) quadrilateral symmetric positions centered on the channel faces[18,143,227-229]. The first step of focusing, i.e. "primary focusing" occurs along the short channel dimension, along the steepest velocity gradient. In this initial step, shear gradient and rotation forces are balanced by a repulsive wall force, resulting in an equilibrium cross-sectional position[20,226]. In a very high or low aspect ratio channel, the flow profile becomes similar to that of parallel plates. In our device, undisturbed laminar velocity profile simulations indicate that U_{max} at the vertical channel centerline is constant for 75% of the lateral interior section as determined by single-phase flow simulations. Thus, most particles away from the lateral channel walls (see Figure 6.1) experience only a single focusing and ordering step in the vertical direction (in and out of the field of view).

From Chapter 3, the flow inertia and particle size parameters combine via the Reynolds number $\mathrm{Re_c}$ and particle Reynolds number $\mathrm{Re_p}$, given by

$$\mathrm{Re_c} = \frac{\rho U_{max} D_h}{\mu}, \text{ and} \tag{6.1}$$

$$\mathrm{Re_p} = \mathrm{Re_c}\left(\frac{a}{D_h}\right)^2, \tag{6.2}$$

where ρ, U_{max}, D_h, μ, and a represent the fluid density, maximum channel velocity (for the undisturbed flow), channel hydraulic diameter, fluid dynamic viscosity, and particle diameter, respectively.

Based on scaling arguments of the lift force near the channel centerline ($F_L \propto \rho U_{max}^2 a^3 / H$, Equation 3.4), larger particles reach a focusing position at a shorter downstream focusing length. One review[20] proposed a metric for calculating the dynamic focusing length L_f from the inlet. The metric is based on balancing the inertial lift force near the centerline with a Stokes' drag force on the particle as it moves laterally from the channel centerline to its focused position. Assuming no particle interactions, the focusing length is given by

$$L_f = \frac{\pi \mu H^2}{\rho U_{max} a^2 f_L}, \tag{6.3}$$

where f_L is an empirical lift coefficient. Numerical analysis[247] has suggested that the lift coefficient is dependent on the vertical particle position z and $\mathrm{Re_c}$, although the analysis assumed the particle was of vanishing size and did not disrupt the flow[247]. It is also important to note that Equation 6.3 assumes that the particle starts at the centerline, but the particle distribution at the inlet is more likely to be random than concentrated at the centerline, so particles starting nearest to the equilibrium z position will focus the most quickly. However, for a random distribution, the average inlet position is the centerline, thus the "average" particle would be represented by Equation 6.3, which can be re-arranged to infer that $L_f/H \propto 1/\mathrm{Re_p}$.

When focused particles interact, they tend to "order" in trains with equal streamwise spacing between particles[234,252,285]. This particle spacing is partly dependent on particle size[285] and the number of discrete trains depending in part on particle concentration[252]. Particle trains have been exploited for efficient cell encapsulation in droplets[24,237,238] (See Chapters 4 and 5) and in flow cytometry applications[19,239].

This study utilizes a motorized microscope stage moving along the channel length at up to 10 cm/s and provides a Lagrangian view of particles to obtain more complete time dependent trajectory, rotation, and interaction histories from the randomly distributed inlet condition to the

downstream positions. Here, we utilize a low aspect ratio channel to create parallel-plate-like conditions where shear gradients in the short channel direction dominate those in the lateral direction. Specific goals include quantifying particle dynamics, rotations, and simple particle interactions for small groups of particles to ascertain phenomena leading to longer trains.

6.3 Materials and Methods

6.3.1. Fabrication and Materials

A straight rectangular channel of nominal height H = 100 μm, width W = 1,710 μm, and length $L_{channel} \approx$ 13 cm was fabricated using two rigid acrylic sheets (1.5 mm thickness for the bottom, 4.5 mm for the top) to mitigate channel deformation due to internal channel pressure. A strip of double-sided tape, a polyester film with natural rubber adhesive (442 KW, 3M, St. Paul, MN) joined the acrylic sheets. The tape also served as a channel height spacer. Based on the maximum flow rate used in this study and single phase pressure drop correlations[286], we estimated a maximum inlet channel pressure of 1.2 atm and a maximum vertical channel deformation on the order of 1 μm. This estimate assumed a linear stress/strain relation and no adhesive separation from either surface. Tubing was adhered to tubing ports at each end to provide a simple inlet and outlet.

6.3.2. Experimental Setup

In lieu of polystyrene microspheres, we utilized monodisperse 30 μm (7.7% CV) and 60 μm (3.8% CV) diameter glass microspheres (Thermo Duke Standards, Waltham, MA) to take advantage of visual occlusions that were utilized for measurement of particle rotations in flow. We prepared a solution of lithium heteropolytungstate (LST) (Central Chemical Consulting,

Malaga, AU) in distilled water to density match the glass microspheres at ρ = 2,450 kg/m^3 with a resulting dynamic viscosity μ = 5.0 x 10^{-3} Pa-s. The suspension of glass microspheres and LST solution is loaded into a 10 mL plastic syringe. A syringe pump (Nexus 3000, Chemyx Inc., Stafford, TX) provided constant displacement flow from 200 to 1,400 μL/min. Based on the channel aspect ratio and steady-state simulation, the velocity ratio U_{max}/U_{mean} = 1.56.

6.3.3. Imaging

Time-sequential images of the top channel view were captured on an inverted microscope with motorized stage (Axio Observer, Zeiss, Oberkochen, Germany) and a high-speed camera (Phantom V310, Wayne, NJ) with frame rates ranging from 500 to 2,000 frames per second, depending on flow rate. Motorized stage velocities were programmed using manufacturer-provided software (MTBTest, Zeiss) to match estimated particle velocities. With image resolution at 1.6 μm per pixel, sub-pixel resolution MATLAB algorithms for both stage motion[287], particle motion, particle rotation, and particle tracking[279] were utilized to determine absolute and relative positions and velocities. Rotations were measured by calculating the relative position between the center of area and the grayscale pixel center of mass for each particle.

6.4 Results and Discussion

Figure 6.1 shows a typical downstream train formation for 30 μm particles. While it is not clear from the figure alone, the particle trains exhibited staggered ordering, with alternating particle locations between the top and bottom of the channel. Note how the lateral spread of trains across the channel differed from results using PDMS channels, where particle trains are

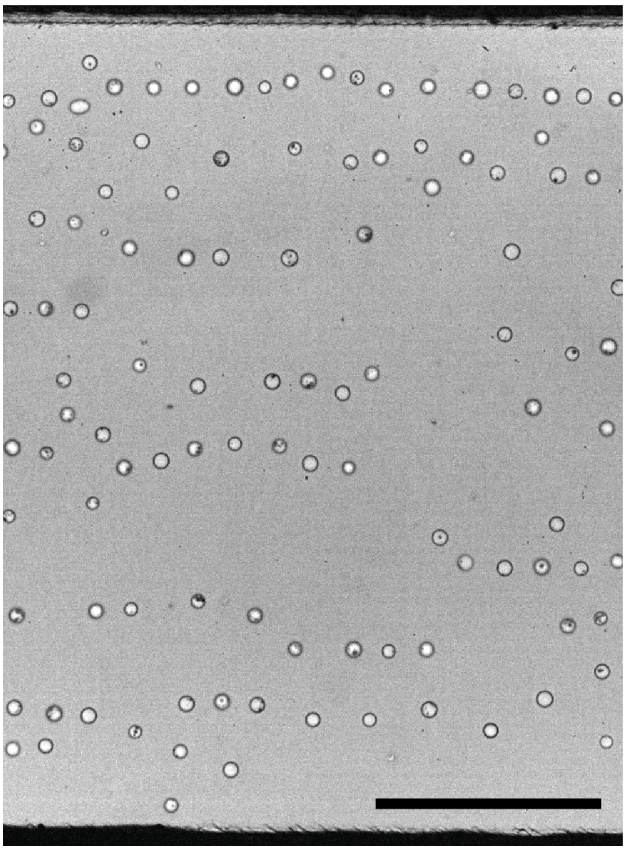

Figure 6.1. Typical glass bead ordering result. Multiple parallel trains of 30 μm particles flow from right to left for $Re_c = 14.6$ and $Re_p = 0.37$. The flow is from left to right, while the stage moves from right to left. The scale bar represents 500 μm.

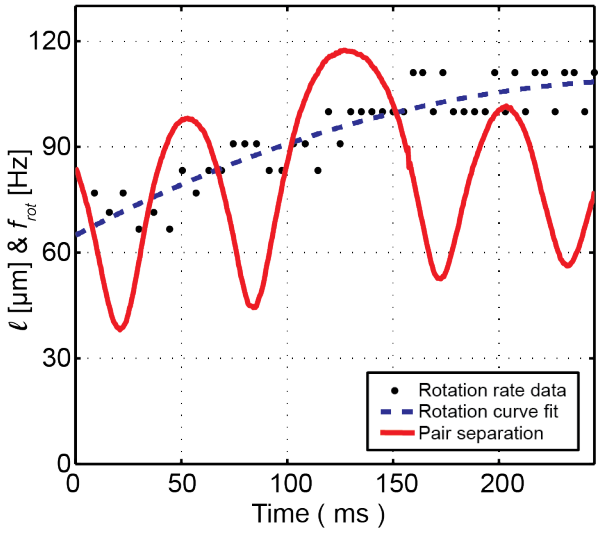

Figure 6.2. Sample particle pair interaction results. Here, $Re_c = 8.43$ and $Re_p = 0.21$. The solid line shows oscillatory relative spacing between two interacting 30 μm particles aligned with the flow. Both particles were on the same vertical side of the channel. The dots and dotted line represent the rotation rate (f_{rot}) of the lead particle.

formed in the center of the channel (see Chapter 5). As opposed to aspect ratios near one, the small shear gradient in the low aspect ratio channel here prevents "secondary focusing" in the lateral direction, a phenomenon described in Chapter 3. Additionally, the reduced channel deformation properties of the acrylic sheets versus elastomeric PDMS channels provide another geometric distinction that is not addressed in depth here.

Table 6.1. Downstream Particle Velocities.

a (μm)	Q (μL/min)	U_{part}/U_{max}
30	600	0.73
30	800	0.73
30	1,000	0.74
30	1,200	0.74
30	1,400	0.73
60	400	0.69
60	600	0.67
60	800	0.68
60	1,000	0.67
60	1,200	0.69
60	1,400	0.69

6.4.1. Downstream Focusing Length

To quantify the extent of inertial focusing and ordering at a given downstream location without measuring the vertical position within the channel, we utilized an assumption, inferred from previous computational results[143], that the downstream velocity of focused particles is constant. We observed that this average particle velocity ratio U_{part}/U_{max} approached a constant value far downstream from the inlet position. This downstream equilibrium velocity ratio is presented in Table 6.1. Thus, when the average particle velocity became uniform with a sufficiently small standard deviation (we selected +/- 1.5% as a cutoff), we inferred that particles had reached their focused positions. Figure 6.3a presents the focusing length versus flow rate for 30 μm and 60 μm particles. While the lift coefficient f_L continuously changes as particles move

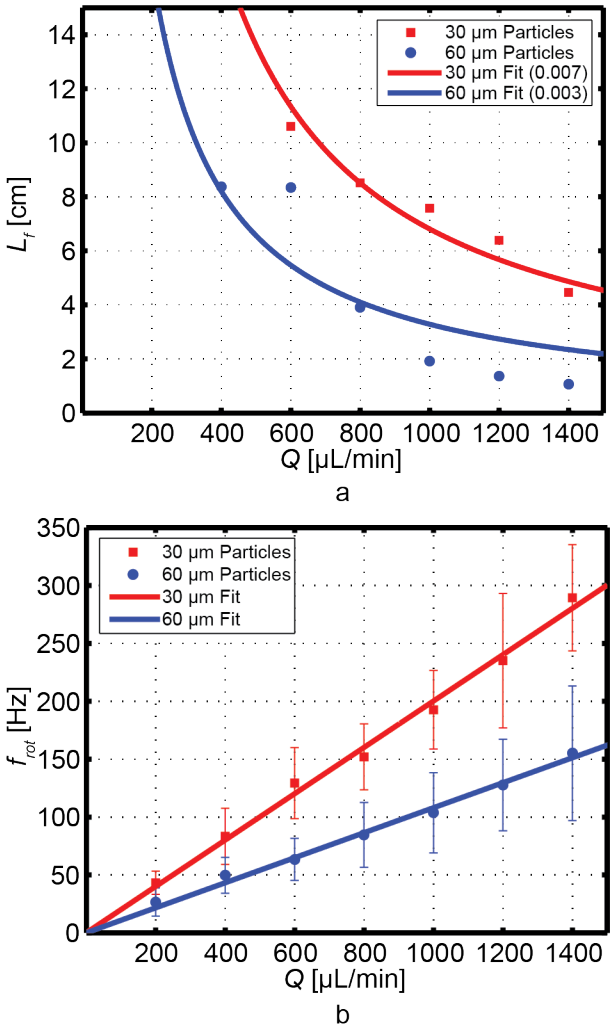

Figure 6.3. Particle focusing length and rotation rate versus flow rate. (a) Channel length L_f required for inertial focusing. Curve fits were obtained by assuming Equation 6.3 f_L values of 0.007 and 0.003 for 30 µm and 60 µm particles, respectively. (b) Particle rotation frequency. Recovered rotation frequencies exhibit a linear scaling with flow rate (R^2 values are 0.992 and 0.991 for 30 µm and 60 µm particles respectively).

across streamlines[247], we experimentally fit an average f_L, which, at first glance, shows a dependence on particle size.

Average rotation rates versus flow rate are also plotted in Figure 6.3b. For two-dimensional parallel plate flow, shear rate is linearly proportional to the flow velocity, thus the linear increase in rotation rate intuitively followed in the data. Additionally, rotation rate

increased with increasing particle size, although the result was not linear. Chapter 7 addresses rotation rate in terms of particle size and local shear rate.

Even for interactions involving two particles, the vertical and lateral positions, trajectory angles, velocities, and rotations contribute to particle interactions. Particles passed each other, "bounced" in a repulsive-like manner, or began moving downstream in tandem. Here, particles typically did not come into direct contact; the wake region of each particle provides the interaction forces. Because the formation of ordered trains is very specific to concentration and initial conditions of a large number of variables, we look here at specific interaction dynamics of single particles, particle pairs, and multiple particle trains in lieu of attempting to solve the complete parameter space.

Figure 6.4 shows the relative position of two paired particles, one on the channel top, and one on the bottom. Note that due to our reference frame tracking apparatus, we tracked the particle pair for 440 ms as compared to just 13 ms for a static reference frame, over a 30-fold increase. While not shown in Figure 6.4, we often observed a relative position decay when particles initially came into contact as suggested by some computational studies[252]. However, Figure 6.4 shows a quasi-equilibrium center-to-center spacing with oscillatory particle interaction of nearly constant amplitude and oscillation frequency about a constant average spacing. Note that the change in relative position after t = 1,100 ms occurred after the pair collided with another particle.

The non-dimensional average quasi-equilibrium spacing l/a observed was largely independent of flow rate (Figure 6.5a). While only two particle sizes were used here, it is interesting to note that the actual particle spacing (in μm) was independent of particle size at all flow rates tested. Figure 6.5b shows particle quasi-equilibrium spacing oscillations at additional

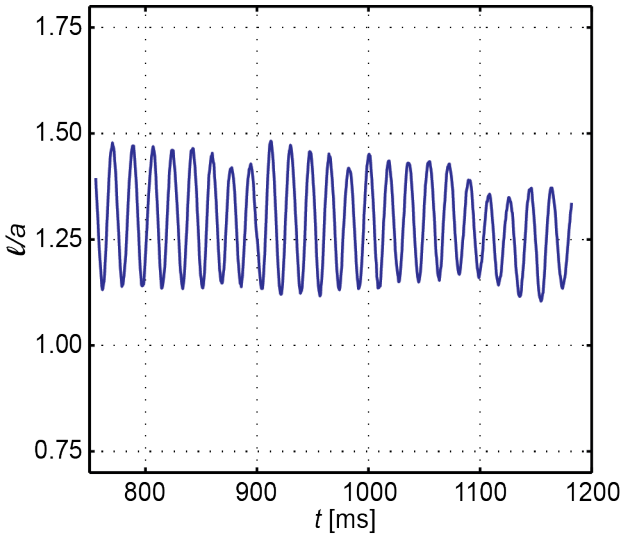

Figure 6.4. Center-to-center relative spacing for a pair of 60 μm particles. The non-dimensional relative spacing l/a represents the streamwise separation for Re_c = 14.59 and Re_p = 1.47. The two particles were on opposite vertical sides of the channel. Note the nearly constant oscillation frequency (~56 Hz) until t = 1,100 ms, where another particle collided with the pair.

flow rates and particle sizes. As shown in Figure 6.5b, particle spacing oscillated at frequencies that increased with flow rate. Note that larger error bars for the 1,200 and 1,400 μL/min flow rates occurred because the average particle velocities were faster than the maximum stage velocity. Thus, these particles were tracked for shorter time periods than those at lower flow rates.

Besides the interaction of particles ordered on alternating sides of the channel, we found different interaction behaviors for particle pairs which were ordered on the same channel sides. The relative position plot shown in Figure 6.2 represents the case where particles on the same side of the channel approached but then repelled each other sharply as if the particles "bounced" off one another. For particles on opposite sides of the channel (Figure 6.4), the relative spacing was more sinusoidal.

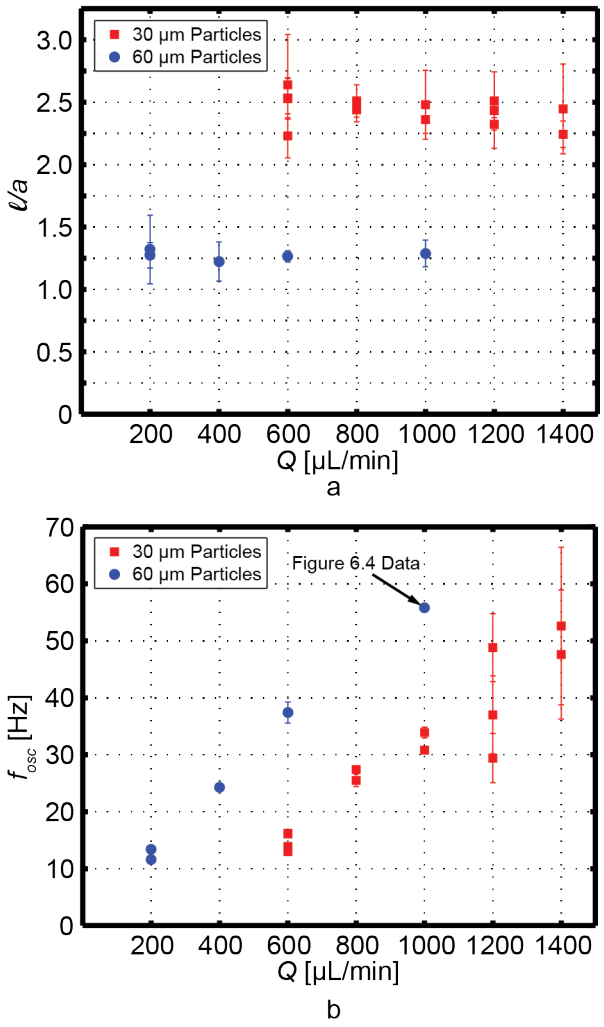

Figure 6.5. Particle pair spacing and oscillation. (a) Average non-dimensional center-to-center relative spacing *l*/*a* versus flow rate for particle pairs. Note that the actual center-to-center spacing (in µm) for the two particle sizes is nearly equal for all flow rates. (b) Oscillation frequency in relative spacing versus flow rate for particle pairs. The data point derived from Figure 6.4 is called out.

Expanding the interactions to triplets, quadruplets, and higher number particle trains, increased complexity was quickly encountered; typically, single particles or additional groups encountered another group, temporarily disrupting the quasi-equilibrium. Figure 6.6a shows a train interaction between five particles, plotting relative position of each particle in the train with respect to the lead particle. The relative position fluctuated as the train developed, followed by

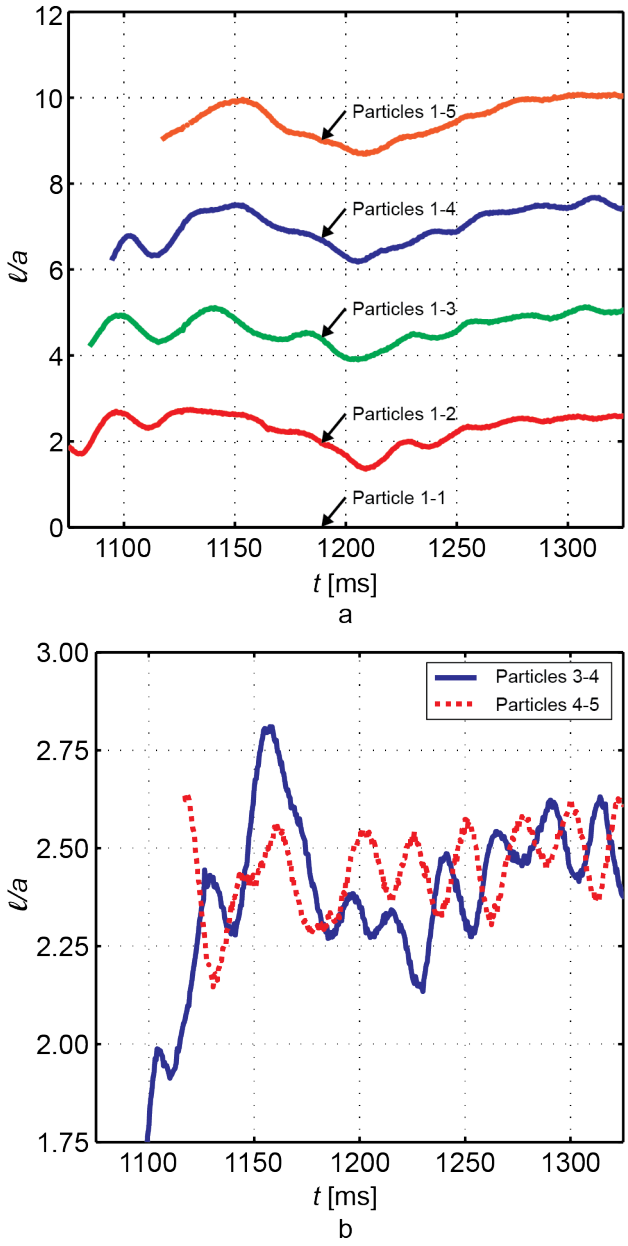

Figure 6.6. Longer particle train interactions. (a) Relative non-dimensional particle center-to-center spacing *l*/*a* for a five 30 μm particle train at Re_c = 14.6 and Re_p = 0.37. Each plotted line represents the respective relative position from Particle 1, with the y-axis representing Particle 1. Following perturbations, the train reached quasi-steady equilibrium with relatively equal spacing. (b) Relative spacing between the 3-4 particles and the 4-5 particles, respectively for the train shown in (a). Note the evolution to a 180° phase angle in relative position.

quasi-steady equilibrium spacing between particles on the order of the pair spacing. Figure 6.6b plots the relative position between the respective Particle 3 and 4 and then Particle 4 and 5 in the train. The superposition plot of relative positions indicates an eventual 180° phase angle,

suggesting that Particle 4 “bounced” between Particles 3 and 5. However, more complex phase shifts were also observed and depended on a large number of factors including train size.

It is important to study the simpler interactions of pairs and triplets because we observed that many of these small groups then join other “base” units to form longer trains downstream. As trains become longer, the possible combinations of particle interactions quickly become complex, where even the possible binary arrangements of the channel sides on which the particles reside, (i.e. top-bottom-top, top-top-bottom, top-top-top, etc.) grows as 2^N, where N is the number of particles in a train.

6.5 Conclusions

Here, we have provided a method to track particle flows using a moving reference frame. Many particle interactions could not have been observed using a stationary reference frame. Key conclusions include the linear relationship between rotation and flow rate, quantification of focusing length, and the lack of dependence of interparticle spacing on flow rate. Figures 6.2, 6.4, and 6.6 highlight the complex, long-lived interactions that highlight the high utility of reference frame tracking.

In order to generalize the data to cover the parameter space required to non-dimensionalize parameters relating to particle spacing, oscillations, and rotations caused by hydrodynamic particle disturbances in flow, one would need to increase the experimental ranges of flow rates, fluid properties, and particle concentrations beyond the scope of work presented here. Still, given the number of variables and possible interactions, computational parametric studies with both increased parameter space and controlled interaction conditions may be better suited for non-dimensional analysis. These computational studies may be calibrated using the

experimental results shown here for guidance on initial and equilibrium conditions. Chapter 7 expands on the idea of reference frame tracking further to increase the parameter space, and couple experimental and numerical results to maximize the utility of both methods.

Chapter 7

Fundamentals of Inertial Microfluidics for Droplet Encapsulation and Cytometry Design Applications

7.1 Abstract

The work of Chapter 6 provided a Lagrangian view into interparticle dynamics through a moving reference frame. Here, we expand on the reference frame tracking by systematically investigating the effect of particle size, flow rate, and channel geometry on ordering behavior. We tested two different channel geometries that have been used in previous applications to couple the underlying two-phase fluid mechanics with the design of practical devices. We varied the channel Reynolds number Re_c from 3.78 to 30.23 and particle Reynolds number Re_p from 0.07 to 2.39. A moving microscope stage, equipped with low-friction air bearings, provided a Lagrangian reference frame such that individual particles and trains can be tracked for long period of time, often 40-50 times longer than in stationary reference frames. Using particle trajectories, we found that downstream ordering length scaled as $1/Re_p$, which provides challenges for the ordering of smaller cells. We also found that the interparticle forces scaled as Re_c^2. Coupling experimental results with computational modeling, we have simulated several experimental cases for particle pairs. The numerical results match our experimental results and provide additional data on particle shear forces and rotation rates, both of which are important data when considering the effect of inertial microfluidics on biological cells.

7.2 Introduction

Previous chapters, Chapter 3 in particular, have addressed the tendency of particles and cells to migrate across streamlines to "focused" equilibrium cross-stream channel positions. Briefly, focusing has been exploited for size-based cell separations in straight[230,231] and curved channels[15-18,144]. Ordered trains of focused particles and cells, with equal longitudinal spacing between each, provide additional applications in flow cytometry and controlled encapsulation.

Focusing and ordering occur in distinct primary and secondary stages (Figure 7.1a) and at sufficiently high channel Reynolds number and particle Reynolds number, given below.

$$\mathrm{Re_c} = \frac{\rho U_{max} D_h}{\mu} \tag{7.1}$$

$$\mathrm{Re_p} = \mathrm{Re_c}(a/D_h)^2 \tag{7.2}$$

Here, a, ρ, U_{max}, D_h, and μ represent the particle/cell diameter, fluid density, maximum channel velocity (for the undisturbed flow), channel hydraulic diameter, and fluid dynamic viscosity, respectively.

Applications utilizing focusing and ordering have largely relied on trial and error. Additionally, only a handful of studies address particle interactions in flow. In this study, we aim to provide a more fundamental understanding of particle and cell ordering mechanics to provide more *a priori* knowledge for design of applied microfluidic devices. Using a range of polystyrene particles as cell surrogates, we cover a wider parameter space to ascertain train spacing, particle velocity, and fundamental behaviors of self-ordering trains.

Here, we use a moving microscope stage to provide Lagrangian reference frame tracking of particles and cells in microchannel flows at particle velocities on the order of 1 m/s. On a

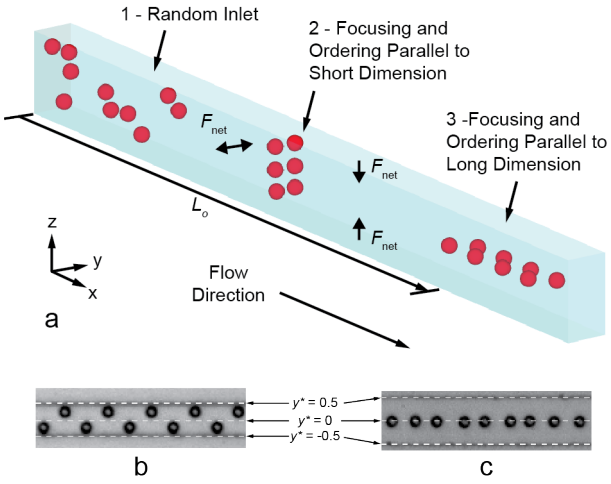

Figure 7.1. Schematic of focusing and ordering in a rectangular microchannel. (a) Particles first focus (but may or may not order) in the *y* direction, parallel to the short channel dimension (2). Particles then migrate in the *z* direction, parallel to the centerline of the long channel face. Interparticle forces lead to staggered, ordered trains at (3). (b) 10 µm particle ordering in a high aspect ratio ($H > W = 27$ µm) channel. (c) 10 µm particle ordering in a low aspect ratio ($W = 40$ µm $> H$) channel. Note that the ordering in (b) and (c) are identical, except that (b) looks at the channel from the top (as shown in (a)), and (c) views the channel from the side. As shown in (b) and (c), we define the dimensionless lateral position in the channel $y^* = 0$ at the centerline. At the channel walls, $y^* = \pm y/W$.

stationary microscope stage, particles are only visible for a short period of time. Using both a motorized microscope stage and a custom, high-speed air bearing stage, we track particle histories as they focus and form ordered trains. In many cases, the time a particle is in view is increased by a factor of 40 or more. As a result, we document train dynamics that could not have been observed using a stationary reference frame. Combining experimental results with computational simulation, we present phenomenological and quantitative interparticle dynamics, including interparticle force measurements that scaled with Re_c^2. Using experimental results as initial conditions, we also present a numerical model which provided additional quantification of interparticle forces and rotations. The coupling of experimental and numerical results, combined with an existing expression for rotation rate in linear flow, provided a predictive model for the rotation rate of microspheres in microchannel flows.

7.3 Materials and Methods

7.3.1 Channel Fabrication and Setup

Two different channel geometries were used for parametric experiments on the high-speed air stage. The "high" aspect ratio ($H > W$) channel measures 27 μm wide by 52 μm high (to match the ordering from previous single-channel ordered encapsulation work)[24]. The "low" aspect ratio ($W > H$) channel measures 40 μm wide by 31 μm high and is similar to dimensions used in previous ordered co-encapsulation work[238]. Results from a third geometry (24 μm wide by 36 μm high) demonstrate tracking of live algae cells.

Devices were fabricated using standard soft lithography techniques[4]. Briefly, master molds were produced by exposing a SU-8 photoresist layer (Microchem 2050, Newton, MA) with ultraviolet light through a 50,000 dpi patterned mylar mask (FineLine Imaging, Colorado Springs, CO). Polydimethyl siloxane (PDMS) (Dow Corning Sylgard 184, Midland, MI) elastomer was mixed at a 10:1 w/w base to curing agent ratio, poured onto the master mold, and cured at 65º C overnight. After peeling the PDMS from the mold, the polymer was cut to size, and tubing ports were created with a biopsy punch. The resulting PDMS channel was then bonded to a 3"x1" glass slide using a handheld corona discharge treater[254] (Electro-Technic Products BD-20AC, Chicago, IL) or an oxygen plasma cleaner (Harrick PDC-32G, Ithaca, NY) and left overnight.

Polystyrene particle suspensions were delivered from a syringe to the channel inlet via 0.01" ID Tygon microbore tubing. The channel flow rate was controlled from 1.25-40 μL/min using a positive displacement syringe pump (Chemyx Nexus 3000, Stafford, TX). Three particle sizes were used: 5 μm (4.8 μm actual size, CV < 5%, Thermo G500, Waltham, MA), 10 μm (9.9 μm actual size, CV < 5%, Thermo G1000), and 15 μm (15.02 μm actual size, CV = 1.0%,

Thermo 4214A). The nominal channel Reynolds numbers Re_c and Particle Reynolds numbers Re_p ranged from 3.8-30.2 and 0.1-5.4, respectively (using μ = 1.12x10^{-3} Pa-s and ρ = 1,000 kg/m^3). Note that the maximum channel velocities using in calculating Re_c are dependent on aspect ratio and were determined using numerical solution correlations for three-dimensional laminar flow in a rectangular channel[271]. The ratio U_{max}/U_{mean} was 2.006 for the 27x52 μm channel (aspect ratio α = 0.52) and 2.076 for the 40x31 μm channel (α = 0.78). The syringe was rotated periodically to avoid sedimentation clumping in the syringe[237].

7.3.2 Algal Culture and Deflagellation

For algae experiments, microalgae *C. reinhardtii* UTEX-90 strain (UTEX, Austin, TX) were cultured in soil water media using an orbital shaker plate (SCILOGEX SK-180-Pro, Berlin, CT) at 160 RPM. The culture temperature and gas composition were maintained at ambient conditions. The cell cycle was synchronized using a 24 hour light/dark cycle, i.e. 12 hours in light followed by 12 hour in darkness. Reversible flagella removal was achieved using techniques described in previous work[238]. Briefly, an algae-containing microcentrifuge tube was submerged in a 40º C water bath for 30 minutes immediately prior to loading in a 1 mL syringe. As with particles, sedimentation and cell clumping were avoided by rotating the syringe every 2 minutes.

7.3.3 Imaging

Visualization was performed using transmitted brighfield illumination on an inverted microscope (Zeiss Axio Observer, Oberkochen, Germany). High-speed video was obtained using a high-speed camera (Phantom V310, Wayne, NJ) at up to 6,100 frames per second. Custom

MATLAB algorithms were used in conjunction with a tracking algorithm[279] to determine particle trajectories, velocities, accelerations, and spacing.

7.3.4 Moving Air Stage

For the algae cell tracking in Figure 7.10, a motorized stage (Zeiss) provided the moving reference frame at up to 10 cm/s. The microfluidic device was secured to the stage using tape to avoid shifting during stage motion. The stage control software provided initial motion upstream of the inlet (to accelerate the stage to its maximum velocity prior to entering the field of view), moved the stage from the inlet to outlet of the channel, and then decelerated and stopped far past the channel outlet.

For the higher-speed particle tracking, a custom "air stage" provided translation at speeds up to 1 m/s (although the stage is capable of up to 4 m/s). Briefly, the microfluidic device was mounted to a cart (Figure 7.2). This cart was supported by two air bearings (New Way, Aston, PA), each attached to polished steel rails to allow for near-frictionless motion (Figure 7.2c). Figure 7.2 shows the stage mounted on the inverted microscope. While the air stage was equipped with an optional air piston for "launching" the cart, we manually accelerated the cart approximately 25 cm upstream of the microscope field of view, through which the cart smoothly glided. The stage was vertically aligned to remain in focus at the vertical center of the channel.

For both the motorized stage and air stage, the velocity was validated by co-fabricated markings on the microfluidic device and subsequent image processing. Figures 7.2c and 7.2d show a measured velocity profile and stage position versus time, respectively. From inlet to outlet, the stage maintained velocity within 2% of the inlet velocity. Combined with the particle tracking relative to each frame, we infer the particle velocity

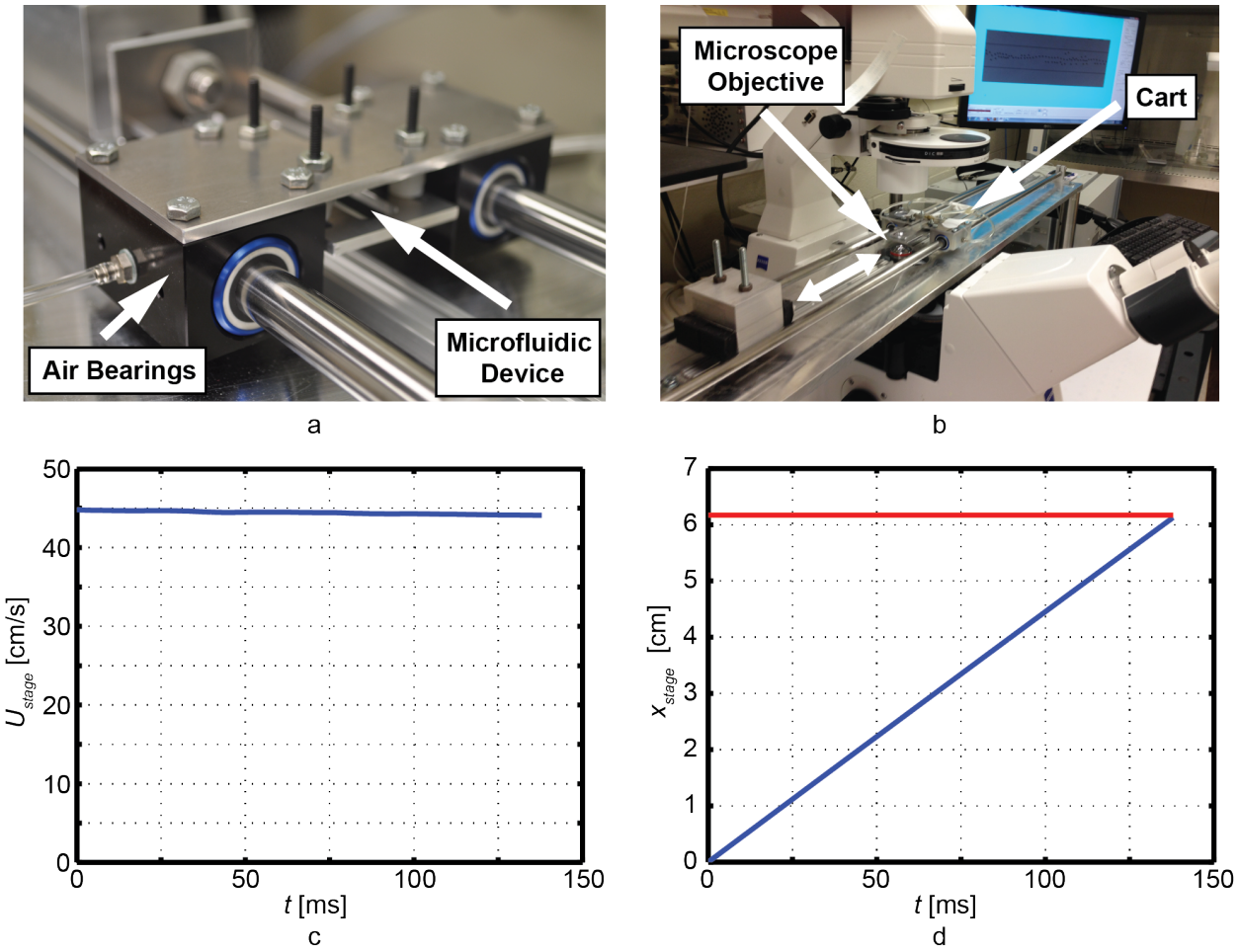

Figure 7.2. High-speed air bearing stage. (a) Air bearing cart mounted to parallel rails. The PDMS device is secured to the cart and then vertically aligned by tightening the adjustment nuts. (b) View of high-speed air stage mounted above the inverted microscope. The mounting posts on each end of the stage provide for micron-level height adjustments within the field of view. (c) Typical air stage velocity profile. While there is some variation, the maximum variation is often less than 2% and is accounted for in subsequent error analyses. (d) Measured downstream position and channel length for the velocity profile in (c). The actual channel length for the 27x52 µm channel (6.1 cm, red line) matches that inferred in (d).

$$U_p = U_{rel} - U_{stage}, \tag{7.3}$$

where U_{rel} is the particle velocity in the image reference frame and the stage velocity U_{stage} is negative, i.e. the stage travels in the opposite direction of flow.

7.3.5 Computational Model

We have also created a time-dependent, three-dimensional finite element model for two neutrally buoyant spherical particles in rectangular channel flow using COMSOL Multiphysics (Version 4.2a, Burlington, MA). Using experimental results as initial conditions, the model provides transient and equilibrium particle spacing, velocities, rotations, and interparticle forces. Briefly, the "Two Phase Flow, Moving Mesh" node was utilized where a moving mesh boundary was constructed at the continuous phase/solid particle interface. Both particles were modeled as a viscous fluid, with artificially high viscosity (μ_p = 10,000 Pa-s) and interfacial tension (σ = 10,000 N/m), to simulate solid bodies. As a result, this method can model solid particles, droplets, cells, and other viscoelastic materials.

To ensure continuity, the model matched the velocity, normal stress, and shear stress at the interface and assumed no mass flow across the particle interface. The resultant forces on the interface led to particle motion (lateral and rotational) through the continuous phase. When the mesh deformed due to lateral motion, the "Automatic Remeshing" node generated a new mesh when the minimum element quality fell below a minimum threshold.

Fully developed laminar flow conditions were assumed at the domain inlet and outlet. In lieu of periodic boundary conditions, the model constantly updated the wall velocity by accelerating both wall and fluid domains using a body force. This PID loop control kept the particles near the center of the computational domain without affecting the underlying two-phase flow physics.

7.4 Results and Discussion

7.4.1 Particle Ordering in 27x52 Channel

Ordering Length

Figure 7.3 shows the ordering length, i.e. the downstream length at which particles in the stream reached an ordered configuration, in a 27x52 μm channel. In applications, the ordering length represents the required channel length, essentially a minimum device footprint. We argue that as particles interact and become "ordered", their relative velocities tend to zero, i.e. particle spacing becomes constant. We define an ordering length L_o at which:

$$\sigma_{rel}^{*} = \frac{\sigma}{U_{max}} \leq 1.25\%, \tag{7.4}$$

where σ is the relative velocity standard deviation, σ_{rel}^{*} is the dimensionless relative velocity standard deviation, and U_{max} is the maximum undisturbed channel velocity at the nominal channel dimensions. We also define the ordering length error such that the lower and upper error bounds due to velocity measurement error correspond to σ_{rel}^{*} values of 1.5% and 1.0%, respectively. The point at which σ_{rel}^{*} (smoothed to avoid false positives due to noise) crossed the threshold corresponded to each length. Additional errors due to downstream channel position and scaling uncertainties have been incorporated into the error bars of Figure 7.3.

Note that due to the lack of imaging at multiple channel heights, the vertical position could not be precisely resolved using the tracking stage. Thus, we could not explicitly distinguish the primary focusing (parallel to the short channel dimension) from the secondary focusing and ordering (parallel to the long channel dimension). In subsequent low aspect ratio channel results, we show that this assumption may not be adequate to fully demonstrate the two steps of focusing and ordering. Figure 7.3a shows the ordering length L_o as a function of Re_p for the three tested particle sizes. Like the suggested scaling for focusing length L_f[20], L_o/H scaled as $1/Re_p$. In

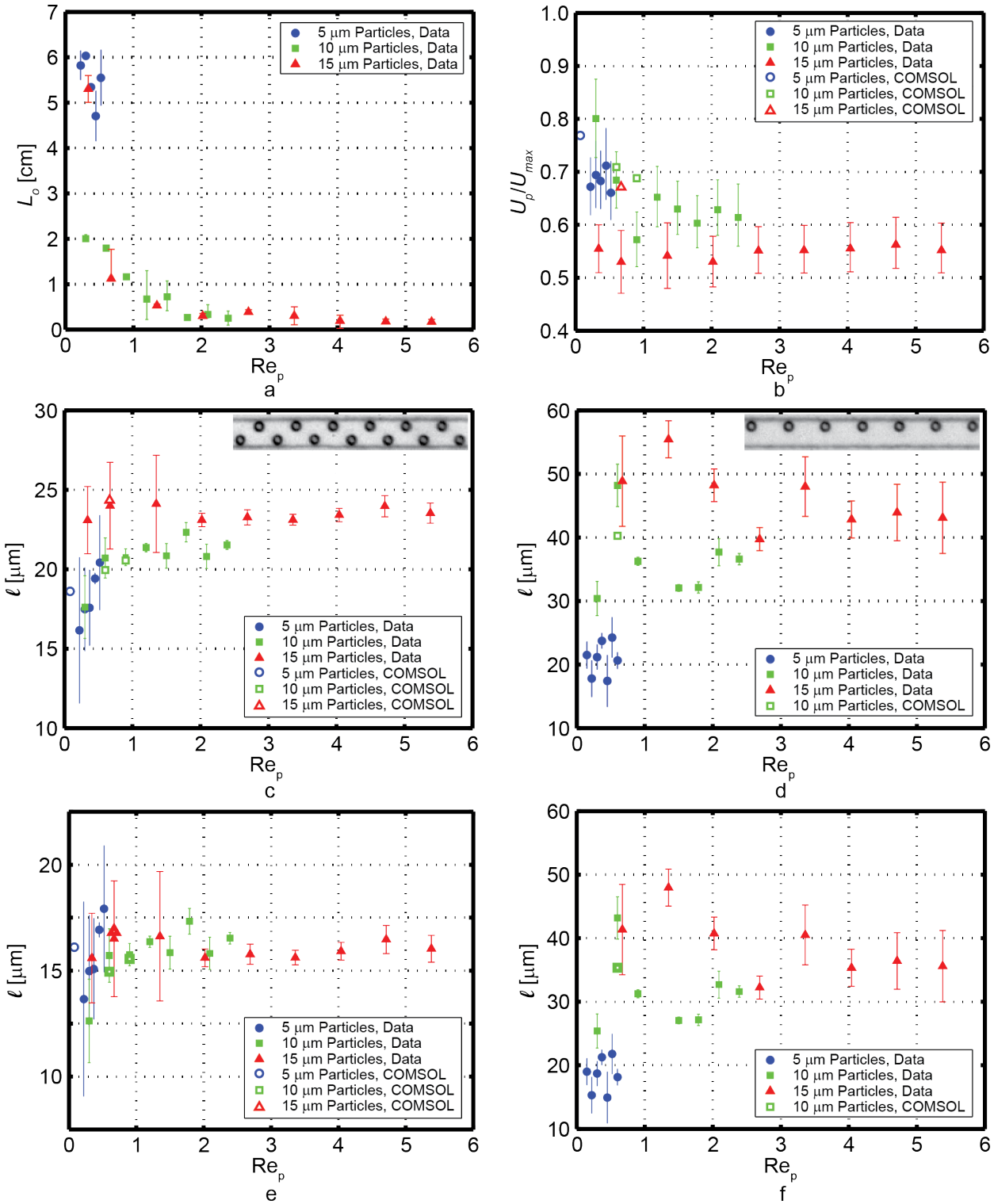

Figure 7.3. Dynamic tracking and equilibrium results for a 27x52 μm channel. (a) Ordering length L_o (Equation 7.4). (b) Particle velocity at equilibrium, normalized by U_{max}. (c) Center-to-center streamwise particle spacing for staggered trains. (d) Center-to-center particle spacing for trains on the same lateral side of the channel. (e) Surface-to-surface streamwise spacing for staggered trains. (f) Surface-to-surface particle spacing for trains on the same lateral side of the channel. For (a) and (b), each data point represents at least two independent trials. For (e) and (f), each data point represents at least two particle trains over at least five frames.

previous controlled encapsulation work, which ordered 10 μm particles[24,238] and cells[24] using the same channel dimensions, the flow rate was limited to just over 10 μL/min to avoid aqueous jetting at the flow-focusing nozzle. However, for 5 μm particles here, complete ordering did not occur below 15 μL/min (Re_p = 0.22). From an application standpoint, this underscores the need for an optimization of channel cross-section, channel length, and aqueous/oil interfacial tension to achieve controlled droplet encapsulation for cells less than 10 μm in diameter[238,259].

One previous study[232] has noted that the focusing length decreased with flow rate in PDMS channels, but then increased at higher flow rates (Re_c > 40). Channel deformation was not addressed. While our study is limited to Re_c ~ 30, upstream PDMS channel deformation at these higher flow rates was significant. For Re_c ~ 30 (40 μL/min flow rate), the channel width measured 35 μm near the inlet, an increase of 30% from the nominal 27 μm value. The height of the channel could not be ascertained from our data, but the deformation in the vertical direction was likely on a similar order of magnitude. At even higher flow rates, de-lamination of the oxygen plasma bond occurred.

Particle concentration also impacts ordering length. Consider that in the data of Figure 3 for 10 μm particle ordering at Re_p = 1.20, the ordering length L_o = 0.67+/- 0.45 cm. For this data, the average particle concentration fraction was 0.066 (v/v). For more concentrated particles where the volume fraction was 0.095, L_o = 1.12+/- 0.35 cm. While the regions do statistically overlap, it was noticeable that with higher concentrations, unordered particles tended to disrupt the ordering patterns such that ordering did not fully occur until further downstream. Taking the extreme limit of a particle fraction approaching 1.0, particles would likely never order. In the

other extreme limit of particle concentration tending to zero, particles would also slowly order due to the small statistical probability of particle interactions. Thus, there is likely some optimal concentration that minimizes the ordering length. However, the most optimal concentration from a practical perspective may be one that orders such that there is precisely one particle per spacing unit l to avoid any gaps in the trains, even at the expense of ordering length.

Particle Velocity

The particle velocity is important for predicting particle and cell positions as well as quantifying interparticle forces (more on forces in subsequent sections). Due to the channel deformation, the particle velocity and interparticle spacing data shown in Figures 7.3b, 7.3c, and 7.3d were taken near the channel outlet (within 2.5 mm), where PDMS deformation was smallest. While the deformation near the channel outlet was minimal, the error bars for U_p/U_{max} include an estimate for the deformed cross-sectional area immediately at the channel outlet. This deformation in part accounts for the larger spread in particle velocity statistics than those in a previous study, which used larger channel dimensions (50x50 μm) and experienced smaller pressure drops[143].

Figure 7.3b shows the equilibrium particle velocity, non-dimensionalized by the nominal maximum channel velocity. For the 5 μm and 10 μm particles, this dimensionless particle velocity U_p/U_{max} was in the range of 0.65-0.70, which was noted in previous work. The experimental values for 15 μm particles (U_p/U_{max} from 0.5-0.6) did not coincide with the results of previous velocity measurements in square channels[143] or with numerical COMSOL simulations performed in this study (U_p/U_{max} = 0.67). Previous experimental work using PDMS particles in square channels included larger particles such that the maximum particle size a/H =

0.9 yet still found U_p/U_{max} = 0.67 for all particle sizes. It is possible that for the largest polystyrene particles used in this study led to wall contact with the channel that was not accounted for in the model or experienced in previous experiments. Table 7.1, which contains COSMOL model results, also shows a decrease in U_{slip}, i.e. an increase in U_p/U_{max}, for a 5 μm particle when compared to 10 μm and 15 μm particles. This is intuitive in that a vanishingly small particle would approach the undisturbed velocity U_∞.

Particle Spacing

Combined with particle velocity, particle spacing is critical for cytometry and encapsulation design. Streamwise spacing distance l (center-to-center) for staggered particle trains is shown in Figure 7.3c. For the 5 μm and 10 μm particles, it is important to note the larger error bars, which are the result of incomplete or unstable ordering and indicate weaker interparticle forces. Thus, dependencies on particle size and flow rate are unclear at small Re_p. For larger particles and larger flow rates, the equilibrium spacing trends are more clear. The center-to-center spacing, most important for encapsulation and cytometry applications, appears to have only slight dependence on size. However, it is also important to note that the surface-to-surface spacing (the center-to-center spacing minus one particle diameter) was statistically constant across all particle sizes and Re_p (Figure 7.3e).

The center-to-center spacing distance l for trains of particles on the same lateral side of the channel appears to have much greater dependence on particle size (Figure 7.3d). Also notable is that the equilibrium configuration appears to be less stable, as indicated by the larger error bars and spread in spacing data. This complements the data of Figure 7.10, which showed the ability for cells on the same side of the channel to reconfigure into staggered ordered trains.

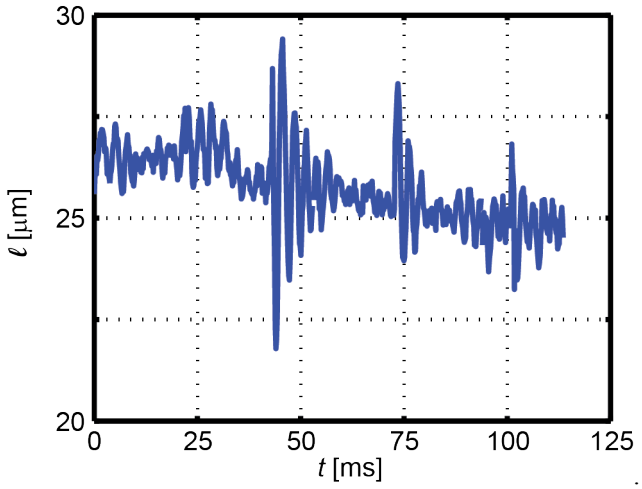

Figure 7.4. Effect of PDMS deformation on particle spacing. Dynamic center-to-center spacing for a 15 μm particle pair in a 27x52 μm channel at 20 μL/min (Re_p = 2.69). The pair was tracked over 100 ms, and 2.3 cm, a nearly thirtyfold increase over a stationary reference frame. The quasi-equilibrium spacing decreased further downstream, where PDMS channel deformation was less prominent.

To further illustrate the impact of PDMS deformation on particle spacing, Figure 7.4 shows particle pair spacing for a 15 μm particle pair at 20 μL/min (Re_p = 2.69) over 100 ms and 2.3 cm traveled. At this flow rate, a single-phase pressure drop for an un-deformed 27 μm by 52 μm channel, over the entire length, was estimated at 3.8 atm[286]. While the deformation reduces the pressure drop by increasing the local hydraulic diameter, the value was still significant. During the time interval in Figure 7.4, the channel width decreased from 30.5 μm to 27.8 μm. Thus, it is important to note that particle spacing decreased as the width decreased (while U_{max} and the shear rate increased).

As a comparison, we have also modeled 10 μm particle pairs in square 50x50 μm channels at Re_c = 20 and Re_p = 0.80 (Table 7.1). At an average shear rate U_{max}/h ~ 17,900 [1/s] (where $h = H/2$), the interparticle spacing was 34.70 μm. At a similar shear rate to the 27x52 channel with U_{max}/h ~ 17,600 [1/s]), the spacing was 20.55 μm. Thus, shear rate, held relatively constant between the two geometries, was not the driving factor for the different spacing.

Force Scaling

To quantify basic particle interactions, we focused here on particle pairs to avoid complex interactions of larger trains. We used video data from particle pair interactions at a range of flow rates and compare the results to transient COSMOL simulation. Figure 7.5a shows the interaction of two 10 μm particles in flow at $Re_p = 0.30$. The relative center-to-center spacing l and relative velocity $U_{p,rel}$ between the particles are shown in Figure 7.5a and Figure 7.5b, respectively. Figure 7.5c shows the COSMOL simulation for both $Re_p = 0.30$ and 0.60. While the same damped oscillatory pattern links the experimental data to simulation, the relative velocity magnitudes do not compare well because of different initial conditions in the particle approach. However, we plot a dimensionless streamwise force F^*, given by

$$F^* = \left(\frac{\partial U_p'}{\partial t}\right)\left(\frac{a}{U_{slip}^2}\right). \tag{7.5}$$

From Chapter 3, one parameter of importance in lift is the slip velocity U_{slip}, given by

$$U_{slip} = U_p - U_\infty, \tag{7.6}$$

where U_p is the particle velocity and U_∞ is an undisturbed velocity at the same lateral position in the absence of a particle[226].

The scaling of Equation 7.5 represents the ratio of the relative interparticle force to the common expression for the drag force on a sphere in flow, given by

$$F_D \propto \rho U_{slip}^2 \frac{\pi}{4} a^2. \tag{7.7}$$

Briefly, Equation 7.5 was derived by dividing the measured relative force (Force = mass x measured relative acceleration) by Equation 7.7. Figure 7.5d plots F^* versus center-to-center particle spacing l for experimental and simulation data. The value of U_{slip} was taken from COMSOL simulation data (Table 7.1). As Table 7.1 data suggests that U_{slip} scales linearly with

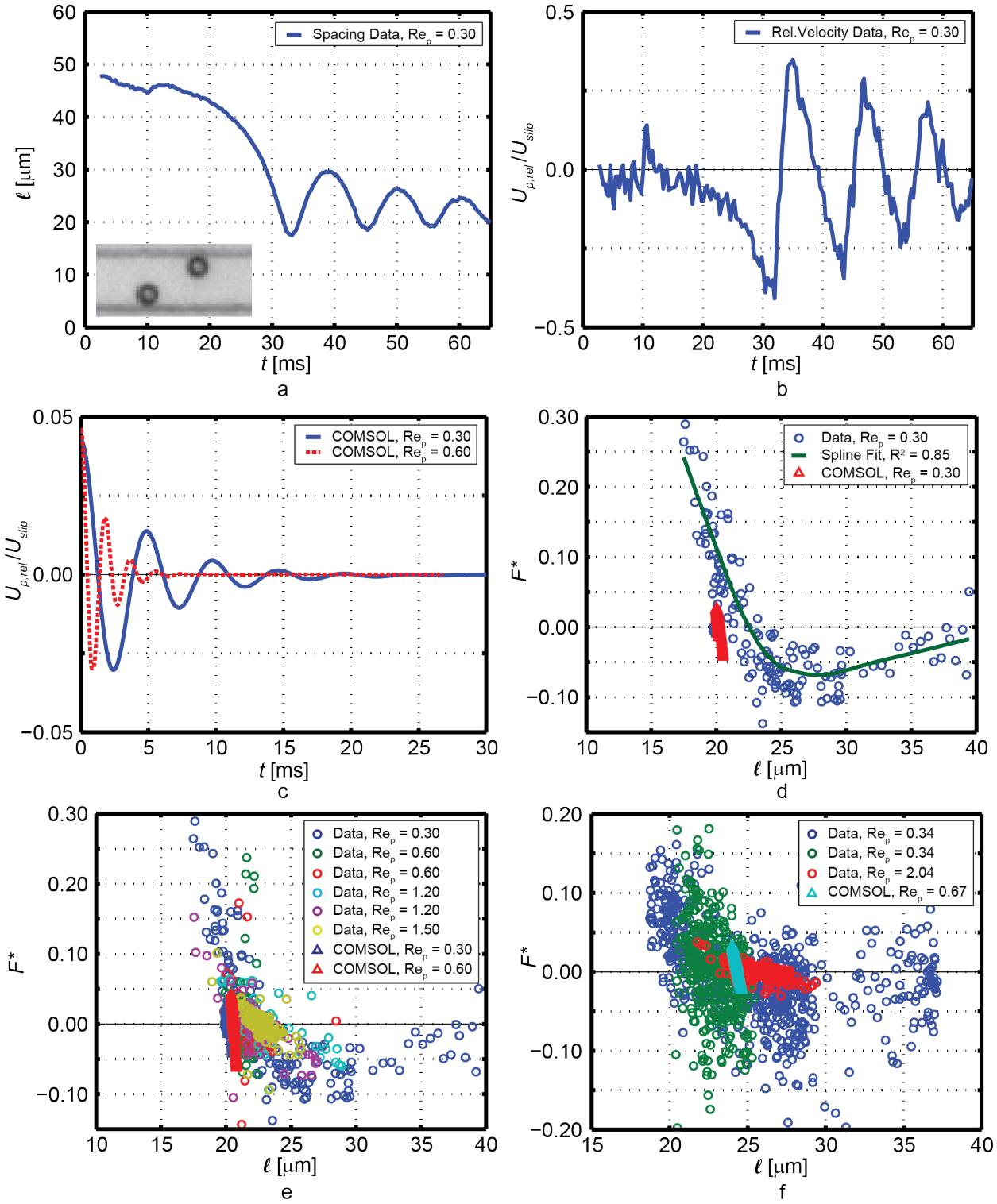

Figure 7.5. Pair spacing, relative velocities, and interparticle forces. (a,b) 10 μm particle pair spacing (a) and dimensionless relative velocity $U_{p,rel}/U_{slip}$ (b). (c) COMSOL results (10 μm particles) for $U_{p,rel}/U_{slip}$. (d) Dimensionless force profiles for experimental and COMSOL data. (e) Experimental and computational force profiles for 10 μm particles pairs. (f) Experimental and computational force profiles for 15 μm particle pairs. Note that for calculations from position data in (b)-(f), velocity and acceleration data has been smoothed to reduce noise due to pixel uncertainty.

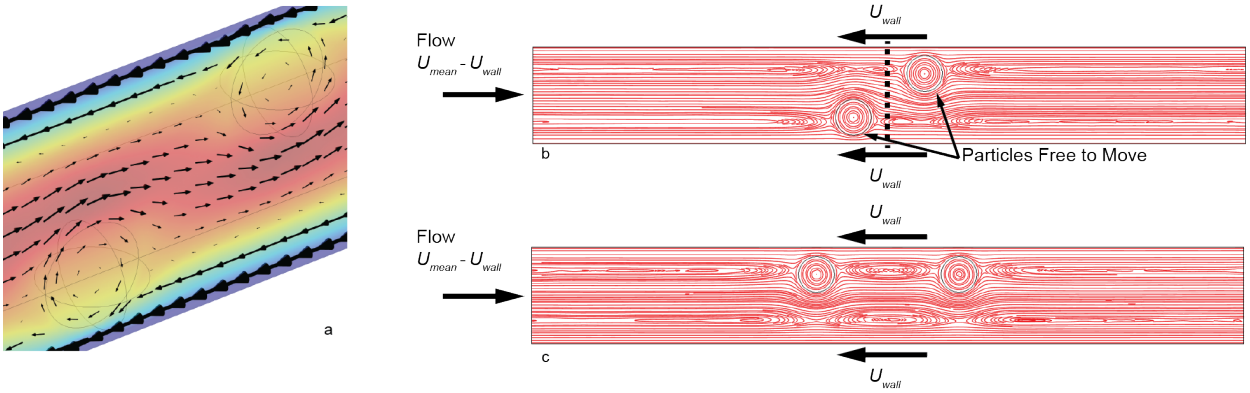

Figure 7.6. Typical COSMOL model results. (a) Center plane slice of the three-dimensional computational plane. Arrows indicate the direction and magnitude of flow relative to the particles. (b) Center plane streamlines for a 10 µm particle pair at Re_c = and Re_p= where the pair is in the staggered train formation. (c) Center plane streamlines for a 10 µm particle pair at Re_c = and Re_p= where both particles are ordered on the same side of the channel with longer spacing between particles. In the model, particles are free to move, but a body force PID loop keeps the average position of the two particles near the centerline.

flow rate, U_{slip} values were extrapolated for additional flow rates. The data, along with a smoothed spline fit, showed a weak attractive force at long distances. Following a maximum attractive force, the force quickly decreased, changing sign at the equilibrium spacing. As the particles became very close, the now repulsive force quickly increased. After a minimum spacing, the particles began moving apart from each other, and the cycle continued about the equilibrium position. The COMSOL results did not cover the large particle separation range of the experimental data but did provide a similar force profile near the equilibrium spacing.

We plot data at additional Re_p for 10 µm (Figure 7.5e) and 15 µm (Figure 7.5f) particles. In both cases, the experimental and simulation data appear to collapse to the same force profiles using the dimensionless relation of Equation 7.5. While we did not resolve the scaling based on particle size, the results for constant particle size suggest that the interparticle ordering force scaled as U_{slip}^2 for constant particle size. In practical terms, the interparticle forces scale with Re_c^2, as U_{max}, U_p, and thus U_{slip} all vary linearly with flow rate.

Table 7.1. COMSOL Simulation Results.

Channel Size	**27x52**				**50x50**
Particle Size	**5 µm**	**10 µm**		**15 µm**	**10 µm**
Flow Rate [μL /min]	5	5	10	5	33.5
Re_c	3.78	3.78	7.56	3.78	20
Re_p	0.07	0.30	0.60	0.67	0.8
l [μm]	18.6	19.95	20.55	24.35	34.70
y^*	0.23	0.23	0.23	0.19	0.27
U_p/U_{max}	0.77	0.71	0.69	0.67	0.68
U_{slip}/U_{max}	0.02	0.09	0.09	0.19	0.06
Ω_p, Lead [Hz]	634	577	1172	434	1403
Ω_p, Lag [Hz]	635	585	1193	435	1408
Ω_p, Equation 7.8 [Hz]	648	636	1255	476	1461
Max. Wall Shear [Pa]	20	29	61	66	48
Max. Particle Shear Force [Pa]	15	22	41	46	41

Figure 7.5 also supports the hypothesis that L_o/H scales as $1/Re_p$. In the numerical data of Figure 7.5c, the flow velocity U_{max} doubled at constant particle size while the time to equilibrium was reduced by a factor of four. Thus, if we assume that the time to equilibrium $t_o \propto f/U_{max}^2$, where f is an unknown parameter with units of diffusivity [m^2/s], and substitute $L_o \propto U_{max} t_o$, we arrive at $L_o \propto f/U_{max}$. For the conditions here of constant particle size, channel geometry, and fluid properties, the equilibrium ordering length scaled as $1/Re_p$.

Modeling and Particle Rotation

Particle interactions as functions of particle sizes are more complex and likely involve rotation rates. Figure 7.6 shows typical streamlines for 10 µm interacting particles, and Table 7.1 shows results for COMSOL simulations completed in this study. The table includes simulation results at Q = 5 µL/min for all three particle sizes, and Q = 10 µL/min for the 10 µm particles. In addition to values plotted in Figure 7.3, Table 7.1 includes additional quantities including slip velocities and rotation rates. Particle shear stresses up to 45 Pa are also reported to quantify

stress on biological samples. This is particularly relevant for biological cell cytometry and encapsulation applications. To provide context, one study found that red blood cell damage occurred only when surface shear stresses exceeded 425 Pa for 620 ms or longer[288].

For the 10 μm particle size, the rotation rate varied linearly with flow rate. This is intuitive, as the average shear rate U_{max}/h (where $h = H/2$), which initiates particle spin, also varies linearly with Q. Due to different slip velocities and shear rates associated with different y^* positions, the rotation rate did not vary linearly with particle size. Equation 7.8 presents an empirical expression for dimensionless rotation at equilibrium (zero net force and torques) for a finite-sized particle in linear shear flow[289].

$$\Omega_{p,eq}^{*} = \frac{\omega^*}{2}(1 - 0.0075\mathrm{Re}_{\omega}^{*})\left(1 - 0.062\mathrm{Re}_{\mathrm{p}}^{*\frac{1}{2}} - 0.001\mathrm{Re}_{\mathrm{p}}^{*}\right) \tag{7.8}$$

Quantities for the dimensionless fluid vorticity ω^*, particle angular velocity Ω_p^*, and alternative definition for particle Reynolds number $\mathrm{Re}_{\mathrm{p}}^{*}$ and shear rate Reynolds number Re_{ω}^{*} are presented below. The symbols ω_f and Ω_p represent the local fluid vorticity for an undisturbed velocity profile at $[y^*, U_\infty]$ and particle angular velocity, respectively.

$$\omega^* = \frac{\omega_f a}{U_{slip}} \tag{7.9}$$

$$\Omega_p^* = \frac{\Omega_p a}{U_{slip}} \tag{7.10}$$

$$\mathrm{Re}_{\mathrm{p}}^{*} = \frac{\rho U_{slip} a}{\mu} \tag{7.11}$$

$$\mathrm{Re}_{\omega}^{*} = \frac{\rho \omega_f a^2}{\mu} \tag{7.12}$$

This fit was extended from an analytical solution for creeping flow ($\Omega_{p,eq}^{*} = \frac{\omega^*}{2}$) to include finite values of $\mathrm{Re}_{\mathrm{p}}^{*}$ and Re_{ω}^{*}[289]. To calculate the rotation rate $\Omega_{p,eq}^{*}$, one needs to only estimate the

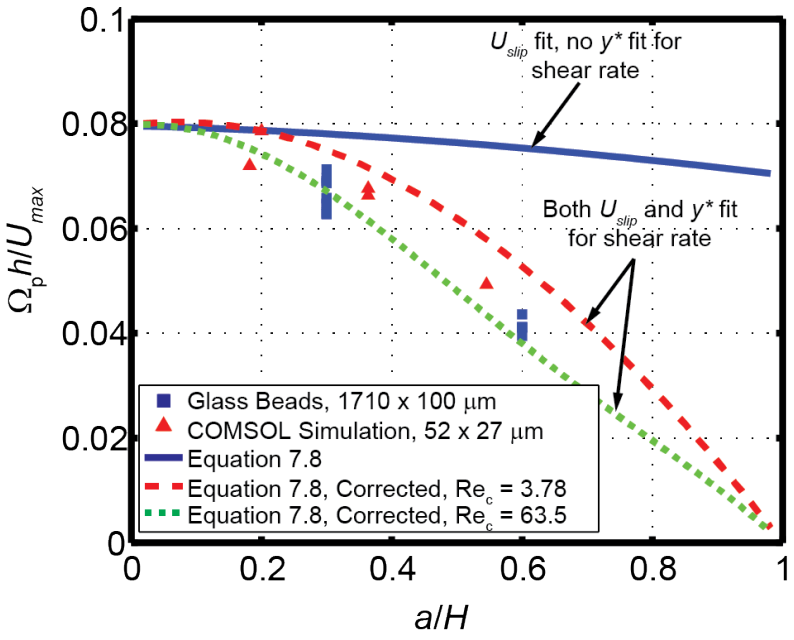

Figure 7.7. Predictive model for dimensionless rotation rate. The data points represent data from the present study and from data obtained in Chapter 6. The solid line represents the need for accurate local shear rate prediction and uses the average channel shear rate in Equation 7.9. The "corrected" plots use a fit for y^* versus a/H to obtain the shear rate from Equation 7.13. The Re_c values plotted using Equation 7.8 are arbitrary, and the range is intended to show the utility at a variety of conditions.

local fluid shear rate. The shear rate was obtained from single-phase 3D velocity profiles for cases where y^* was known. While Equation 7.8 was developed for linear shear flows and not the Poiseuille flows of the present study, this shear-rate based estimate for particle rotation provided a valuable design estimate of the rotation rate within 10% of those provided by the CFD model (Table 7.1).

Table 7.1 compares modeled results for equilibrium rotation with predicted values from and Equation 7.8. However, Equation 7.8 relied on the prior knowledge of the local shear rate at y^* and U_{slip}, both which of which were obtained through numerical modeling. It would be more useful to predict the rotation rate without computationally expensive solutions. Here, we fit the results for U_{slip}/U_{max} and y^* versus a/H using the data points in Table 7.1. The fit parameters are plotted in Appendix F and did not assume constant Re_c or Re_p. The fit values for U_{slip} were

plugged directly into Equations 7.9-7.11. We then converted our fit values for y^* using the local shear rate

$$\omega_f = U_{max}\frac{2y}{h^2} = 4\left(\frac{U_{max}}{h}\right)y^*. \tag{7.13}$$

Thus, the combinations of Equations 7.8-7.13, with curve fits from Table 7.1, provide an expression for the equilibrium rotation rate based only on the particle size, shortest channel dimension, and flow rate. Figure 7.7 plots the expressions against numerical data from this study, as well as experimental rotational data from Chapter 6. Despite stark differences in channel geometry, particle size, and fluid properties, the dimensionless rotation $\Omega_p h/U_{max}$ versus a/H compares well between the two datasets and the predicted values. While not shown, the plot of Figure 7.7 also compares well to results of a previous study[143] (Figure 2), which experimentally measured and numerically modeled rotations in a square channel.

7.4.2 Ordering in 40x31 Channel

Analysis of low aspect ratio ($W > H$) channels in conjunction provides additional insight into ordering. The ordering phenomenon is ultimately similar, but the flipped aspect ratio provides a perpendicular view to that of the previous section. While the z^* positions were not directly quantifiable, two staggered trains marked the presence of ordering downstream. The low aspect ratio channels, combined with the reference frame tracking, provided a distinction between the primary (short dimension) and the secondary (long dimension) ordering in rectangular channels. Figure 7.8 provides ordering statistics for 5 μm and 10 μm particles in the 40 μm wide by 31 μm tall channel. The inset in Figure 7.8a shows frames for 10 μm particle ordering at $Re_p = 0.78$, along with a plot of σ^*_{rel} (Equation 7.4) versus downstream position,

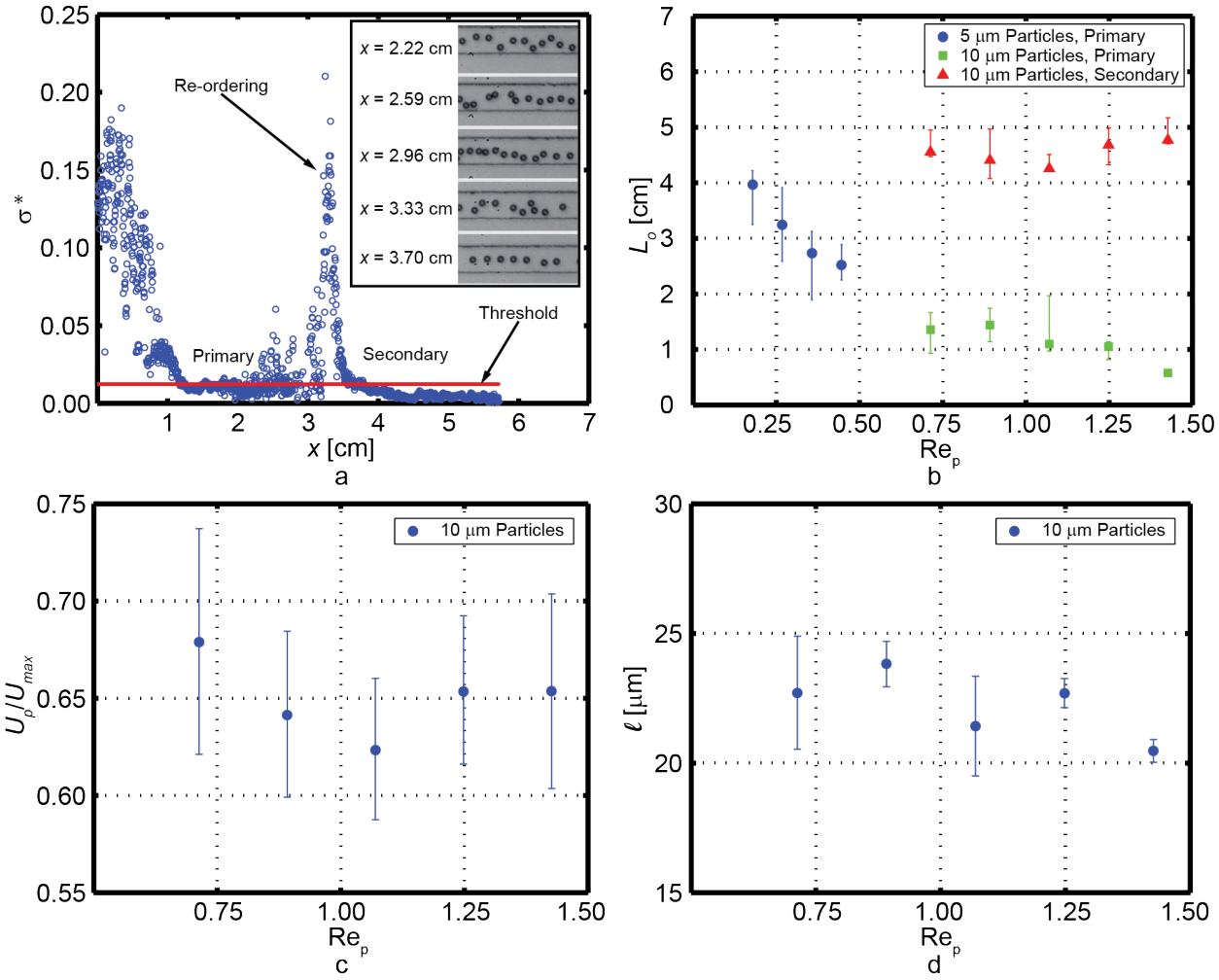

Figure 7.8. Dynamic tracking and equilibrium results for a 40x31 µm channel. (a) Particle velocity uniformity (Equation 7.4) versus downstream channel position. The inset shows primary focusing/ordering at x = 2.22 cm, where particles travelled at uniform velocity, but not in a single train. The particles reordered following migration toward the centerline at $y^* = 0$ (secondary focusing and ordering). (b) Ordering length L_o versus $\mathrm{Re_p}$ for 5 µm and 10 µm particles. Both steps of ordering are plotted (secondary ordering redefined by Equation 7.13). Note that the 5 µm particles never achieved full ordering along $y^* = 0$ for the flow rates tested. (c, d) Particle velocity (a) and center-to-center spacing (d) near the channel outlet for ordered 10 µm particles. For (b) and (c), each data point represents at least two independent trials. For (d), each data point represents at least two particle trains over at least five frames.

measured from the channel inlet. Primary ordering quickly occurred, but particles were not aligned in trains (x = 1.22 cm). However, the particles slowly migrated along the long channel dimension (secondary ordering) toward the centerline ($y^* = 0$). As they neared the centerline, the particles became crowded (x = 2.59 cm and 2.96 cm). This compressed train became unstable as

some particles quickly accelerated down the channel and others remained at the same velocity (x = 3.33 cm 3.33 cm). Finally, particles re-ordered into equally spaced trains further downstream.

This two-step ordering process was typical among experiments for the 40x31 μm device. The results of Figures 7.7a illustrate that particles are "competing" for the same space near the centerline. When the particles become too close together, reorganization occurs. Thus, particle concentration is a key parameter in ordering applications. While not systematically addressed in this study, the previous section noted the impact of particle concentration on ordering length.

Figure 7.8b plots ordering length L_o with distinctions between each of the two steps. Given the ability to visualize the "secondary" ordering with a low aspect ratio channel, we found that the average y^* position provided a more accurate depiction of "complete" ordering. We redefined completion of the secondary ordering, i.e. completion of ordering, as the point where the standard deviation of the dimensionless position y^* satisfies

$$\sigma_y^* \leq 4.0\%. \tag{7.13}$$

Again, we define the ordering length error such that the lower and upper error bounds to σ_y^* values of 5.0% and 3.0%, respectively. Additional errors in downstream channel position and scaling uncertainties have been incorporated into the error bars of Figure 7.8b. Note that for 5 μm particles, only primary ordering occurred within the 6 cm channel length. Again, as suggested for focusing length L_f[20], L_o/H scaled as $1/\mathrm{Re}_p$.

When comparing ordering in these low aspect ratio channels to that in high aspect ratio channels, one may ask why the multiple peaks for σ_{rel}^* not observed for high aspect ratio channels as they were in Figure 7.8a. While one possible explanation could be the slightly different ways in which the PDMS deforms in each of the two configurations, another plausible explanation relates to the inlet conditions. Figure 7.9 shows the typical inlet configuration for

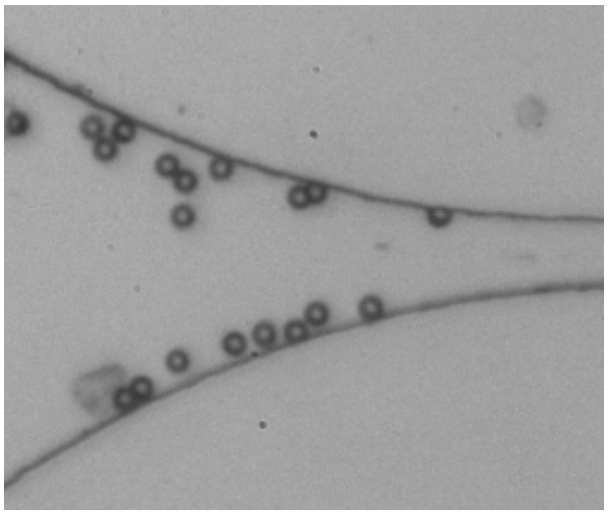

Figure 7.9. Typical particle flow distribution at the inlet. This distribution was similar for both the high aspect ratio and low aspect ratio designs. Due to the standard microfluidic inlet design, the 10 μm particles tended to "spill" into the channel along the sides. Thus, particles were biased toward the final ordering positions for high aspect ratio channels. Conversely, particles were furthest from their ordering positions for low aspect ratio channels.

both the 40x31 and 27x52 channels, respectively. In both cases, the particles flowed radially from the inlet port. Most of the particles flow into the plenum and then are redirected around the plenum sides such that they "spilled" into the channel along the channel sides. Thus, in a high aspect ratio ($H > W$) channel, the particles are already biased toward the primary focusing/ordering position. However, in the 40x31 channel, the particles start on the sides of the channel furthest from their final ordering positions. Here, the shear gradients for ordering were weaker, slowing migration velocity.

7.4.3 Biological Cell Ordering in 24x36 Channel

As an example of biological cell applications, ordering of algal cells using the motorized stage is shown in Figure 7.10. Here, the tracking stage allowed for a 45-fold time increase in which the cells were visible in the field of view. Figure 7.10b shows the relative x and y spacing

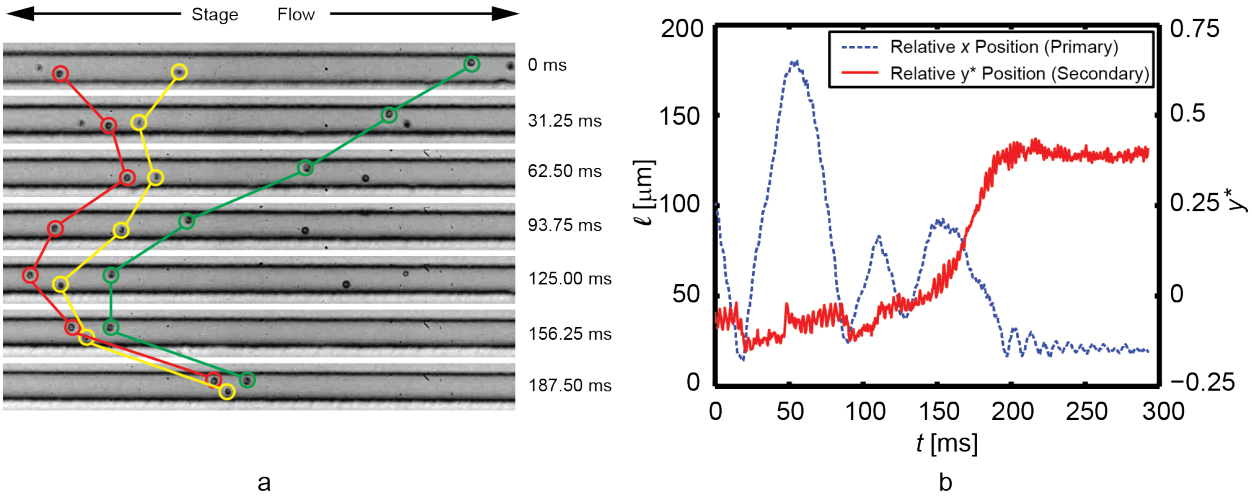

Figure 7.10. Ovoid algae cell ordering in a 24x36 μm channel. (a) The trailing cell, "Cell 1", interacted with Cell 2 first. Part (b) shows the relative streamwise and lateral spacing between Cell 1 and Cell 2. While on the same lateral side of the channel, the cells "bounce" off each other. After the interaction induces Cell 1 to change sides, the spacing exhibits damped oscillation to an equilibrium spacing. Part (a) also shows the leading Cell 3 leave its neighboring cell to join the Cell 1 and 2 pair. The video more clearly shows the cell interactions, orientations, rotations, and *z* position changes (based on focus of the cell within the frame).

between the two cells, "Cell 1" and "Cell 2". Initially, both were on the same lateral side of the channel. As they began to interact, Cell 1 seemed to "bounce" off Cell 2 while remaining on the same side of the channel. As they became closer in proximity, Cell 1 migrated to the opposite side of the channel due to the interaction of the velocity profiles induced by each cell. While we cannot confirm this quantitatively, the video appears to show changes (due to focus of the cells in the frame) in the *z* position (into the screen) of both cells, as well as fluctuating rotational axes of the ellipsoidal cells.

During the interaction between Cells 1 and 2, a third cell, "Cell 3", interacted with the original cell pair on the leading side of the flow. The three cells equilibrated to an alternate-side ordering trio, similar to that of previous work[20,24]. The important thing to note here is that cells and particles interacting on the same lateral side of the channel can migrate between focusing positions when forming trains. While we cannot directly confirm the vertical spacing in

the channel, we hypothesize that the cells migrate around the annulus of the channel as opposed to taking direct paths between ordering positions.

7.5 Conclusions

Here, we have utilized the combination of experiments and numerical modeling to study the effect of flow rate and particle size on ordering behavior in two rectangular microfluidic channel geometries. We have revealed new insights into microfluidic focusing and ordering of particles in small, but finite, Reynolds number flows. Using reference frame tracking, we have tracked individual particles, pairs, and multiple particle trains for long periods, often reaching fiftyfold increases in particle observation time within the field of view. The results have shown similar particle interaction behaviors between experimental data and CFD results. Coupling the two has led to quantifiable dynamic particle interactions, ordering lengths, and force scaling, as well as equilibrium spacing, velocity, and rotation rates.

Key results include:

1. Ordering length scaled as $1/Re_p$. For the applied devices tested, ordering of 5 μm particles was possible only at high flow rates. While not as consequential for cytometry applications, this is important for ordered encapsulation applications where lower Weber and Capillary numbers are required to prevent jetting[259].
2. In the 27x52 device, the equilibrium particle spacing (center-to-center) showed only a slight dependence on particle size. Additionally, the surface-to-surface spacing was constant for all particle sizes tested.

3. Equilibrium particle spacing decreased with decreasing channel dimensions. This relationship was shown numerically at constant maximum shear rate U_{max}/h for the two dimensions (27x52 and 50x50) modeled. This relationship was also observed in deformable PDMS devices. As the channel deformation decreased downstream, the particle spacing also decreased.
4. Interparticle forces scaled as the particle slip velocity squared (U_{slip}^2) and thus were proportional to Re_c^2 for constant particle size.
5. Particle shear stresses were numerically quantified using modeling. For flow rates and dimensions used in previous studies[24,237], particle and cell surface shear stresses were calculated as high as 40 Pa. The combination of stress calculation and time within the device provides valuable information when correlating to cell expression and viability following ordering.
6. Equilibrium particle rotations were predicted to within 10% using an empirical equation (Equation 7.8) expanded from an analytical solution for linear shear flow. This expression was expanded using modeling fits for y^* and U_{slip} to provide dimensionless rotation predictions based on only the particle size, shortest channel dimension, and flow rate.
7. We have documented the presence of two distinct focusing and ordering stages using discrete particle trajectories.
8. Particles and ovoid cells can migrate across focusing positions to achieve staggered ordering trains.

While we have systematically focused here on particle size, channel geometry, and flow rate (Re_c and Re_p), we have also found that particle concentration, channel deformability, and inlet conditions play additional roles in the development of ordered trains. Given its high utility, our reference-frame tracking concept is well suited for performing additional studies to fully address a wide range of parameters for many applied designs in cytometry, ordered encapsulation, and other inertial microfluidic applications.

Chapter 8

Conclusions

In total, this work has investigated microfluidic devices on two fronts: applications and fundamentals. Droplet microfluidics provides a variety of benefits in cell signal amplification and cell isolation. By trapping cells or cell groups within droplets, millions of parallel bioreactors can be exploited to perform simultaneous experiments to test drug efficacy, perform diagnostic tests, and highlight rare cells and interactions. However, controlling the number of cells in each droplet has limited the applications of cell-laden droplets.

Keeping in mind downstream biological applications, this work has presented two designs for single and multiple-cell co-encapsulation by merging droplet microfluidics with inertial microfluidics. In the first device, a single microfluidic "ordering" channel improved microparticle encapsulation efficiency at 6.1 kHz to 79.5%, compared to a random encapsulation efficiency of 36.7%. The same device encapsulated two and only two particles in droplets at 3.8 kHz with 71.5% efficiency, compared to 26.7% in random paired encapsulation.

This dissertation also presents an applied device that improves on the first design by incorporating two distinct upstream ordering channels. This allowed for the encapsulation of two distinct cell types to pair dissimilar cells in isolated droplets. While the theoretical probability of a droplet containing one cell of each type for 13.5%, in most practical dilutions useful for fluorescence activated cell sorting (FACS), the number is limited to around 5%. This work demonstrated paired co-encapsulation of idealized microspheres at 64% efficiency and 5.8 kHz. For living cells, the device was used to pair opposite-type algal gametes in droplets at 29%

efficiency. Subsequently, mating between the gametes occurred. Following zygospore maturation, the emulsion was broken after 17 days on agar, and vegetative cell mitosis resumed. This work represented significant achievements in controlling isolated cell interactions, as well as demonstrating long-term survival in droplets without refreshing culture media.

To improve on controlled encapsulation in applied devices, this dissertation also investigated the effect of flow rate, particle size, and channel geometry in the upstream channels. Since ordering is key to achieving efficient encapsulation and is useful in flow cytometry, a moving reference frame microscope stage was constructed to track ordering along the entire length. The apparatus allowed tracking of particles moving on the order of 1 m/s for factors of 50 times longer than stationary stages. Providing more quantifiable results, numerical models were coupled with experimental results. The particle focusing, interactions, equilibrium positions, and ordering lengths presented here represent unique understanding and insight into the design of applied devices. Qualitatively, we have documented the presence of distinct ordering stages, the first where particles migrated to short channel dimensions, and the second where particles re-arranged to form trains centered along the wider channel dimension. Quantitatively, ordering lengths scaled as $1/Re_p$, interparticle forces scaled as Re_c^2 for constant particle size, typical cell shear stresses for the devices used in the applied work were on the order of 40 Pa, and particle rotations were found to be adequately estimated by empirical equations derived from linear shear flow.

Both the fundamental and applied work represent advances toward more robust, parallel diagnostic tools. On the fundamental side, the results have provided key insight, but also open a wide range of future questions, into the fluid mechanics of inertial focusing and ordering. On the applied side, the paired cell co-encapsulation device has the potential to be used in a variety of

studies where cell-cell interactions are needed. Such examples include studies in paired cell fusion, target-receptor interactions, and immune response. In total, the studies encapsulate a range of accomplishments in applied bioMEMS devices, additional understanding of two-phase particulate flows, and tools for further studies in applied and fundamental microfluidics.

Appendix A

Sample Droplet Encapsulation Device Fabrication and Experimental Protocol

The protocols in this section describe the materials and equipment utilized specifically to obtain the experimental results presented in Chapter 4. This protocol has been previously published by the author[237]. Note that alternative suppliers for chemicals and equipment may be utilized.

1. Device Fabrication and Soft Lithography

Standard soft lithography techniques, a number of which have been featured in previous JOVE articles, were used for creating polydimethylsiloxane (PDMS) microchannel networks bonded to glass substrates. Aside from master replica mold fabrication by SU-8 photolithography, the processes may be performed outside a clean room or clean hood; however, dust and particulates should still be minimized to achieve consistent results.

1. Design a micro-channel pattern as shown in **Figure 4.1** in AutoCAD (AutoDesk Inc.). Employ a third party manufacturer (Fineline Imaging Inc.) to print a high resolution (50,000 dpi) transparency mask on Mylar film or quartz where channels are transparent on a dark background.
2. Create a silicon and SU-8 photoresist master for replica molding. Briefly, spin SU-8 2050 (MicroChem) negative photoresist with manufacturer's recommended rpm on a spin-coater to create a 52 μm thick layer on a clean 7.5 cm or 10 cm silicon wafer. After soft bake, edge bead removal, UV exposure through a contact mask, post-exposure bake, development, and flood exposure, measure the actual thickness of the SU-8 layer using a Dektak profilometer (Veeco). Tape the master mold onto the bottom of a 4" or 5" Petri dish to prepare for PDMS replica molding.
3. Mix PDMS elastomer base with elastomer curing agent (Dow Corning) in a 10:1 ratio w/w base to curing agent. Pour well-mixed PDMS precursor onto the silicon master to create a 2-3 mm final thickness layer. A mixture of 20 g elastomer base with 2 g curing agent is sufficient to cover a 4" diameter surface.
4. Place the master mold and PDMS in vacuum desiccator (Jencons) to de-gas the uncured PDMS. Using a pressure regulator (Cole Parmer), slowly decrease the chamber gage pressure from 0" Hg to -27" Hg over 20 minutes to avoid excessive foaming. Leave device in vacuum chamber at -27" Hg for 30 minutes or until air bubbles disappear.
5. Release vacuum and move master mold and PDMS to a 65 °C oven (Thermo Scientific) for a minimum of four hours. The device may be left in the oven overnight to improve curing.
6. Remove the device from oven and allow to cool. Carefully cut PDMS around circular wafer using a precision knife and peel out PDMS. Cut out device outline as shown in **Figure 4.1** with a scalpel.
7. Punch fluidic ports (three per device) in the three round regions shown in **Figure 4.1** using a biopsy punch. For this device, use a 0.75 mm outer diameter punch (Harris).

8. Adhere scotch tape to the patterned side of the PDMS and peel to remove any dust. As a cost-saving but viable alternative to conventional oxygen plasma apparatuses, plasma treat the patterned side of the PDMS and a clean 3" x 1" glass microscope slide using a hand-held laboratory corona treater (Electro-Technic Products Inc.).[23] Note that this device should be used in a fume hood or well-ventilated area due to ozone discharge, and all watches and cell phones should be kept at least ten feet away. Adjust the corona discharge to attain a stable corona with minimal sparking. Slowly wave the electrode about 1/4" above each surface for around 20 seconds and then immediately bring the treated surfaces into contact to form a strong permanent bond before the PDMS surfaces return to their native state.
9. Place the device on a metal plate, place in a cool oven, set the oven to 120 °C, and bake overnight to complete bonding and to return the PDMS to its original hydrophobic state. During this high temperature baking, the glass surface of the channel will also be rendered hydrophobic due to deposition of a thin hydrophobic layer onto the glass. Alternatively, hydrophobic coatings such as Aquapel (PPG Industries) may be injected into the fluidic ports using a 1 mL syringe and a syringe needle. Carefully but firmly inject the Aquapel followed by purging air into the fluidic ports without breaking the PDMS to glass bond. Aggressively repeat the air purge on all inlet and outlet ports while wiping off any excess Aquapel in order to avoid any deposits that may clog the channels upon drying.

2. Sample Preparation

1. Prepare a cell culture according to established procedures for your chosen cell type. For the particular device used in this study, 8-15 μm particles or cells should adequately order for encapsulation. Smaller or larger cell types may require changing the dimensions of the focusing channel to achieve adequate Re_p. For the method demonstration results shown in this paper, 9.9 μm polystyrene microspheres (G1000, Thermo Scientific) are utilized as cell surrogates.
2. Prepare the aqueous particle or cell suspension through gentle mixing. When using cells or polystyrene particles, concentration control is essential (see **Figure 4.4**) to achieve ideal ordered encapsulation. Using previous data as a guide, calculate the desired cell or particle concentration based on the ordered train spacing and micro-channel size as: one cell or particle per expected longitudinal train spacing times the focusing channel cross-sectional area. If the stock concentration (1% w/w) is inadequate, increase the concentration (here to 1.5% w/w) by gently centrifuging the stock sample, removing supernatant liquid, and re-suspending the particles by vortex mixing, or gentler mixing when using cells. Prepare an adequate volume to account for desired collection volume and for run time associated with flow tuning.
3. Both cells and polystyrene particles have a specific gravity greater than one. Although not demonstrated in this protocol, for long-term experiments lasting on the order of many minutes to hours, buoyancy match the solution by adding a solute such as $CaCl_2$ for particles or OptiPrep (Sigma-Aldrich) for cells.
4. Prepare a 10 mL sample of the continuous fluorocarbon oil phase by mixing the fluorocarbon oil FC-40 (3M) and PFPE-PEG block copolymer surfactant (2.5% w/w) (RainDance Technologies) in a 15 mL centrifuge tube. Alternatively, light mineral oil (PTI Process Chemicals) can be utilized with ABIL-EM 90 surfactant (2.5% w/w) (Evonik Goldschmidt Corporation).

3. Experimental Setup

1. Power on the inverted optical microscope (Axio Observer, Zeiss) and high-speed camera (Phantom V310, Vision Research). Focus and inspect the channels for clogs and debris by either

manually moving the device or by using a motorized microscope stage. Some small debris may be pushed out when liquid flows through. For large debris or obvious clogs, select another channel on the device as debris in the focusing channel can degrade ordering quality significantly. Note that clogs can often be removed under flow by pressing firmly on the PDMS surface above the affected region with blunt tweezers.

2. Cut three lengths of PVC tubing (0.01" ID/0.03" OD, Tygon) for the aqueous inlet, oil inlet, and emulsion outlet. To minimize dead volume, cut just enough tubing to reach from the syringe pumps to the microscope stage. Cut tubing ends at a 45° angle to facilitate insertion into fluidic ports.
3. Use tweezers to press fit the tube ends into the fluidic ports punched in Step 1 and then press fit two 30 gauge blunt-tip stainless steel syringe needles (SmallParts) into the free ends of the respective aqueous and oil inlet tubes (no adhesive necessary). Place the outlet tubing into a waste reservoir. This tube will later be moved into a collection reservoir.
4. Move the device and attached tubing to the microscope stage, align, and focus on the device nozzle using an available objective (20x was used for this experiment). Adjust for Kohler illumination and other microscope settings as required for optimal recording.
5. Fill a 1 mL syringe (BD) with the well-mixed aqueous phase and a 3 mL syringe (BD) with the oil phase solution prepared in Step 2. Note that any syringes of any volume may be used and should be carefully selected depending on the desired run times and minimization of any pulsatility. Tilt one syringe vertically and flick to move air bubbles to the syringe outlet. Slowly depress plunger enough to push the air to the syringe tip. Holding the syringe vertically, connect the syringes to the respective syringe needle already attached to the device in Step 3.3. Depress plunger to force the air through the syringe needle dead volume until fluid is pushed through the tubing almost to the device. Securely mount the syringe to a syringe pump (Nexus 3000, Chemyx) and engage the plunger block. Repeat connections for the second syringe and mount to a second syringe pump.
6. Power on each syringe pump and program using the pump manufacturer's protocols. Set the initial flow rates to Q_{oil} = 50 μL/min and Q_{aq} = 5 μL/min for the oil phase and aqueous phase, respectively. Start the pumps.
7. Wait for each fluid to enter the device and fill the channels, pushing out remaining dead air. This may take several minutes. If there is a large amount of air in the inlet tubing, temporarily increase each flow rate until the air is expelled. Do not increase the flow rates so high that large pressures occur in the channel, potentially leading to PDMS-to-glass bond failure.
8. Using the initial flow rates, observe the formation of drops at the nozzle (results shown here: 20x magnification, frame rate 21,005 fps, exposure 3 μs). Reduce the camera field of view to only the nozzle to maximize the frame rate and reduce memory requirements if possible. Capture sample videos and confirm that the sampling rate is adequate to avoid aliasing.
9. To avoid jetting (see **Figure 4.2**), start with low aqueous flow rates. Slowly increase the aqueous flow rate to observe ordering of particles in the long aqueous solution channel as the flow rate increases.
10. If the particle concentration is too low to provide trains with relatively few "missing" particles and the sample was not buoyancy matched, physically tilt the syringe pump toward the syringe outlet to provide gradual settling of particles toward the syringe outlet. This method is demonstrated in the video protocol. Periodically rotating the syringe along its axis may also reduce undesired settling.
11. Once adequate ordering occurs, adjust the oil flow rate to tune the generation frequency and size of drops. The mean drop volume may be calculated using the aqueous flow rate divided by the

drop generation frequency as measured by video capture. Iteratively adjust both flow rates to achieve desired encapsulation rates and drop volumes.

12. Once stable ordered encapsulation is confirmed, move the outlet tubing from the waste reservoir into a collection reservoir or feed it into another device for subsequent testing.
13. Determine the collection time based on desired number of droplets and the calculated generation frequency.
14. Record the fraction of drops containing 0, 1, 2,…, N particles to quantify efficiency using either drop generation video results or by pipetting a sample of collected emulsion for inspection.

Appendix B

Droplet Encapsulation Simulator, MATLAB Code

(Previously published as supplemental material for [237])

```
% Droplet Encapsulation Simulator
% Jon F Edd
% Todd P Lagus
% Vanderbilt University
% February 14, 2012
% This MATLAB script simulates encapsulation of particles in a set number
% of drops (N_drops) by calculating downstream positions of a particle and
% an associated drop.  The simulation models, effectively, a very long
% channel with a volume equal to the total volume of aqueous fluid
% dispensed (N_drops times the average drop volume). The channel length is
% split into sections of an effective drop length (drop volume divided by
% the aqueous flow channel cross section). If the particle downstream
% position intersects with a drop downstream position limits, then that
% particle is assigned to that particular drop. The downstream particle and
% drop positions are assigned using average particle spacing and drop
% volumes, each with offsets determined by the respective standard
% deviation multiplied by a random number (randn) to simulate a
% random experiment. Polydispersity in drop size is accounted for in the
% standard deviation of the drop volume, altering the effective lengths of
% the drop sections, with monodisperse drops exhibiting low standard
% deviations. The effect of ordering is included with the standard
% deviation of particle spacing. For high degrees of ordering, the standard
% deviation will be small, and for no ordering, the standard deviation will
% be at its largest. For monodisperse drops with high ordering, both the
% particles and drops will be spaced at regular intervals, indicating more
% controlled ordering. Note that very high standard deviations may cause
% problems if regions overlap. The simulation counts the number of
% particles in each drop and provides a histogram matrix for the number of
% particles, as well as a plot of the percentage of drops with 1,2,3, … Nk
% particles.

% Inputs:
N_drops=1e3; % number of drops (drop sample size)
channel_height=52; %height in microns
channel_width=27; %width in microns
dx_part_avg=17.5; % average particle spacing (observed, in microns)
dx_part_std=5; % standard deviation of the particle spacing (degree of ordering)
drop_vol_avg=24.39*1000; % average drop volume, cubic micron (shown here -
picoliters*1000)
drop_vol_std=5*1000; % standard deviation of drop volume, cubic micron (shown here -
picoliters*1000) (degree of monodispersity)

% Calculate effective drop diameter
dx_drop_avg=drop_vol_avg/(channel_height*channel_width); % average effective droplet
spacing
dx_drop_std=drop_vol_std/(channel_height*channel_width); % standard deviation of the
effective droplet spacing

Nk=zeros(100,1); % histogram counter for number of particles per drop
x_part=0; x_drop=0; m=0; % initialize x_distance down channel
```

```
h=waitbar(0,'Encapsulating particles...');
for i=1:N_drops
    x_drop=x_drop+(dx_drop_avg+dx_drop_std*randn); % generate particle x_position
    k=0; % Start the count of particles for the upcoming drop
    while x_part<x_drop %generate drop x_position
        k=k+1;
        x_part=x_part+(dx_part_avg+dx_part_std*randn);
    end
    Nk(k+1)=Nk(k+1)+1;
    m=m+1;
    if m>(N_drops/100)
        waitbar(i/N_drops,h);
        m=0;
    end
end
close(h);

Pk=Nk/sum(Nk);
figure; bar(0:(length(Pk)-1),Pk);
```

Appendix C

MATLAB Particle and Cell Tracking Code

The following represents a sample of code for processing video pre-processed in ImageJ[290]. Functions for the stage velocity correlation (dftregistration.m) and particle tracking (track.m) have been customized using existing codes from [287] and [279], respectively. To conserve space, the two referenced algorithms have not been explicitly included here, but online locations of these codes are available in the cited references.

```
% Tracking Main
% PDMS channel image processing using flat channel (no tilt) with or without
% a moving stage
% NOTE: ROTATE VIDEO SUCH THAT CHANNEL DIRECTION IS HORIZONTAL AND FLOW IS
% LEFT TO RIGHT ON SCREEN. CROP ANY ADDITIONAL NON-CHANNEL SPACE AS NEEDED.
% KEEP ONE ORIGINAL FILE IN AVI FORMAT, AND THEN PERFORM A BANDPASS FILTER
% (RESET MIN AND MAX PIXEL SIZE FILTERS AS NEEDED) WITH HORIZONTAL STRIPE
% SUPRESSION AND SAVE. THE TWO FILES ARE INTERACTIVELY SELECTED BY THE USER.
% TPL 7/31/12
 %% Clear Variables
    clear all
    close all

%% Initialize Global Variables
    global num;
    global numframes;
    global timestep;

%% GUI file selection
numfiles=1; %number of file pairs
% the first file in the pair should be an unprocessed image for
% determining the channel width in each frame
% The second file should be a bandpass filtered image with horizontal
% stripe suppression (assuming left to right flow orientation)
for i=1:numfiles
    [filename,pathname] = uigetfile('*.avi',strcat('Enter Filename of Cropped Original
Image Stack'));
    fullname=fullfile(pathname, filename);
    fnames{i,1}=fullname;
    [filename,pathname] = uigetfile('*.avi',strcat('Enter Filename of Cropped Bandpass
Filtered Image Stack'));
    fullname=fullfile(pathname, filename);
    fnames{i,2}=fullname;
end
    mov1=VideoReader(fnames{1,1}); %original movie
    mov2=VideoReader(fnames{1,2}); %preprocessed movie

%% Inputs and data
    numframes=mov1.NumberOfFrames;
    startframe=1;
% User 'inputs'
    framerate=input(strcat('Frame Rate (frames/s):'));
    flowrate=input(strcat('Flow Rate (microliters/min):'));
    channelheight=input(strcat('Channel Height (microns):'));
    channelwidth=input(strcat('Channel Width (this will also be measured using video)
(microns):'));
```

```
    diam=10; %nominal particle size, um
    scale=1.026; %um/pixel
    rho=1000; %kg/m3, fluid density
    mu=0.00112; %N-s/m2
    channellength=61739; %um
    stagevelmax_x=channellength/(numframes/framerate); %um/s (establish a "guess"
value for stage velocity, which will be measured
% Calculations based on inputs
    timestep=1/framerate;
% est. velocity for downstream displacement of particles from frame to
% frame for threshold calculation
% Note that pdisp is very important in selecting particles
    Axsec=channelheight*channelwidth; %um^2 (estimated)
    u_mean=(flowrate*1e9*(1/60))/Axsec; %um/s
    u_max=1.5*u_mean; %um/s (estimated)
    pdisp=1.25*u_max*timestep*(1/scale); %particle displacement (absolute) in
pixels/frame
% Create time and frame vectors
    t=(0:timestep:(numframes-1)*timestep)';
    f=(1:1:numframes)';

%% Track Wall Locations
wall_threshold=input(strcat('Select Wall Threshold:'));
x_wallp=zeros(1,2);
y_wallp=zeros(1,2);
H=waitbar(0,'Obtaining Wall Locations');
samples=4; %even # (2,4,6,8) of wall samples to take for stage velocity
pixel_width=channelwidth/scale; %nominal channel width for guess value
for frame=startframe:numframes
    %read frame
    f_orig = read(mov1, frame);
    f_orig = rgb2gray(f_orig);
    %frame %diagnostic output
    % Measure channel dimensions in pixels
    [x_wall(frame,:),
y_wall(frame,:)]=channelwidthmain_min2(f_orig,frame,wall_threshold,x_wallp,y_wallp,pix
el_width); %calculate channel dimensions for frame
    if abs(y_wall(frame,2)-y_wall(frame,1))<pixel_width/2
        y_wall(frame,:)=y_wall(frame-1,:);
        x_wall(frame,:)=x_wall(frame-1,:);
    end
    waitbar(frame/(numframes),H);
    x_wallp=x_wall(frame,:);
    y_wallp=y_wall(frame,:);
end
close(H);

%% Smooth, scale, and calculate channel width to eliminate pixel noise
smooth_region=10;
for i=1:size(y_wall,2)
    channel_wall_smooth(:,i)=smooth(y_wall(:,i),smooth_region);
end
channel_width=(channel_wall_smooth(:,2)-channel_wall_smooth(:,1))*scale;
channel_wall_scaled=channel_wall_smooth*scale; %average channel wall coordinates in
frame

%% Z-projection to find background
f_background=(zeros(mov1.Height,mov1.Width));
count=1; %keep count for running weighted average
H=waitbar(0,'Z-projecting');
for frame=startframe:numframes
    f_preprocess = read(mov2, frame);
    f_preprocess = rgb2gray(f_preprocess);
```

```
    f_background = ((count-1)*f_background+(double(f_preprocess)))/count;
    count=count+1;
    waitbar(frame/(numframes),H);
end
f_background=uint8(f_background);
close(H);

%% Centroid Locations using background subtraction
num=1; %start particle counter at 1
wall_threshold=20; %intensity threshold for wall
stagedisp=zeros(numframes,2);
part_threshold=130; %intensity threshold for particles
ecc_threshold=0.75; %eccentricity threshold for particles

H=waitbar(0,'Subtracting Background');
writerObj1 = VideoWriter('backgound_subtract_video.avi'); %diagnostic
writerObj2 = VideoWriter('binary_video.avi'); %diagnostic output video
open(writerObj1);
open(writerObj2);
crop_tol=0; %for stage motion, crop this value in from the wall
for frame=startframe:numframes
    y_max=round(channel_wall_smooth(frame,2)); % wall coordinates
    y_min=floor(channel_wall_smooth(frame,1)); % wall coordinates
    if frame == startframe
        f_preprocess = read(mov2, frame);
        f_preprocess = rgb2gray(f_preprocess);
        f_subtract = f_background-f_preprocess;
        f_subtract = imadjust(f_subtract); %normalize histogram
        f_subtractw = f_subtract;
        f_subtractw(y_min+crop_tol:y_max-crop_tol,:)=0;
    else
        f_subtract = f_subtractf;
        f_subtractw = f_subtractfw;
    end
    if frame < numframes
        f_preprocessf = read(mov2, frame+1);
        f_preprocessf = rgb2gray(f_preprocessf);
        f_subtractf = f_background-f_preprocessf;
        f_subtractf = imadjust(f_subtractf); %normalize histogram
        f_subtractfw = f_subtractf;
        f_subtractfw(y_min+crop_tol:y_max-crop_tol,:)=0;
    end
    % Wall processing for stage tracking
    f1_binary=im2bw(f_subtractw,wall_threshold/255); %convert binary
    f2_binary=im2bw(f_subtractfw,wall_threshold/255); %convert binary
    f1_binary=bwareaopen(f1_binary, 25); %remove noise
    f2_binary=bwareaopen(f2_binary, 25); %remove noise

    % Call wall tracking correlation
    [output g] = dftregistration(fft2(f1_binary),fft2(f2_binary),100);
    stagedisp(frame,1)=output(1,4); %x_shift, pixels
    stagedisp(frame,2)=output(1,3); %y shift, pixels

    % Call particle locating function
[C{frame,1},f_binary]=centroidmain(f_subtract,frame,part_threshold,ecc_threshold,y_min
,y_max);

    % write video for processed frames
    writeVideo(writerObj1,f_subtract);
    f_binary=uint8(f_binary*255); %convert binary frames to avi file
    writeVideo(writerObj2,f_binary);
    waitbar(frame/(numframes),H);
end
```

```
close(writerObj1);
close(writerObj2);
close(H)
save('loopone.mat') %save initial data

%% Smooth, stage tracking data
smooth_region=10;
% filter out nonsensical data
lower_limit=stagevelmax_x*(1/scale)*(1/framerate)*.95;
upper_limit=stagevelmax_x*(1/scale)*(1/framerate)*1.15;
stagedisp(numframes,:)=stagedisp(numframes-1,:);
for frame=startframe+1:numframes
    if stagedisp(frame,1)<lower_limit || stagedisp(frame,1)>upper_limit ||
abs(stagedisp(frame,2))>1
       stagedisp(frame,:)=stagedisp(frame-1,:);
    end
end

for i=1:size(stagedisp,2)
stagedisp_smoothed(:,i)=smooth(stagedisp(1:size(stagedisp,1),i),smooth_region,'rloess'
);
end
stagedisp_scaled=stagedisp_smoothed*scale;
stagevel=stagedisp_scaled./timestep;

%% Stage acceleration (forward difference)
stageacc=diff(stagevel);
stageacc(numframes,:)=stageacc(numframes-1,:);

%%  convert centroid cell array to number array
    for frame=startframe:numframes
        Ccorr1{frame,1}=cell2mat(C{frame});
    end
    Ccorr2=cell2mat(Ccorr1);
    % delete any zero value rows
    Ccorr2(find(Ccorr2(:,1)==0),:)=[];

%% Call particle counting function - Based on relative reference frame
    param.mem=1; %maximum time steps for a "lost" particle
    param.good=3; %min frames a particle must exist to be included
    param.dim=2; %first two cols of Ccorr2 represent centroid data
    param.quiet=0; %set to 1 to turn off output text
    pdisp_corr=1*(pdisp-min(stagevel(:,1))*(1/scale)*timestep);
    results=track(Ccorr2,pdisp_corr,param); %2nd input= maxpixel displacement

%% Replace all non-values with NaNs and populate position matrices
   unique=max(results(:,11)); %read number of unique tracked particles
   Xmat=NaN(unique,numframes);
   Ymat=Xmat;pixel_intensity=Ymat;eccentricity=Ymat;
   H=waitbar(0,'Arranging Tracking Data');
   % Matrix values at row = particle number, column = frame
   for part=1:size(results,1)
       Xmat(results(part,11),results(part,10))=results(part,1);
       Ymat(results(part,11),results(part,10))=results(part,2);
       pixel_intensity(results(part,11),results(part,10))=results(part,8);
       eccentricity(results(part,11),results(part,10))=results(part,6);
       area(results(part,11),results(part,10))=results(part,5);
       orientation(results(part,11),results(part,10))=results(part,7);
       waitbar(part/(size(results,1)),H);
   end
   close(H);

%% scale values for independent particle matrix
```

```
    Xmat_dim=Xmat*scale; %convert x position to um
    Ymat_dim=Ymat*scale; %convert y position to um

% Perform matrix operations to calculate forward, central, and backward time %
differences for velocity and acceleration
%%%%%%%%%%%%%%%%%%%%%%%%%%%%%%%%%%%%%%%%%%%%%%%%%%%%%%%%%%%%%%%%%%%%%%%%%%%%
% Channel width function %

function [x_w,y_w]=channelwidthmain_min2(frame1,frame,thresh,x_wp,y_wp,p_w);
%Todd Lagus
%Channel width measurement using minimum pixel values for finding the focused %wall
%location. This code assumes that the streamwise direction is vertical in the %image.
Create two images (one for left wall, one for right wall) and
%find the minima and location in each.

global numframes
%% Find Minimum and maximum pixel values
xwidth=size(frame1,2);
yheight=size(frame1,1);

% sobel edge filter on original frame
filt1=fspecial('average',[1,500]);
frame1_filt=imfilter(frame1,filt1,'replicate');

%% Thresholding
channel=im2bw(frame1,thresh/255);
%imshow(channel)

%% Remove Noise
channel=1-channel;
channel=bwareaopen(channel, 200); %removes objects less than pixel area
channel=1-channel;
%imshow(channel)

%% Find ballpark wall coordinate

x_w(1,1:2)=round(xwidth/2);
center=channel(:,x_w(1,1));
if isempty(find(center==0,1,'first'))==1 || (abs(find(center==0,1,'first')-
find(center==0,1,'last'))<(p_w/2))
    x_w=x_wp;
    y_w=y_wp;
else
    y_w(1,1)=find(center==0,1,'first');
    y_w(1,2)=find(center==0,1,'last');
end

%% Crop to ROI
y_tol=10;
framecrop_top=[1 max(y_w(1,1)-y_tol,1) xwidth y_tol*2];
framecrop_bottom=[1 max(y_w(1,2)-y_tol,1) xwidth y_tol*2];
filt2=(fspecial('prewitt'));

frame2_filt=imfilter(frame1_filt,filt2,'replicate');
filt3=fspecial('average',[3,xwidth]);
frame3_filt=imfilter(frame1_filt,filt3,'replicate');
%frame3_filt=255-frame3_filt;
frame_top=imcrop(frame3_filt,framecrop_top);
frame_bottom=imcrop(frame3_filt,framecrop_bottom);

%% Find wall coordinate
[min_top,y_top]=min(min(frame_top(:,x_w(1,1)),[],2));
[min_bottom,y_bottom]=min(min(frame_bottom(:,x_w(1,2)),[],2));
```

```
y_top=y_top+(framecrop_top(1,2)-1);
y_bottom=y_bottom+(framecrop_bottom(1,2)-1);

y_w=[y_top y_bottom];

%% Diagnostic Plot
h1=subplot(2,1,1);
imshow(imadjust(frame1))
title(strcat({'Un-processed Frame '},num2str(frame), {' of '}, num2str(numframes)))
hold on
scatter(x_w(1,1),y_top,'blue','o','filled');
hold on
scatter(x_w(1,2),y_bottom,'red','o','filled');
hold off
h2=subplot(2,1,2);
imshow(channel)
title(strcat({'Processed Frame '},num2str(frame), {' of '}, num2str(numframes)))
hold on
scatter(x_w(1,1),y_top,'blue','o','filled');
hold on
scatter(x_w(1,2),y_bottom,'red','o','filled');
hold off
end
```

```
%%%%%%%%%%%%%%%%%%%%%%%%%%%%%%%%%%%%%%%%%%%%%%%%%%%%%%%%%%%%%%%%%%%%%%%
% Particle Centroid Function %
function
[A,cframe_binary]=centroidmain(cframe,frame,thresh,ecc_thresh,y_minimum,y_maximum)
%% Introduction
%TPL 5/12/11
%Recall Global Variables
global num;
global numframes;
%% Thresholding for particle centers
    cframe_binary=im2bw(cframe,thresh/255);

%% Remove Noise
    cframe_binary=bwareaopen(cframe_binary, 50); %removes objects less than pixel area
specified

%% imclose
cframe_binary=imclose(cframe_binary,strel('disk',4));
%imshow(cframe_binary)

%% fill holes
cframe_binary=imfill(cframe_binary,'holes');

%% filter large particles
    cframe_binary=cframe_binary-bwareaopen(cframe_binary, 750);

%% Watershed segmentation of "double" particles
    D = -bwdist(~cframe_binary);
    W=watershed(D); %label matrix W
    cframe_binary(W == 0) = 0;
    %imshow(cframe_binary) % Segmented image D (above)

%% Remove Noise
    cframe_binary=bwareaopen(cframe_binary, 50); %removes small objects
    %imshow(cframe_binary)

%% filter large particles
    cframe_binary=cframe_binary-bwareaopen(cframe_binary, 400);

%% Find Particles
    [B,L]=bwboundaries(cframe_binary, 8,'noholes');
    s=regionprops(L,'all');
    numparticles=max(L(:));
    shapes=[s.Eccentricity];
    areas=[s.Area];
    orient=[s.Orientation];


%% Find Centroids
    centers=[s.Centroid];
    c=zeros(size(B,1),2);
    for j=1:length(centers)/2
        c(j,1)=centers(2*j-1);
        c(j,2)=centers(2*j);
    end
    ck=c';
    if length(c)~=0
        keepers =  find((shapes<ecc_thresh)&(ck(2,:)>y_minimum)&(ck(2,:)<y_maximum));
        centroids=c(keepers,:);
    else
        keepers=[];
    end
```

```
    %% Calculate Intensity
    average_pixel_values=zeros(size(keepers,2),1);
    cmassk=zeros(size(keepers,2),2);
    for k = 1:numel(keepers)
        idx = s(keepers(k)).PixelIdxList;
        pixel_values = double(cframe(idx));
        sum_pixel_values = sum(pixel_values);
        average_pixel_values(k)=sum_pixel_values/size(pixel_values,1);
        x = s(keepers(k)).PixelList(:, 1);
        y = s(keepers(k)).PixelList(:, 2);
        cmassk(k,1) = sum(x .* pixel_values) / sum_pixel_values;
        cmassk(k,2) = sum(y .* pixel_values) / sum_pixel_values;
    end

%% prepare output
     if length(keepers)==0
        A{1,1}=[0 0 0 0 0 0 0 0 0 frame]
        else
        for j=1:length(keepers)
        A{j,1}=[centroids(j,1) centroids(j,2) cmassk(j,1) cmassk(j,2)
areas(keepers(j)) shapes(keepers(j)) orient(keepers(j)) average_pixel_values(j) num
frame]; %added x_offset
        num=num+1;
        end
    end

%% Animated display (optional, disable this on a slow computer)
h1=subplot(2,1,1);
imshow(cframe)
title(strcat({'Pre-processed Frame '},num2str(frame), {' of '}, num2str(numframes)))
h2=subplot(2,1,2);
imshow(cframe_binary)
hold on
title(strcat({'Processed Frame '},num2str(frame), {' of '}, num2str(numframes), {',
Threshold = '}, num2str(thresh)))
    for n=1:length(keepers)
        outline=B{keepers(n)};
        line(outline(:,2),outline(:,1),'Color','r','LineWidth',2)
        hold on
    end
    hold off
end
```

Appendix D

COMSOL Multiphysics Simulation Details

This section contains additional details of the three-dimensional transient CFD models used to simulate interparticle motion. As noted in Chapter 7, models were run using COMSOL 4.2a. The "Two-phase flow, moving mesh" node was used, along with a direct PARADISO solver. To verify the model and to ascertain mesh sensitivity, a single particle was first modeled. Table D.1 compares equilibrium conditions for our transient model to previously published work in a 50x50 μm square channel at Re_c = 20[143]. Note that the previous work (shown as "PRL" in Table D.1) used a static model which iteratively updated the particle position, velocity, and rotation rate until equilibrium was obtained. Despite the different methodologies used, the two models compare favorably. Additional verification for the two-particle models was provided in Chapter 7, where the computational interparticle spacing was compared to experimental data.

Table D.1 also addresses the mesh sensitivity. For the single particle, when the mesh points were increased by 20%, the computational time, already significant, increased by over 80%. Given that for multiple particles, more mesh deformation and remeshing would occur. Thus, the model used a "coarser" mesh. The number of mesh points and mesh sizes on the surfaces of the spheres for the two-particle cases presented in Chapter 7 are presented in Table D.2.

Table D.1. COMSOL Validation and Mesh Sensitivity for Single Particle Model.

Equilibrium Values	PRL [143]	Coarser	Finer	Refinement Change
y^* [-]	~0.27	0.263	0.263	0.2%
U_p/U_{max} [-]	~0.67	0.679	0.679	-0.1%
$\Omega_p h/U_p$ [-]	~0.1	0.108	0.109	0.8%
Mesh Points	N/A	319,969	384,088	20%
Time to Solve [hours]	N/A	28	52	86%

Table D.2. Two-particle COMSOL Model Mesh Details.

Channel Size	27x52				50x50
Particle Size	5 μm	10 μm		15 μm	10 μm
Flow Rate [μL /min]	5	5	10	5	33.5
Re_c	3.78	3.78	7.56	3.78	20
Mesh Points	280,022	308,487	306,304	356,095	319,969
Max. Mesh Size on Sphere [μm]	1.05	1.18	1.14	1.27	2.06

Appendix E

PDMS Deformation Model

This section contains additional details of a two-dimensional solid COMSOL model of PDMS deformation at the channel outlet for determining the error in U_p/U_{max} in Chapter 7. The particle velocities for Figures 7.3b and 7.7c were measured at the end of the nozzle section. Still, the fluid passed through a short channel section, through an outlet, and through the outlet tubing. Thus, there was still a gage pressure at this position relative to atmospheric pressure.

Table E.1 presents estimated gage pressures at the velocity measurement location for each flow rate tested in the 27x52 μm channel. Additionally, the table presents the deformation of the PDMS channel assuming the constant pressures in Table E.1. represented the boundary conditions (shown applied in Figure E.1). Table E.2 presents the same results for the 30x31 μm channel. In the model, PDMS was assumed to be a hyper-elastic material using a Neo-Hookean model[291]. We also assumed that he first Lamé parameter λ = 5.6 MPa and the second Lamé parameter μ = 0.62 MPa. The value $\Delta U_{max}/U_{max}$ represents the fractional error in U_{max} due to channel deformation only. Additional errors to the values of U_p/U_{max} presented in Chapter 7, e.g. from flow rate uncertainty, were calculated separately.

Table E.1. PDMS Deformation in 27x52 μm Channel.

Flow Rate [μL/min]	Estimated Pressure Drop from Nozzle to Outlet [kPa]	Top Deformation [μm]	One Side Deformation [μm]	Deformation Error ($\Delta U_{max}/U_{max}$) [-]
1.25	0.813	0.02	0.02	0.002
2.5	1.625	0.05	0.04	0.003
5	3.250	0.09	0.09	0.007
10	6.500	0.19	0.17	0.013
15	9.750	0.28	0.26	0.020
20	13.00	0.38	0.34	0.026
25	16.25	0.47	0.43	0.033
30	19.50	0.57	0.51	0.040
35	22.75	0.66	0.60	0.046
40	26.00	0.75	0.68	0.053

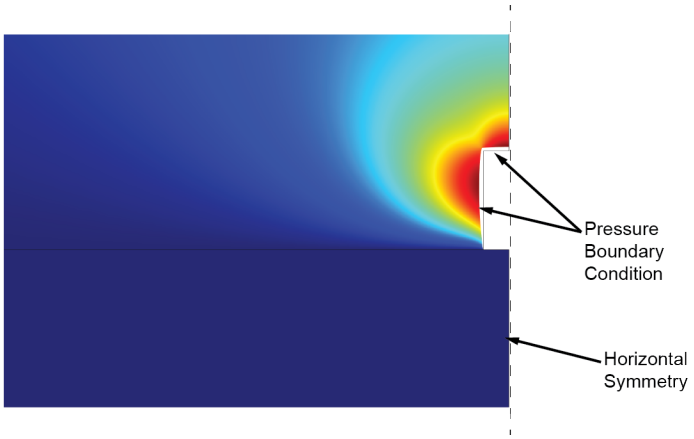

Figure E.1. Sample PDMS deformation model.

Table E.2. PDMS Deformation in 40x31 μm Channel.

Flow Rate [μL/min]	Estimated Pressure Drop from Nozzle to Outlet [kPa]	Top Deformation [μm]	One Side Deformation [μm]	Deformation Error ($\Delta U_{max}/U_{max}$) [-]
1.25	0.173	0.005	0.003	0.000
2.5	0.345	0.010	0.007	0.000
5	0.69	0.019	0.013	0.001
10	1.38	0.038	0.027	0.002
15	2.07	0.057	0.040	0.003
20	2.76	0.076	0.054	0.004
25	3.45	0.096	0.067	0.005
30	4.14	0.115	0.080	0.005
35	4.83	0.134	0.094	0.006
40	5.52	0.153	0.107	0.007

Appendix F

Curve Fit Parameters for Equation 7.8

Curve fit values (from COMSOL data of Table 7.1) for y^* and U_{slip}/U_{max} wer used in plotting Figure 7.7 from Equations 7.9-7.13. Curve fits are presented in Figures F.1 and F.2.

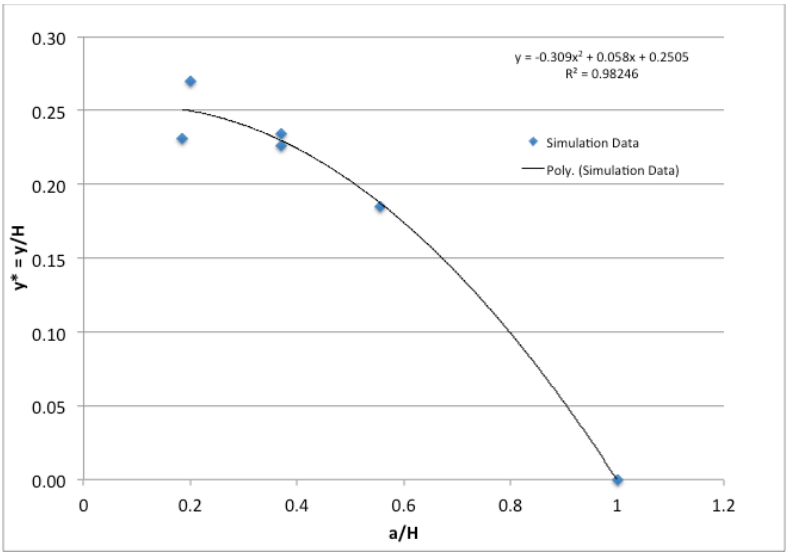

Figure F.1. Curve fit for *y.**

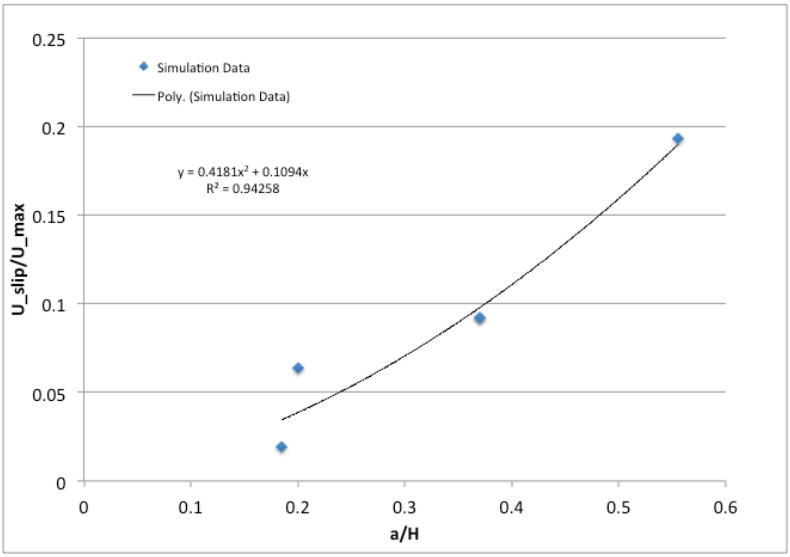

Figure F.1. Curve fit for U_{slip}/U_{max}.

References

[1] Beebe, D. J., Mensing, G. A. & Walker, G. M. Physics and applications of microfluidics in biology. *Annual review of biomedical engineering* **4**, 261-286,(2002).

[2] Melin, J. & Quake, S. R. Microfluidic large-scale integration: the evolution of design rules for biological automation. *Annual review of biophysics and biomolecular structure* **36**, 213-231,(2007).

[3] Mark, D., Haeberle, S., Roth, G., von Stetten, F. & Zengerle, R. Microfluidic lab-on-a-chip platforms: requirements, characteristics and applications. *Chemical Society reviews* **39**, 1153-1182,(2010).

[4] Duffy, D. C., McDonald, J. C., Schueller, O. J. A. & Whitesides, G. M. Rapid prototyping of microfluidic systems in poly(dimethylsiloxane). *Anal Chem* **70**, 4974-4984,(1998).

[5] Becker, H. Chips, money, industry, education and the "killer application". *Lab Chip* **9**, 1659-1660,(2009).

[6] Becker, H. Hype, hope and hubris: the quest for the killer application in microfluidics. *Lab Chip* **9**, 2119-2122,(2009).

[7] Becker, H. It's the economy. *Lab Chip* **9**, 2759-2762,(2009).

[8] Vincent, M. E., Liu, W., Haney, E. B. & Ismagilov, R. F. Microfluidic stochastic confinement enhances analysis of rare cells by isolating cells and creating high density environments for control of diffusible signals. *Chemical Society reviews* **39**, 974-984,(2010).

[9] Liu, W. S., Kim, H. J., Lucchetta, E. M., Du, W. B. & Ismagilov, R. F. Isolation, incubation, and parallel functional testing and identification by FISH of rare microbial single-copy cells from multi-species mixtures using the combination of chemistrode and stochastic confinement. *Lab Chip* **9**, 2153-2162,(2009).

[10] Lombardi, D. & Dittrich, P. S. Advances in microfluidics for drug discovery. *Expert Opin Drug Dis* **5**, 1081-1094,(2010).

[11] Gong, Z. *et al*. Drug effects analysis on cells using a high throughput microfluidic chip. *Biomedical microdevices* **13**, 215-219,(2011).

[12] Boedicker, J. Q., Vincent, M. E. & Ismagilov, R. F. Microfluidic Confinement of Single Cells of Bacteria in Small Volumes Initiates High-Density Behavior of Quorum Sensing and Growth and Reveals Its Variability. *Angew Chem Int Edit* **48**, 5908-5911,(2009).

[13] Segré, G. & Silberberg, A. Radial Particle Displacements in Poiseuille Flow of Suspensions. *Nature* **189**, 209-210,(1961).

[14] Bhagat, A. A. S., Kuntaegowdanahalli, S. S. & Papautsky, I. Inertial microfluidics for continuous particle filtration and extraction. *Microfluidics and nanofluidics* **7**, 217-226,(2008).

[15] Russom, A. *et al*. Differential inertial focusing of particles in curved low-aspect-ratio microchannels. *New journal of physics* **11**, 75025,(2009).

[16] Bhagat, A. A., Kuntaegowdanahalli, S. S. & Papautsky, I. Continuous particle separation in spiral microchannels using Dean flows and differential migration. *Lab Chip* **8**, 1906-1914,(2008).

[17] Di Carlo, D., Edd, J. F., Irimia, D., Tompkins, R. G. & Toner, M. Equilibrium separation and filtration of particles using differential inertial focusing. *Anal Chem* **80**, 2204-2211,(2008).
[18] Di Carlo, D., Irimia, D., Tompkins, R. G. & Toner, M. Continuous inertial focusing, ordering, and separation of particles in microchannels. *Proceedings of the National Academy of Sciences of the United States of America* **104**, 18892-18897,(2007).
[19] Oakey, J. *et al*. Particle Focusing in Staged Inertial Microfluidic Devices for Flow Cytometry. *Anal Chem* **82**, 3862-3867,(2010).
[20] Di Carlo, D. Inertial microfluidics. *Lab Chip* **9**, 3038-3046,(2009).
[21] Hong, J., deMello, A. J. & Jayasinghe, S. N. Bio-electrospraying and droplet-based microfluidics: control of cell numbers within living residues. *Biomedical materials* **5**, 21001,(2010).
[22] Givan, A. L. Flow cytometry: an introduction. *Methods in molecular biology* **699**, 1-29,(2011).
[23] Koster, S. *et al*. Drop-based microfluidic devices for encapsulation of single cells. *Lab Chip* **8**, 1110-1115,(2008).
[24] Edd, J. F. *et al*. Controlled encapsulation of single-cells into monodisperse picolitre drops. *Lab Chip* **8**, 1262-1264,(2008).
[25] Huebner, A. *et al*. Microdroplets: a sea of applications? *Lab Chip* **8**, 1244-1254,(2008).
[26] Casadevall i Solvas, X. & deMello, A. Droplet microfluidics: recent developments and future applications. *Chemical communications* **47**, 1936-1942,(2011).
[27] Zagnoni, M. & Cooper, J. M. Droplet microfluidics for high-throughput analysis of cells and particles. *Methods in cell biology* **102**, 25-48,(2011).
[28] Theberge, A. B. *et al*. Microdroplets in microfluidics: an evolving platform for discoveries in chemistry and biology. *Angew Chem Int Ed Engl* **49**, 5846-5868,(2010).
[29] Fair, R. B. Digital microfluidics: is a true lab-on-a-chip possible? *Microfluidics and Nanofluidics* **3**, 245-281,(2007).
[30] Choi, K. *et al*. Integration of field effect transistor-based biosensors with a digital microfluidic device for a lab-on-a-chip application. *Lab Chip* **12**, 1533-1539,(2012).
[31] Schaerli, Y. & Hollfelder, F. The potential of microfluidic water-in-oil droplets in experimental biology. *Molecular bioSystems* **5**, 1392-1404,(2009).
[32] Pekin, D. *et al*. Quantitative and sensitive detection of rare mutations using droplet-based microfluidics. *Lab Chip* **11**, 2156-2166,(2011).
[33] Markey, A. L., Mohr, S. & Day, P. J. High-throughput droplet PCR. *Methods* **50**, 277-281,(2010).
[34] Zhu, Z. *et al*. Single-molecule emulsion PCR in microfluidic droplets. *Analytical and bioanalytical chemistry* **403**, 2127-2143,(2012).
[35] Brouzes, E. *et al*. Droplet microfluidic technology for single-cell high-throughput screening. *Proceedings of the National Academy of Sciences of the United States of America* **106**, 14195-14200,(2009).
[36] Huebner, A. *et al*. Quantitative detection of protein expression in single cells using droplet microfluidics. *Chemical communications*, 1218-1220,(2007).
[37] Srisa-Art, M. *et al*. Identification of rare progenitor cells from human periosteal tissue using droplet microfluidics. *The Analyst* **134**, 2239-2245,(2009).
[38] *Search Results: Topic=("high throughput" microfluidic*)*, 2012).

[39] Osborne, G. W. Recent advances in flow cytometric cell sorting. *Methods in cell biology* **102**, 533-556,(2011).
[40] Virgo, P. F. & Gibbs, G. J. Flow cytometry in clinical pathology. *Annals of clinical biochemistry* **49**, 17-28,(2012).
[41] Eisenstein, M. Cell sorting: Divide and conquer. *Nature* **441**, 1179-1185,(2006).
[42] Ashcroft, R. G. & Lopez, P. A. Commercial high speed machines open new opportunities in high throughput flow cytometry (HTFC). *Journal of immunological methods* **243**, 13-24,(2000).
[43] Christopher, G. F. & Anna, S. L. Microfluidic methods for generating continuous droplet streams. *Journal of Physics D: Applied Physics* **40**, R319-R336,(2007).
[44] Teh, S. Y., Lin, R., Hung, L. H. & Lee, A. P. Droplet microfluidics. *Lab Chip* **8**, 198-220,(2008).
[45] Baroud, C. N., Gallaire, F. & Dangla, R. Dynamics of microfluidic droplets. *Lab Chip* **10**, 2032-2045,(2010).
[46] Seemann, R., Brinkmann, M., Pfohl, T. & Herminghaus, S. Droplet based microfluidics. *Reports on Progress in Physics* **75**, 016601,(2012).
[47] Hardt, S. & Hahn, T. Microfluidics with aqueous two-phase systems. *Lab Chip* **12**, 434-442,(2012).
[48] Xu, J. & Attinger, D. Drop on demand in a microfluidic chip. *Journal of Micromechanics and Microengineering* **18**, 065020,(2008).
[49] Kim, H. *et al*. Controlled production of emulsion drops using an electric field in a flow-focusing microfluidic device. *Applied Physics Letters* **91**, 133106,(2007).
[50] Anna, S. L., Bontoux, N. & Stone, H. A. Formation of dispersions using "flow focusing" in microchannels. *Applied Physics Letters* **82**, 364-366,(2003).
[51] Utada, A., Fernandez-Nieves, A., Stone, H. & Weitz, D. Dripping to Jetting Transitions in Coflowing Liquid Streams. *Physical Review Letters* **99**, 094502,(2007).
[52] Nisisako, T., Torii, T. & Higuchi, T. Droplet formation in a microchannel network. *Lab Chip* **2**, 24-26,(2002).
[53] Chu, L. Y., Utada, A. S., Shah, R. K., Kim, J. W. & Weitz, D. A. Controllable monodisperse multiple emulsions. *Angew Chem Int Edit* **46**, 8970-8974,(2007).
[54] Okushima, S., Nisisako, T., Torii, T. & Higuchi, T. Controlled production of monodisperse double emulsions by two-step droplet breakup in microfluidic devices. *Langmuir : the ACS journal of surfaces and colloids* **20**, 9905-9908,(2004).
[55] Dreyfus, R., Tabeling, P. & Willaime, H. Ordered and Disordered Patterns in Two-Phase Flows in Microchannels. *Physical Review Letters* **90**, 144505,(2003).
[56] Becker, H. & Gartner, C. Polymer microfabrication technologies for microfluidic systems. *Analytical and bioanalytical chemistry* **390**, 89-111,(2008).
[57] Tsao, C.-W. & DeVoe, D. L. Bonding of thermoplastic polymer microfluidics. *Microfluidics and Nanofluidics* **6**, 1-16,(2008).
[58] Roy, E., Geissler, M., Galas, J.-C. & Veres, T. Prototyping of microfluidic systems using a commercial thermoplastic elastomer. *Microfluidics and Nanofluidics* **11**, 235-244,(2011).
[59] Berthier, E., Young, E. W. K. & Beebe, D. Engineers are from PDMS-land, Biologists are from Polystyrenia. *Lab Chip* **12**, 1224-1237,(2012).
[60] Bong, K. W. *et al*. Non-polydimethylsiloxane devices for oxygen-free flow lithography. *Nat. Commun.* **3**, 805,(2012).

[61] Garstecki, P., Fuerstman, M. J., Stone, H. A. & Whitesides, G. M. Formation of droplets and bubbles in a microfluidic T-junction-scaling and mechanism of break-up. *Lab Chip* **6**, 437-446,(2006).
[62] De Menech, M., Garstecki, P., Jousse, F. & Stone, H. A. Transition from squeezing to dripping in a microfluidic T-shaped junction. *Journal of Fluid Mechanics* **595**, 141-161,(2008).
[63] Pathak, M. Numerical simulation of membrane emulsification: Effect of flow properties in the transition from dripping to jetting. *J Membrane Sci* **382**, 166-176,(2011).
[64] Abate, A. R., Mary, P., van Steijn, V. & Weitz, D. A. Experimental validation of plugging during drop formation in a T-junction. *Lab Chip* **12**, 1516-1521,(2012).
[65] Bibette, J., Calderon, F. L. & Poulin, P. Emulsions: basic principles. *Reports on Progress in Physics* **62**, 969-1033,(1999).
[66] Baret, J. C. Surfactants in droplet-based microfluidics. *Lab Chip* **12**, 422-433,(2012).
[67] Holtze, C. *et al*. Biocompatible surfactants for water-in-fluorocarbon emulsions. *Lab Chip* **8**, 1632-1639,(2008).
[68] Holt, D. J., Payne, R. J., Chow, W. Y. & Abell, C. Fluorosurfactants for microdroplets: interfacial tension analysis. *Journal of colloid and interface science* **350**, 205-211,(2010).
[69] Holt, D. J., Payne, R. J. & Abell, C. Synthesis of novel fluorous surfactants for microdroplet stabilisation in fluorous oil streams. *Journal of Fluorine Chemistry* **131**, 398-407,(2010).
[70] Yan, N. X., Gray, M. R. & Masliyah, J. H. On water-in-oil emulsions stabilized by fine solids. *Colloid Surf. A-Physicochem. Eng. Asp.* **193**, 97-107,(2001).
[71] Simovic, S. & Prestidge, C. A. Nanoparticles of varying hydrophobicity at the emulsion droplet-water interface: Adsorption and coalescence stability. *Langmuir : the ACS journal of surfaces and colloids* **20**, 8357-8365,(2004).
[72] Sohel Murshed, S. M., Tan, S.-H. & Nguyen, N.-T. Temperature dependence of interfacial properties and viscosity of nanofluids for droplet-based microfluidics. *Journal of Physics D: Applied Physics* **41**, 085502,(2008).
[73] Bresme, F. & Oettel, M. Nanoparticles at fluid interfaces. *Journal of Physics: Condensed Matter* **19**, 413101,(2007).
[74] Bringer, M. R., Gerdts, C. J., Song, H., Tice, J. D. & Ismagilov, R. F. Microfluidic systems for chemical kinetics that rely on chaotic mixing in droplets. *Philos T Roy Soc A* **362**, 1087-1104,(2004).
[75] Cai, L. F., Zhu, Y., Du, G. S. & Fang, Q. Droplet-based microfluidic flow injection system with large-scale concentration gradient by a single nanoliter-scale injection for enzyme inhibition assay. *Anal Chem* **84**, 446-452,(2012).
[76] Atencia, J. & Beebe, D. J. Controlled microfluidic interfaces. *Nature* **437**, 648-655,(2005).
[77] Capretto, L., Cheng, W., Hill, M. & Zhang, X. Micromixing within microfluidic devices. *Topics in current chemistry* **304**, 27-68,(2011).
[78] Song, H., Chen, D. L. & Ismagilov, R. F. Reactions in droplets in microflulidic channels. *Angew Chem Int Edit* **45**, 7336-7356,(2006).
[79] Yeh, C.-H., Chen, Y.-C. & Lin, Y.-C. Generation of droplets with different concentrations using gradient-microfluidic droplet generator. *Microfluidics and Nanofluidics* **11**, 245-253,(2011).

[80] Bajpayee, A., Edd, J. F., Chang, A. & Toner, M. Concentration of Glycerol in Aqueous Microdroplets by Selective Removal of Water. *Anal Chem* **82**, 1288-1291,(2010).
[81] Wong, E. H. M., Rondeau, E., Schuetz, P. & Cooper-White, J. A microfluidic-based method for the transfer of biopolymer particles from an oil phase to an aqueous phase. *Lab Chip* **9**, 2582-2590,(2009).
[82] Chen, F. *et al*. Chemical transfection of cells in picoliter aqueous droplets in fluorocarbon oil. *Anal Chem* **83**, 8816-8820,(2011).
[83] Abbyad, P., Tharaux, P. L., Martin, J. L., Baroud, C. N. & Alexandrou, A. Sickling of red blood cells through rapid oxygen exchange in microfluidic drops. *Lab Chip* **10**, 2505-2512,(2010).
[84] Lindstrom, S. & Andersson-Svahn, H. Overview of single-cell analyses: microdevices and applications. *Lab Chip* **10**, 3363-3372,(2010).
[85] Clausell-Tormos, J. *et al*. Droplet-based microfluidic platforms for the encapsulation and screening of mammalian cells and multicellular organisms. *Chemistry & biology* **15**, 427-437,(2008).
[86] Luo, D., Pullela, S. R., Marquez, M. & Cheng, Z. Cell encapsules with tunable transport and mechanical properties. *Biomicrofluidics* **1**, 34102,(2007).
[87] Um, E., Lee, D.-S., Pyo, H.-B. & Park, J.-K. Continuous generation of hydrogel beads and encapsulation of biological materials using a microfluidic droplet-merging channel. *Microfluidics and Nanofluidics* **5**, 541-549,(2008).
[88] Leonard, A. *et al*. Whole-cell based hybrid materials for green energy production, environmental remediation and smart cell-therapy. *Chemical Society reviews* **40**, 860-885,(2011).
[89] Eun, Y. J., Utada, A. S., Copeland, M. F., Takeuchi, S. & Weibel, D. B. Encapsulating bacteria in agarose microparticles using microfluidics for high-throughput cell analysis and isolation. *ACS chemical biology* **6**, 260-266,(2011).
[90] Lin, Y. S., Yang, C. H., Lu, K., Huang, K. S. & Zheng, Y. Z. Synthesis of agar microparticles using temperature-controlled microfluidic devices for Cordyceps militaris cultivation. *Electrophoresis* **32**, 3157-3163,(2011).
[91] Velasco, D., Tumarkin, E. & Kumacheva, E. Microfluidic encapsulation of cells in polymer microgels. *Small* **8**, 1633-1642,(2012).
[92] Leng, X., Zhang, W., Wang, C., Cui, L. & Yang, C. J. Agarose droplet microfluidics for highly parallel and efficient single molecule emulsion PCR. *Lab Chip* **10**, 2841-2843,(2010).
[93] Berthier, J. *et al*. Highly viscous fluids in pressure actuated flow focusing devices. *Sensors and Actuators A: Physical* **158**, 140-148,(2010).
[94] Rossow, T. *et al*. Controlled synthesis of cell-laden microgels by radical-free gelation in droplet microfluidics. *J Am Chem Soc* **134**, 4983-4989,(2012).
[95] Nisisako, T., Torii, T., Takahashi, T. & Takizawa, Y. Synthesis of Monodisperse Bicolored Janus Particles with Electrical Anisotropy Using a Microfluidic Co-Flow System. *Advanced Materials* **18**, 1152-1156,(2006).
[96] Walther, A. & Müller, A. H. E. Janus particles. *Soft Matter* **4**, 663,(2008).
[97] Yuet, K. P., Hwang, D. K., Haghgooie, R. & Doyle, P. S. Multifunctional superparamagnetic Janus particles. *Langmuir : the ACS journal of surfaces and colloids* **26**, 4281-4287,(2010).

[98] Nisisako, T. & Hatsuzawa, T. A microfluidic cross-flowing emulsion generator for producing biphasic droplets and anisotropically shaped polymer particles. *Microfluidics and Nanofluidics* **9**, 427-437,(2009).
[99] Kim, J. W., Utada, A. S., Fernandez-Nieves, A., Hu, Z. & Weitz, D. A. Fabrication of monodisperse gel shells and functional microgels in microfluidic devices. *Angew Chem Int Ed Engl* **46**, 1819-1822,(2007).
[100] Seiffert, S., Romanowsky, M. B. & Weitz, D. A. Janus microgels produced from functional precursor polymers. *Langmuir : the ACS journal of surfaces and colloids* **26**, 14842-14847,(2010).
[101] Seiffert, S. & Weitz, D. A. Controlled fabrication of polymer microgels by polymer-analogous gelation in droplet microfluidics. *Soft Matter* **6**, 3184,(2010).
[102] Teh, S. Y., Khnouf, R., Fan, H. & Lee, A. P. Stable, biocompatible lipid vesicle generation by solvent extraction-based droplet microfluidics. *Biomicrofluidics* **5**, 44113,(2011).
[103] Zhang, J. *et al*. One-step fabrication of supramolecular microcapsules from microfluidic droplets. *Science* **335**, 690-694,(2012).
[104] Gulati, S. *et al*. Opportunities for microfluidic technologies in synthetic biology. *Journal of the Royal Society, Interface / the Royal Society* **6 Suppl 4**, S493-506,(2009).
[105] Vinuselvi, P. *et al*. Microfluidic technologies for synthetic biology. *International journal of molecular sciences* **12**, 3576-3593,(2011).
[106] van Dongen, S. F. M. *et al*. Biohybrid Polymer Capsules. *Chem Rev* **109**, 6212-6274,(2009).
[107] Bysell, H., Mansson, R., Hansson, P. & Malmsten, M. Microgels and microcapsules in peptide and protein drug delivery. *Advanced drug delivery reviews* **63**, 1172-1185,(2011).
[108] Rabanel, J. M., Banquy, X., Zouaoui, H., Mokhtar, M. & Hildgen, P. Progress Technology in Microencapsulation Methods for Cell Therapy. *Biotechnol Progr* **25**, 946-963,(2009).
[109] Yin, H. & Marshall, D. Microfluidics for single cell analysis. *Current opinion in biotechnology* **23**, 110-119,(2012).
[110] Fritzsch, F. S., Dusny, C., Frick, O. & Schmid, A. Single-cell analysis in biotechnology, systems biology, and biocatalysis. *Annual review of chemical and biomolecular engineering* **3**, 129-155,(2012).
[111] Iverson, B. D. & Garimella, S. V. Recent advances in microscale pumping technologies: a review and evaluation. *Microfluidics and Nanofluidics* **5**, 145-174,(2008).
[112] Nisar, A., Afzulpurkar, N., Mahaisavariya, B. & Tuantranont, A. MEMS-based micropumps in drug delivery and biomedical applications. *Sensors and Actuators B: Chemical* **130**, 917-942,(2008).
[113] Link, D. R., Anna, S. L., Weitz, D. A. & Stone, H. A. Geometrically mediated breakup of drops in microfluidic devices. *Physical Review Letters* **92**, 054503,(2004).
[114] Leshansky, A. M. & Pismen, L. M. Breakup of drops in a microfluidic T junction. *Physics of Fluids* **21**, 023303,(2009).
[115] Hatch, A. C., Fisher, J. S., Pentoney, S. L., Yang, D. L. & Lee, A. P. Tunable 3D droplet self-assembly for ultra-high-density digital micro-reactor arrays. *Lab Chip* **11**, 2509-2517,(2011).
[116] Carlson, A., Do-Quang, M. & Amberg, G. Droplet dynamics in a bifurcating channel. *International Journal of Multiphase Flow* **36**, 397-405,(2010).

[117] Menetrier-Deremble, L. & Tabeling, P. Droplet breakup in microfluidic junctions of arbitrary angles. *Physical Review E* **74**, 035303,(2006).
[118] Lai, A., Bremond, N. & Stone, H. A. Separation-driven coalescence of droplets: an analytical criterion for the approach to contact. *Journal of Fluid Mechanics* **632**, 97-107,(2009).
[119] Niu, X., Gulati, S., Edel, J. B. & deMello, A. J. Pillar-induced droplet merging in microfluidic circuits. *Lab Chip* **8**, 1837-1841,(2008).
[120] Niu, X. Z., Gielen, F., Edel, J. B. & deMello, A. J. A microdroplet dilutor for high-throughput screening. *Nat Chem* **3**, 437-442,(2011).
[121] Fidalgo, L. M., Abell, C. & Huck, W. T. S. Surface-induced droplet fusion in microfluidic devices. *Lab Chip* **7**, 984-986,(2007).
[122] Zagnoni, M., Le Lain, G. & Cooper, J. M. Electrocoalescence mechanisms of microdroplets using localized electric fields in microfluidic channels. *Langmuir : the ACS journal of surfaces and colloids* **26**, 14443-14449,(2010).
[123] Niu, X. Z., Gielen, F., deMello, A. J. & Edel, J. B. Electro-Coalescence of Digitally Controlled Droplets. *Anal Chem* **81**, 7321-7325,(2009).
[124] Baroud, C. N., de Saint Vincent, M. R. & Delville, J. P. An optical toolbox for total control of droplet microfluidics. *Lab Chip* **7**, 1029-1033,(2007).
[125] Zhan, Y. H., Wang, J., Bao, N. & Lu, C. Electroporation of Cells in Microfluidic Droplets. *Anal Chem* **81**, 2027-2031,(2009).
[126] He, M. Y. *et al*. Selective encapsulation of single cells and subcellular organelles into picoliter- and femtoliter-volume droplets. *Anal Chem* **77**, 1539-1544,(2005).
[127] Kim, H., Vishniakou, S. & Faris, G. W. Petri dish PCR: laser-heated reactions in nanoliter droplet arrays. *Lab Chip* **9**, 1230-1235,(2009).
[128] Kim, H., Dixit, S., Green, C. J. & Faris, G. W. Nanodroplet real-time PCR system with laser assisted heating. *Opt. Express* **17**, 218-227,(2009).
[129] Di Carlo, D., Wu, L. Y. & Lee, L. P. Dynamic single cell culture array. *Lab Chip* **6**, 1445-1449,(2006).
[130] Srisa-Art, M., deMello, A. J. & Edel, J. B. High-Efficiency Single-Molecule Detection within Trapped Aqueous Microdroplets. *J. Phys. Chem. B* **114**, 15766-15772,(2010).
[131] Bai, Y. P. *et al*. A double droplet trap system for studying mass transport across a droplet-droplet interface. *Lab Chip* **10**, 1281-1285,(2010).
[132] Huebner, A. M., Abell, C., Huck, W. T., Baroud, C. N. & Hollfelder, F. Monitoring a reaction at submillisecond resolution in picoliter volumes. *Anal Chem* **83**, 1462-1468,(2011).
[133] Hatch, A. C. *et al*. 1-Million droplet array with wide-field fluorescence imaging for digital PCR. *Lab Chip*, 3838-3845,(2011).
[134] Schmitz, C. H., Rowat, A. C., Koster, S. & Weitz, D. A. Dropspots: a picoliter array in a microfluidic device. *Lab Chip* **9**, 44-49,(2009).
[135] Edd, J. F., Humphry, K. J., Irimia, D., Weitz, D. A. & Toner, M. Nucleation and solidification in static arrays of monodisperse drops. *Lab Chip* **9**, 1859-1865,(2009).
[136] Taylor, R. J. *et al*. Dynamic analysis of MAPK signaling using a high-throughput microfluidic single-cell imaging platform. *Proceedings of the National Academy of Sciences of the United States of America* **106**, 3758-3763,(2009).
[137] Falconnet, D. *et al*. High-throughput tracking of single yeast cells in a microfluidic imaging matrix. *Lab Chip* **11**, 466-473,(2011).

[138] Gomez-Sjoberg, R., Leyrat, A. A., Pirone, D. M., Chen, C. S. & Quake, S. R. Versatile, fully automated, microfluidic cell culture system. *Anal Chem* **79**, 8557-8563,(2007).
[139] Yamada, M., Nakashima, M. & Seki, M. Pinched flow fractionation: Continuous size separation of particles utilizing a laminar flow profile in a pinched microchannel. *Anal Chem* **76**, 5465-5471,(2004).
[140] Huang, L. R., Cox, E. C., Austin, R. H. & Sturm, J. C. Continuous particle separation through deterministic lateral displacement. *Science* **304**, 987-990,(2004).
[141] Joensson, H. N., Uhlen, M. & Svahn, H. A. Droplet size based separation by deterministic lateral displacement-separating droplets by cell-induced shrinking. *Lab Chip* **11**, 1305-1310,(2011).
[142] Segré, G. & Silberberg, A. Behaviour of macroscopic rigid spheres in Poiseuille flow Part 2. Experimental results and interpretation. *Journal of Fluid Mechanics* **14**, 136,(1962).
[143] Di Carlo, D., Edd, J., Humphry, K., Stone, H. & Toner, M. Particle Segregation and Dynamics in Confined Flows. *Physical Review Letters* **102**, 094503,(2009).
[144] Kuntaegowdanahalli, S. S., Bhagat, A. A., Kumar, G. & Papautsky, I. Inertial microfluidics for continuous particle separation in spiral microchannels. *Lab Chip* **9**, 2973-2980,(2009).
[145] Jonas, A. & Zemanek, P. Light at work: The use of optical forces for particle manipulation, sorting, and analysis. *Electrophoresis* **29**, 4813-4851,(2008).
[146] Ashkin, A., Dziedzic, J. M., Bjorkholm, J. E. & Chu, S. OBSERVATION OF A SINGLE-BEAM GRADIENT FORCE OPTICAL TRAP FOR DIELECTRIC PARTICLES. *Optics Letters* **11**, 288-290,(1986).
[147] Lorenz, R. M., Edgar, J. S., Jeffries, G. D. M. & Chiu, D. T. Microfluidic and optical systems for the on-demand generation and manipulation of single femtoliter-volume aqueous droplets. *Anal Chem* **78**, 6433-6439,(2006).
[148] Wang, M. M. *et al*. Microfluidic sorting of mammalian cells by optical force switching. *Nature biotechnology* **23**, 83-87,(2005).
[149] Chen, J., Ng, J., Lin, Z. F. & Chan, C. T. Optical pulling force. *Nat. Photonics* **5**, 531-534,(2011).
[150] Zhang, K. *et al*. On-chip manipulation of continuous picoliter-volume superparamagnetic droplets using a magnetic force. *Lab Chip* **9**, 2992-2999,(2009).
[151] Lombardi, D. & Dittrich, P. S. Droplet microfluidics with magnetic beads: a new tool to investigate drug–protein interactions. *Analytical and bioanalytical chemistry* **399**, 347-352,(2010).
[152] Zhang, D. Y. *et al*. Functionalization of whole-cell bacterial reporters with magnetic nanoparticles. *Microb. Biotechnol.* **4**, 89-97,(2011).
[153] Fakhrullin, R. F., Garcia-Alonso, J. & Paunov, V. N. A direct technique for preparation of magnetically functionalised living yeast cells. *Soft Matter* **6**, 391-397,(2010).
[154] Kekarainen, T., Mannelin, S., Laine, J. & Jaatinen, T. Optimization of immunomagnetic separation for cord blood-derived hematopoietic stem cells. *BMC Cell Biol.* **7**, 30,(2006).
[155] Pankhurst, Q. A., Connolly, J., Jones, S. K. & Dobson, J. Applications of magnetic nanoparticles in biomedicine. *J. Phys. D-Appl. Phys.* **36**, R167-R181,(2003).
[156] Lombardi, D. & Dittrich, P. S. Droplet microfluidics with magnetic beads: a new tool to investigate drug-protein interactions. *Analytical and bioanalytical chemistry* **399**, 347-352,(2011).

[157] Liu, C., Stakenborg, T., Peeters, S. & Lagae, L. Cell manipulation with magnetic particles toward microfluidic cytometry. *J. Appl. Phys.* **105**, 102014,(2009).
[158] Petersson, F., Nilsson, A., Holm, C., Jonsson, H. & Laurell, T. Continuous separation of lipid particles from erythrocytes by means of laminar flow and acoustic standing wave forces. *Lab Chip* **5**, 20-22,(2005).
[159] Bruus, H. Acoustofluidics 1: Governing equations in microfluidics. *Lab Chip* **11**, 3742-3751,(2011).
[160] Petersson, F., Aberg, L., Sward-Nilsson, A. M. & Laurell, T. Free flow acoustophoresis: Microfluidic-based mode of particle and cell separation. *Anal Chem* **79**, 5117-5123,(2007).
[161] Franke, T., Braunmuller, S., Schmid, L., Wixforth, A. & Weitz, D. A. Surface acoustic wave actuated cell sorting (SAWACS). *Lab Chip* **10**, 789-794,(2010).
[162] Franke, T., Abate, A. R., Weitz, D. A. & Wixforth, A. Surface acoustic wave (SAW) directed droplet flow in microfluidics for PDMS devices. *Lab Chip* **9**, 2625-2627,(2009).
[163] Link, D. R. *et al*. Electric control of droplets in microfluidic devices. *Angew Chem Int Ed Engl* **45**, 2556-2560,(2006).
[164] Pethig, R. Review Article-Dielectrophoresis: Status of the theory, technology, and applications. *Biomicrofluidics* **4**, 022811,(2010).
[165] Baret, J. C. *et al*. Fluorescence-activated droplet sorting (FADS): efficient microfluidic cell sorting based on enzymatic activity. *Lab Chip* **9**, 1850-1858,(2009).
[166] Hu, X. Y. *et al*. Marker-specific sorting of rare cells using dielectrophoresis. *Proceedings of the National Academy of Sciences of the United States of America* **102**, 15757-15761,(2005).
[167] Pregibon, D. C., Toner, M. & Doyle, P. S. Multifunctional encoded particles for high-throughput biomolecule analysis. *Science* **315**, 1393-1396,(2007).
[168] Bong, K. W., Chapin, S. C. & Doyle, P. S. Magnetic Barcoded Hydrogel Microparticles for Multiplexed Detection. *Langmuir : the ACS journal of surfaces and colloids* **26**, 8008-8014,(2010).
[169] Ji, X.-H. *et al*. On-demand preparation of quantum dot-encoded microparticles using a droplet microfluidic system. *Lab Chip* **11**, 2561,(2011).
[170] Ji, X.-H. *et al*. Integrated parallel microfluidic device for simultaneous preparation of multiplex optical-encoded microbeads with distinct quantum dot barcodes. *Journal of Materials Chemistry* **21**, 13380,(2011).
[171] Zhao, Y. *et al*. Microfluidic generation of multifunctional quantum dot barcode particles. *J Am Chem Soc* **133**, 8790-8793,(2011).
[172] Goldner, L. S., Jofre, A. M. & Tang, J. Y. in *Methods in Enzymology, Vol 472: Single Molecule Tools, Pt A: Fluorescence Based Approaches* Vol. 472 *Methods in Enzymology* (ed N. G. Walter) 61-88 (Elsevier Academic Press Inc, 2010).
[173] Damean, N., Olguin, L. F., Hollfelder, F., Abell, C. & Huck, W. T. S. Simultaneous measurement of reactions in microdroplets filled by concentration gradients. *Lab Chip* **9**, 1707-1713,(2009).
[174] Song, H. & Ismagilov, R. F. Millisecond kinetics on a microfluidic chip using nanoliters of reagents. *J Am Chem Soc* **125**, 14613-14619,(2003).
[175] Ng, K. C., Heredia, K. H. & Kliewer, D. Note: A method to isolate and detect a large number of single molecules by microdroplet fluorescence spectroscopy. *Rev. Sci. Instrum.* **83**, 036107,(2012).

[176] Srisa-Art, M., Dyson, E. C., Demello, A. J. & Edel, J. B. Monitoring of real-time streptavidin-biotin binding kinetics using droplet microfluidics. *Anal Chem* **80**, 7063-7067,(2008).
[177] Dittrich, P. S., Jahnz, M. & Schwille, P. A new embedded process for compartmentalized cell-free protein expression and on-line detection in microfluidic devices. *Chembiochem : a European journal of chemical biology* **6**, 811-814,(2005).
[178] Joensson, H. N., Zhang, C., Uhlen, M. & Andersson-Svahn, H. A homogeneous assay for protein analysis in droplets by fluorescence polarization. *Electrophoresis* **33**, 436-439,(2012).
[179] Fidalgo, L. M. *et al*. From microdroplets to microfluidics: Selective emulsion separation in microfluidic devices. *Angew Chem Int Edit* **47**, 2042-2045,(2008).
[180] Zhu, Y. & Fang, Q. Integrated Droplet Analysis System with Electrospray Ionization-Mass Spectrometry Using a Hydrophilic Tongue-Based Droplet Extraction Interface. *Anal Chem* **82**, 8361-8366,(2010).
[181] Huang, W. E., Griffiths, R. I., Thompson, I. P., Bailey, M. J. & Whiteley, A. S. Raman microscopic analysis of single microbial cells. *Anal Chem* **76**, 4452-4458,(2004).
[182] Li, M., Xu, J., Romero-Gonzalez, M., Banwart, S. A. & Huang, W. E. Single cell Raman spectroscopy for cell sorting and imaging. *Current opinion in biotechnology* **23**, 56-63,(2012).
[183] Huang, W. E., Li, M. Q., Jarvis, R. M., Goodacre, R. & Banwart, S. A. in *Advances in Applied Microbiology, Vol 70* Vol. 70 *Advances in Applied Microbiology* (eds A. I. Laskin, S. Sariaslani, & G. M. Gadd) 153-186 (Elsevier Academic Press Inc, 2010).
[184] Lau, A. Y., Lee, L. P. & Chan, J. W. An integrated optofluidic platform for Raman-activated cell sorting. *Lab Chip* **8**, 1116-1120,(2008).
[185] Lee, S. E. & Lee, L. P. Biomolecular plasmonics for quantitative biology and nanomedicine. *Current opinion in biotechnology* **21**, 489-497,(2010).
[186] Walter, A., Marz, A., Schumacher, W., Rosch, P. & Popp, J. Towards a fast, high specific and reliable discrimination of bacteria on strain level by means of SERS in a microfluidic device. *Lab Chip* **11**, 1013-1021,(2011).
[187] Syme, C. D., Martino, C., Yusvana, R., Sirimuthu, N. M. & Cooper, J. M. Quantitative characterization of individual microdroplets using surface-enhanced resonance Raman scattering spectroscopy. *Anal Chem* **84**, 1491-1495,(2012).
[188] Cecchini, M. P. *et al*. Ultrafast surface enhanced resonance Raman scattering detection in droplet-based microfluidic systems. *Anal Chem* **83**, 3076-3081,(2011).
[189] Ernst, A., Streule, W., Schmitt, N., Zengerle, R. & Koltay, P. A capacitive sensor for non-contact nanoliter droplet detection. *Sensors and Actuators A: Physical* **153**, 57-63,(2009).
[190] Elbuken, C., Glawdel, T., Chan, D. & Ren, C. L. Detection of microdroplet size and speed using capacitive sensors. *Sensors and Actuators A: Physical* **171**, 55-62,(2011).
[191] Cahill, B. P., Land, R., Nacke, T., Min, M. & Beckmann, D. Contactless sensing of the conductivity of aqueous droplets in segmented flow. *Sensors and Actuators B: Chemical* **159**, 286-293,(2011).
[192] Moiseeva, E. V., Fletcher, A. A. & Harnett, C. K. Thin-film electrode based droplet detection for microfluidic systems. *Sensors and Actuators B: Chemical* **155**, 408-414,(2011).

[193] Sadeghi, S. *et al*. On Chip Droplet Characterization: A Practical, High-Sensitivity Measurement of Droplet Impedance in Digital Microfluidics. *Anal Chem* **84**, 1915-1923,(2012).
[194] Kautz, R. A., Goetzinger, W. K. & Karger, B. L. High-throughput microcoil NMR of compound libraries using zero-dispersion segmented flow analysis. *J. Comb. Chem.* **7**, 14-20,(2005).
[195] Lin, Y. Q., Schiavo, S., Orjala, J., Vouros, P. & Kautz, R. Microscale LC-MS-NMR Platform Applied to the Identification of Active Cyanobacterial Metabolites. *Anal Chem* **80**, 8045-8054,(2008).
[196] Lee, H., Sun, E., Ham, D. & Weissleder, R. Chip-NMR biosensor for detection and molecular analysis of cells. *Nat. Med.* **14**, 869-874,(2008).
[197] Lee, H., Yoon, T. J. & Weissleder, R. Ultrasensitive Detection of Bacteria Using Core-Shell Nanoparticles and an NMR-Filter System. *Angew Chem Int Edit* **48**, 5657-5660,(2009).
[198] Haun, J. B. *et al*. Micro-NMR for Rapid Molecular Analysis of Human Tumor Samples. *Sci Transl Med* **3**,(2011).
[199] Haun, J. B., Yoon, T. J., Lee, H. & Weissleder, R. Magnetic nanoparticle biosensors. *Wires Nanomed Nanobi* **2**, 291-304,(2010).
[200] Prabaharan, M. & Mano, J. F. Stimuli-responsive hydrogels based on polysaccharides incorporated with thermo-responsive polymers as novel biomaterials. *Macromol. Biosci.* **6**, 991-1008,(2006).
[201] Madsen, J. & Armes, S. P. (Meth)acrylic stimulus-responsive block copolymer hydrogels. *Soft Matter* **8**, 592-605,(2012).
[202] Salehpour, S. & Dube, M. A. Application Properties of Stimuli-Responsive Polyglycerol Hydrogels. *J. Macromol. Sci. Part A-Pure Appl. Chem.* **49**, 103-110,(2012).
[203] Liu, J. W. Oligonucleotide-functionalized hydrogels as stimuli responsive materials and biosensors. *Soft Matter* **7**, 6757-6767,(2011).
[204] Jiang, K., Thomas, P. C., Forry, S. P., DeVoe, D. L. & Raghavan, S. R. Microfluidic synthesis of monodisperse PDMS microbeads as discrete oxygen sensors. *Soft Matter* **8**, 923,(2012).
[205] Hofmann, T. W., Hanselmann, S., Janiesch, J. W., Rademacher, A. & Bohm, C. H. Applying microdroplets as sensors for label-free detection of chemical reactions. *Lab Chip* **12**, 916-922,(2012).
[206] Boedicker, J. Q., Li, L., Kline, T. R. & Ismagilov, R. F. Detecting bacteria and determining their susceptibility to antibiotics by stochastic confinement in nanoliter droplets using plug-based microfluidics. *Lab Chip* **8**, 1265-1272,(2008).
[207] Joensson, H. N. *et al*. Detection and Analysis of Low-Abundance Cell-Surface Biomarkers Using Enzymatic Amplification in Microfluidic Droplets. *Angew Chem Int Edit* **48**, 2518-2521,(2009).
[208] Kumaresan, P., Yang, C. J., Cronier, S. A., Blazej, R. G. & Mathies, R. A. High-throughput single copy DNA amplification and cell analysis in engineered nanoliter droplets. *Anal Chem* **80**, 3522-3529,(2008).
[209] Guo, M. T., Rotem, A., Heyman, J. A. & Weitz, D. A. Droplet microfluidics for high-throughput biological assays. *Lab Chip* **12**, 2146-2155,(2012).
[210] Lecault, V. *et al*. High-throughput analysis of single hematopoietic stem cell proliferation in microfluidic cell culture arrays. *Nature methods* **8**, 581-U593,(2011).

[211] Fallah-Araghi, A., Baret, J. C., Ryckelynck, M. & Griffiths, A. D. A completely in vitro ultrahigh-throughput droplet-based microfluidic screening system for protein engineering and directed evolution. *Lab Chip* **12**, 882-891,(2012).
[212] Zhang, H., Jenkins, G., Zou, Y., Zhu, Z. & Yang, C. J. Massively parallel single-molecule and single-cell emulsion reverse transcription polymerase chain reaction using agarose droplet microfluidics. *Anal Chem* **84**, 3599-3606,(2012).
[213] Zhang, W. Y. *et al*. Highly parallel single-molecule amplification approach based on agarose droplet polymerase chain reaction for efficient and cost-effective aptamer selection. *Anal Chem* **84**, 350-355,(2012).
[214] Mastrobattista, E. *et al*. High-throughput screening of enzyme libraries: In vitro evolution of a beta-galactosidase by fluorescence-activated sorting of double emulsions. *Chemistry & biology* **12**, 1291-1300,(2005).
[215] Bernath, K. *et al*. In vitro compartmentalization by double emulsions: sorting and gene enrichment by fluorescence activated cell sorting. *Anal. Biochem.* **325**, 151-157,(2004).
[216] Nagrath, S. *et al*. Isolation of rare circulating tumour cells in cancer patients by microchip technology. *Nature* **450**, 1235-U1210,(2007).
[217] Boyum, A. Separation of Lymphocytes, Granulocytes, and Monocytes from Human-Blood Using Iodinated Density Gradient Media. *Method Enzymol* **108**, 88-102,(1984).
[218] Gossett, D. R. *et al*. Label-free cell separation and sorting in microfluidic systems. *Analytical and bioanalytical chemistry* **397**, 3249-3267,(2010).
[219] Boitard, L. *et al*. Monitoring single-cell bioenergetics via the coarsening of emulsion droplets. *Proceedings of the National Academy of Sciences of the United States of America* **109**, 7181-7186,(2012).
[220] Jimenez, A. M. *et al*. Towards high throughput production of artificial egg oocytes using microfluidics. *Lab Chip* **11**, 429-434,(2011).
[221] Bourouina, N., Husson, J., Hivroz, C. & Henry, N. Biomimetic Droplets for Artificial Engagement of Living Cell Surface Receptors: The Specific Case of the T-Cell. *Langmuir : the ACS journal of surfaces and colloids* **28**, 6106-6113,(2012).
[222] Zagnoni, M. Miniaturised technologies for the development of artificial lipid bilayer systems. *Lab Chip* **12**, 1026-1039,(2012).
[223] Saffman, P. G. On motion of small spheroidal particles in viscous liquid. *Journal of Fluid Mechanics* **1**, 540-553,(1956).
[224] Bretherton, F. P. Slow viscous motion round cylinder in simple shear. *Journal of Fluid Mechanics* **12**, 591-613,(1962).
[225] Saffman, P. G. Lift on a Small Sphere in a Slow Shear Flow. *Journal of Fluid Mechanics* **22**, 385-&,(1965).
[226] Feng, J., Hu, H. H. & Joseph, D. D. Direct Simulation of Initial-Value Problems for the Motion of Solid Bodies in a Newtonian Fluid .2. Couette and Poiseuille Flows. *Journal of Fluid Mechanics* **277**, 271-301,(1994).
[227] Choi, Y. S., Seo, K. W. & Lee, S. J. Lateral and cross-lateral focusing of spherical particles in a square microchannel. *Lab Chip* **11**, 460-465,(2011).
[228] Chun, B. & Ladd, A. J. C. Inertial migration of neutrally buoyant particles in a square duct: An investigation of multiple equilibrium positions. *Physics of Fluids* **18**, 031704,(2006).

[229] Lim, E. J., Ober, T. J., Edd, J. F., McKinley, G. H. & Toner, M. Visualization of microscale particle focusing in diluted and whole blood using particle trajectory analysis. *Lab Chip* **12**, 2199-2210,(2012).
[230] Bhagat, A. A. S., Kuntaegowdanahalli, S. S. & Papautsky, I. Enhanced particle filtration in straight microchannels using shear-modulated inertial migration. *Physics of Fluids* **20**, 101702,(2008).
[231] Zhou, J., Giridhar, P. V., Kasper, S. & Papautsky, I. Modulation of aspect ratio for complete separation in an inertial microfluidic channel. *Lab Chip* **13**, 1919-1929,(2013).
[232] Zhou, J. & Papautsky, I. Fundamentals of inertial focusing in microchannels. *Lab Chip* **13**, 1121-1132,(2013).
[233] Inamuro, T., Maeba, K. & Ogino, F. Flow between parallel walls containing the lines of neutrally buoyant circular cylinders. *International Journal of Multiphase Flow* **26**, 1981-2004,(2000).
[234] Matas, J.-P., Glezer, V., Guazzelli, E. l. & Morris, J. F. Trains of particles in finite-Reynolds-number pipe flow. *Physics of Fluids* **16**, 4192,(2004).
[235] Kemna, E. W. *et al*. High-yield cell ordering and deterministic cell-in-droplet encapsulation using Dean flow in a curved microchannel. *Lab Chip* **12**, 2881-2887,(2012).
[236] Agresti, J. J. *et al*. Ultrahigh-throughput screening in drop-based microfluidics for directed evolution. *Proceedings of the National Academy of Sciences of the United States of America* **107**, 4004-4009,(2010).
[237] Lagus, T. P. & Edd, J. F. High Throughput Single-cell and Multiple-cell Micro-encapsulation. *Journal of visualized experiments : JoVE* **64**, 4096,(2012).
[238] Lagus, T. P. & Edd, J. F. High-throughput co-encapsulation of self-ordered cell trains: cell pair interactions in microdroplets. *RSC Advances* **3**, 20512,(2013).
[239] Hur, S. C., Tse, H. T. & Di Carlo, D. Sheathless inertial cell ordering for extreme throughput flow cytometry. *Lab Chip* **10**, 274-280,(2010).
[240] Rubinow, S. I. & Keller, J. B. Transverse force on spinning sphere moving in viscous fluid. *Journal of Fluid Mechanics* **11**, 447-459,(1961).
[241] Cox, R. G. & Brenner, H. The lateral migration of solid particles in Poiseuille flow — I theory. *Chemical Engineering Science* **23**, 147-173,(1968).
[242] Ho, B. P. & Leal, L. G. Inertial migration of rigid spheres in two-dimensional unidirectional flows. *Journal of Fluid Mechanics* **65**, 365-400,(1974).
[243] Kaneda, Y. & Ishii, K. The hydrodynamic interaction of two spheres moving in an unbounded fluid at small but finite reynolds-number. *Journal of Fluid Mechanics* **124**, 209-217,(1982).
[244] Cherukat, P. & McLaughlin, J. B. Wall-induced lift on a sphere. *International Journal of Multiphase Flow* **16**, 899-907,(1990).
[245] Cherukat, P. & Mclaughlin, J. B. The inertial lift on a rigid sphere in a linear shear-flow field near a flat wall. *Journal of Fluid Mechanics* **263**, 1-18,(1994).
[246] Schonberg, J. A. & Hinch, E. J. Inertial migration of a sphere in poiseuille flow. *Journal of Fluid Mechanics* **203**, 517-524,(1989).
[247] Asmolov, E. S. The inertial lift on a spherical particle in a plane Poiseuille flow at large channel Reynolds number. *Journal of Fluid Mechanics* **381**, 63-87,(1999).
[248] Matas, J.-P., Morris, J. F. & Guazzelli, É. Inertial migration of rigid spherical particles in Poiseuille flow. *Journal of Fluid Mechanics* **515**, 171-195,(2004).

[249] Kobel, S. & Lutolf, M. P. Biomaterials meet microfluidics: building the next generation of artificial niches. *Current opinion in biotechnology* **22**, 690-697,(2011).
[250] Chabert, M. & Viovy, J. L. Microfluidic high-throughput encapsulation and hydrodynamic self-sorting of single cells. *Proceedings of the National Academy of Sciences of the United States of America* **105**, 3191-3196,(2008).
[251] Abate, A. R., Chen, C. H., Agresti, J. J. & Weitz, D. A. Beating Poisson encapsulation statistics using close-packed ordering. *Lab Chip* **9**, 2628-2631,(2009).
[252] Humphry, K. J., Kulkarni, P. M., Weitz, D. A., Morris, J. F. & Stone, H. A. Axial and lateral particle ordering in finite Reynolds number channel flows. *Physics of Fluids* **22**, 081703,(2010).
[253] Lee, W., Amini, H., Stone, H. A. & Di Carlo, D. Dynamic self-assembly and control of microfluidic particle crystals. *Proceedings of the National Academy of Sciences of the United States of America* **107**, 22413-22418,(2010).
[254] Haubert, K., Drier, T. & Beebe, D. PDMS bonding by means of a portable, low-cost corona system. *Lab Chip* **6**, 1548-1549,(2006).
[255] Garstecki, P., Stone, H. & Whitesides, G. Mechanism for Flow-Rate Controlled Breakup in Confined Geometries: A Route to Monodisperse Emulsions. *Physical Review Letters* **94**,(2005).
[256] Nie, Z. *et al*. Emulsification in a microfluidic flow-focusing device: effect of the viscosities of the liquids. *Microfluidics and Nanofluidics*,(2008).
[257] Pan, J. *et al*. Quantitative tracking of the growth of individual algal cells in microdroplet compartments. *Integrative biology : quantitative biosciences from nano to macro* **3**, 1043-1051,(2011).
[258] Dewan, A., Kim, J., McLean, R. H., Vanapalli, S. A. & Karim, M. N. Growth kinetics of microalgae in microfluidic static droplet arrays. *Biotechnology and bioengineering* **109**, 2987-2996,(2012).
[259] Lagus, T. P. & Edd, J. F. A review of the theory, methods and recent applications of high-throughput single-cell droplet microfluidics. *Journal of Physics D: Applied Physics* **46**, 114005,(2013).
[260] Gao, Y. *et al*. A versatile valve-enabled microfluidic cell co-culture platform and demonstration of its applications to neurobiology and cancer biology. *Biomedical microdevices* **13**, 539-548,(2011).
[261] Businaro, L. *et al*. Cross talk between cancer and immune cells: exploring complex dynamics in a microfluidic environment. *Lab Chip* **13**, 229-239,(2013).
[262] Tumarkin, E. *et al*. High-throughput combinatorial cell co-culture using microfluidics. *Integrative biology : quantitative biosciences from nano to macro* **3**, 653-662,(2011).
[263] Srigunapalan, S., Eydelnant, I. A., Simmons, C. A. & Wheeler, A. R. A digital microfluidic platform for primary cell culture and analysis. *Lab Chip* **12**, 369-375,(2012).
[264] Fidalgo, L. M., Abell, C. & Huck, W. T. Surface-induced droplet fusion in microfluidic devices. *Lab Chip* **7**, 984-986,(2007).
[265] Harris, E. H. *The Chlamydomonas sourcebook : introduction to chlamydomonas and its laboratory use*. 2nd edn, 241-302 (Academic Press, 2009).
[266] Rosales-Mendoza, S., Paz-Maldonado, L. M. & Soria-Guerra, R. E. Chlamydomonas reinhardtii as a viable platform for the production of recombinant proteins: current status and perspectives. *Plant cell reports* **31**, 479-494,(2012).

[267] Harun, R., Danquah, M. K. & Forde, G. M. Microalgal biomass as a fermentation feedstock for bioethanol production. *Journal of Chemical Technology & Biotechnology* **85**, 199-203,(2010).
[268] Burgess, S. J., Tamburic, B., Zemichael, F., Hellgardt, K. & Nixon, P. J. Solar-driven hydrogen production in green algae. *Advances in applied microbiology* **75**, 71-110,(2011).
[269] Merchant, S. S., Kropat, J., Liu, B., Shaw, J. & Warakanont, J. TAG, you're it! Chlamydomonas as a reference organism for understanding algal triacylglycerol accumulation. *Current opinion in biotechnology* **23**, 352-363,(2012).
[270] Jones, C. S. & Mayfield, S. P. Algae biofuels: versatility for the future of bioenergy. *Current opinion in biotechnology* **23**, 346-351,(2012).
[271] Natarajan, N. M. & Lakshmanan. Laminar flow in rectangular ducts: Prediction of velocity profiles and friction factor. *Indian Journal of Technology* **10**, 435-438,(1972).
[272] Sueoka, N. Mitotic replication of deoxyribonucleic acid in chlamydomonas reinhardi. *Proceedings of the National Academy of Sciences* **46**, 83-91,(1960).
[273] Sager, R. & Granick, S. Nutritional control of sexuality in chlamydomonas reinhardi. *The Journal of General Physiology* **37**, 729-742,(1954).
[274] Yoshimura, K., Matsuo, Y. & Kamiya, R. Gravitaxis in Chlamydomonas reinhardtii studied with novel mutants. *Plant Cell Physiol* **44**, 1112-1118,(2003).
[275] Solter, K. M. & Gibor, A. Evidence for role of flagella as sensory transducers in mating of chlamydomonas-reinhardi. *Nature* **265**, 444-445,(1977).
[276] Ai, X. *et al*. Controlling gas/liquid exchange using microfluidics for real-time monitoring of flagellar length in living Chlamydomonas at the single-cell level. *Lab Chip* **12**, 4516-4522,(2012).
[277] Lewin, R. A., Lee, T. H. & Fang, L. S. Effects of Various Agents on Flagellar Activity, Flagellar Autotomy and Cell Viability in 4 Species of Chlamydomonas (Chlorophyta, Volvocales). *Sym Soc Exp Biol*, 421-437,(1982).
[278] Jiang, X. & Stern, D. Mating and Tetrad Separation of Chlamydomonas reinhardtii for Genetic Analysis. *Journal of visualized experiments : JoVE*, e1274,(2009).
[279] Crocker, J. C. track.pro (MATLAB Version). http://physics.georgetown.edu/matlab/ (1999).
[280] Hur, S. C., Choi, S.-E., Kwon, S. & Carlo, D. D. Inertial focusing of non-spherical microparticles. *Applied Physics Letters* **99**, 044101,(2011).
[281] Masaeli, M. *et al*. Continuous inertial focusing and separation of particles by shape. *Physical Review X* **2**, 031017,(2012).
[282] Cooper, M. S., Hardin, W. R., Petersen, T. W. & Cattolico, R. A. Visualizing "green oil" in live algal cells. *Journal of bioscience and bioengineering* **109**, 198-201,(2010).
[283] Hardy, J. T. & Curl, H. Candy-colored, snow-flaked Alpine biome. *Natural History* **81**, 74-78,(1972).
[284] Clausell-Tormos, J. *et al*. Droplet-based microfluidic platforms for the encapsulation and screening of Mammalian cells and multicellular organisms. *Chemistry & biology* **15**, 427-437,(2008).
[285] Matas, J.-P., Morris, J. F. & Guazzelli, É. Lateral force on a rigid sphere in large-inertia laminar pipe flow. *Journal of Fluid Mechanics* **621**, 59,(2009).
[286] Steinke, M. & Kandlikar, S. Single-phase liquid friction factors in microchannels. *International Journal of Thermal Sciences* **45**, 1073-1083,(2006).

[287] Guizar-Sicairos, M., Thurman, S. T. & Fienup, J. R. Efficient subpixel image registration algorithms. *Optics Letters* **33**, 156,(2008).
[288] Paul, R. *et al*. Shear stress related blood damage in laminar Couette flow. *Artificial Organs* **27**, 517-529,(2003).
[289] Loth, E. & Dorgan, A. J. An equation of motion for particles of finite Reynolds number and size. *Environmental Fluid Mechanics* **9**, 187-206,(2009).
[290] Rasband, W. S. ImageJ 1.46r. http://imagej.nih.gov/ij/ (U.S. National Institutes of Health, Bethesda, MD, 1997-2012).
[291] Studer, V. *et al*. Scaling properties of a low-actuation pressure microfluidic valve. *J. Appl. Phys*. **95**, 393-398,(2004).